A B S T R A C T

THE SMW TRIO AND THE MEASUREMENT OF PROTON-IRON INELASTIC CROSS SECTION ABOVE 70 GeV

by

Billy Wei-yu Loo

Co-chairmen: Lawrence W. Jones, David R. Bach

The Streamer chamber, Marx generator, amd Wide-gap spark chamber form an intimate trio that support and complement each other as detectors for ultra-high energy charged particles.

A research program covering the feasibility study and actual incorporation of such devices in a high altitude cosmic ray experiment is reported. Design philosophies and optimization procedures are also presented. The program resulted in the successful development of (1) the first streamer chamber in the U.S. and demonstrated the practicality of recording streamers of arbitrary length along the electric field when coupled to an image intensifier system, and (2) a compact 10-stage Marx generator with a total capacitance of 0.08 μf and a capability of delivering a

voltage pulse of 50-300 kV amplitude with both the rise-time and delay-time to be in the neighborhood of two nano-seconds, and (3) a high precision multi-wide-gap spark chamber with an intrinsic angular resolution of 0.1 mr per gap; and two such chambers are employed in conjunction with a superconducting magnet of 13 kilogauss-meters to form a spectrometer which has a maximum detectable momentum of about 5 TeV/c.

Concurrent with the magnetic spectrometer development, the energy dependence of proton-iron inelastic cross section was studied with a total absorption ionization calorimeter of 1200 gm/cm^2 of iron interleaved with 10 plastic scintillation layers. Systematic effects were thoroughly investigated. It was found that between 20 and 1500 GeV the cross section was best represented by a flat 710 mb with a slope uncertainty of 3.5% per decade change in energy.

UM HE 72-12

THE SMW TRIO AND THE MEASUREMENT OF PROTON-IRON INELASTIC CROSS SECTION ABOVE 70 GeV

by

Billy Wei-yu Loo

A dissertation submitted in partial fulfillment
of the requirements for the degree of
Doctor of Philosophy
(Physics and Nuclear Engineering)
in The University of Michigan
1972

Doctoral Committee:

Professor Lawrence W. Jones, Co-chairman
Professor David R. Bach, Co-chairman
Professor Wayne E. Hazen
Professor John S. King
Associate Professor Glenn F. Knoll

ACKNOWLEDGEMENT

I must first of all thank my parents whose sacrificial love and earnest quest for reality and wisdom have always been a sustaining and motivating force for me.

I would like to express my respect and gratitude to Prof. Lawrence Jones, true gentleman and scholar, for his most intellegent and considerate guidance throughout my graduate career.

I would like to thank Prof. David Bach for his counselling and coordinational effort which made the joint degree in physics and nuclear engineering possible.

I am indebted to Orman Haas for his kind and ingenious mechanical assistance in all phases of the work; to Fritz Bausch for his expert help on wide-gap spark chambers and surveying instruments; to Paul Holloway and the entire staff of the physics instrument shop, Glenn Edict and Jim Pluta of the electronics shop for many years of uncommon cooperation; to Dick Worland and his surveying staff at the Argonne National Laboratory for their excellent fiducial measurements; to Tom McCorreston for helpful theoretical discussions; to the University of Denver for the hospitality at its High Altitude Lab; to the Lawrence Berkeley Lab for the use of film measuring facilities in the early phase of the experiment; to the Argonne National Lab for the film

processing and computing facilities; and to all who have participated in the construction, execution, film measurement, and data reduction of the Echo Lake experiment; their pleasant coorporation is collectively but gratefully acknowledged.

TABLE OF CONTENTS

LIST OF TABLES

LIST OF FIGURES

CHAPTER I

BACKGROUND

A. INTRODUCTION

In the course of a few decades, man has witnessed the phenomenal growth of particle accelerator technology and the resulting population explosion of elementary or subnuclear particles. At the same time he could no longer comfortably account for the physical universe in terms of gravitational and electromagnetic interactions. Yet in spite of vast volumes of experimental data accumulated and efforts of thorough theoretical scrutiny, the true nature of strong and weak interactions remains a mystery. From the few pieces of the puzzle assembled so far, physicists are convinced that there will not be enough clues available from the data of present day accelerator energy of 70 GeV. (1) It is further believed that due to the wave nature of matter, large momentum and energy transfer is only possible in small regions of space and time, and the short deBroglie wave lengths of particles of hundreds or thousands of GeV will be necessary to probe spacial structures below 10^{-15} cm and time intervals under 10^{-25} sec. It is hoped that life will be simpler in the smaller world.

Just as larger accelerators are essential to the production of high energy particles, more sophisticated instruments are needed to detect or analyze them. Only

through advanced and precision instruments can man extend his realm of physical observations. The 200 GeV accelerator will soon be operational and other accelerators of up to 5000 GeV are under consideration.[2] Superconducting or even cold aluminum magnets will undoubtedly make them economically feasible someday and new detectors will be sought to meet those demands.

B. HIGH ENERGY PARTICLE DETECTOR RESEARCH

We shall consider here only charged particle detectors although neutral particles and energetic photons are always detected through the production of charged particles. Thus all particles, whether they are strong or weak interacting, are eventually detected via electromagnetic interactions in the detection medium. Gravitons and neutrinos are of course exceptions.

There is a whole army of particle detectors ranging from the old Geiger Müller counter to solid state detectors; but we shall only consider those which would yield momentum or energy information in the ultra-relativistic range. That is, when the energy of a particle is much larger than its rest mass or $\gamma \gg 1$ where

$$\gamma = \frac{1}{\sqrt{1-\beta^2}} \quad ,$$

and

$$E = \gamma m_o c^2 \approx pc \quad .$$

Energy measurements may generally be carried out under the following five categories:

(1) Velocity Selection

(a) Time of flight measurement: This is the simplest and most direct measurement but its effectiveness is rather limited at high energies. For instance, the best time resolution of counters is about 10^{-10} sec. For a flight path of say 10 m, the velocity resolution $d\beta \approx c \frac{dt}{x} = 3 \times 10^{-3}$. Since

$$\frac{dp}{p} \approx \frac{dE}{E} = \beta\gamma^2 d\beta \approx \gamma^2 d\beta \quad ,$$

the maximum detectable γ is 18.3 or the maximum detectable momentum is under 20 GeV/c for protons.

(b) Cerenkov detectors: When the velocity of a charged particle exceeds the velocity of light in the medium with index of refraction n, continuous spectrum of Cerenkov radiation will be emitted at an angle θ with respect to the particle trajectory according to $\cos\theta = \frac{1}{\beta n}$ and the number of photons N produced by a particle of charge Ze along the track length x in the wave length region of λ_1 to λ_2 is

$$N = 2\pi \frac{e^2}{\hbar c} Z^2 \times \int_{\lambda_1}^{\lambda_2} \left(1 - \frac{1}{\beta^2 n^2}\right) \frac{d\lambda}{\lambda^2} \quad .$$

It is thus possible to operate a Cerenkov detec-

tor as a threshold counter or a differential counter for $\beta n > 1$ and $\Delta\beta$, corresponding to the range of $\Delta\theta$ accepted in the detector, respectively. Making use of the previous equation, it is also possible to operate a multichannel Cerenkov counter in which the detected light intensity is related to the momentum of the particle. Recent development has pushed the resolution to $\Delta\beta = 6 \times 10^{-7}$ (3) or a maximum detectable γ of 1290.

(2) Magnetic Bending

Unlike in an electric field, a charged particle experiences no energy change while traversing a constant magnetic field. But more relavent is the fact that the largest practically attainable magnetic force is some hundred times higher than the electric force. In the case of magnetic bending, the particles energy for unit charge in GeV is equal to the magnetic rigidity

$$E = 30\ BR \quad ,$$

where B is the magnetic field in kilogauss and

R is the radius of curvature in kilometers

and $$R \approx \frac{1}{8} \frac{L^2}{S} \quad ,$$

where L is the path length in the magnetic field and

S is the sagitta .

It is seen that $\frac{dE}{E} = \frac{dS}{S}$ and the spacial resolution of the detector in the magnetic field will be of

prime importance. Bubble chambers and wide-gap spark chambers have spacial resolution of about 0.1 mm, while that of cloud chambers and streamer chambers is about 0.2 mm.

On the other hand, if detectors are placed outside of the magnetic field and the deflection angle θ is measured,

$$E = \frac{30}{\theta} \int B_{\perp} dL \quad .$$

Given the same magnetic field strength and region and given the same spacial resolution of the detectors, it is seen from simple geometrical consideration that one can achieve an energy resolution of a factor of four better with the detectors outside of the magnetic field region. Spacial resolution of 2 μm can be achieved with emulsions[4] while those of wire spark chambers and counter hodoscope are about 0.3 mm and a few mm respectively.

(3) Relativistic Rise in Energy Loss

The rate of energy loss of a particle of charge ze in a medium of atomic number Z by excitation and ionization along its trajectory is given by

$$-\frac{dE}{dx} = \frac{4\pi e^4 z^2 N}{mv^2} Z \left[\ln \frac{2mv^2}{I} - \ln(1-\beta^2) - \beta^2 \right]$$

where N is the number of absorber atoms per cm^3 and

I is the mean excitation and ionization potential of the absorbing atoms.

In general, $\frac{dE}{dx}$ decreases rapidly as E is increased and a characteristic minimum is reached at about twice the rest mass energy of the particle. It then increases logarithmicly with E. Such a rise is reduced in denser materials or at ultra-relativistic energies due to the screening of the Coulomb field by the close packing of the atoms. But such density effect is found to be absent in the case of thin ($\sim 10^{-5}$cm) films. Thus a measure of $\frac{dE}{dx}$ is a measure of log γ. Streamer chambers,[5] proportional counter arrays[6] are suitable for this type of measurements. Collecting secondary electrons from thin film solid state detector slabs is also a promissing approach.[7]

Transition Radiation

When a charged particle traverses a boundary of two media of different dielectric constants, a continuous spectrum of transition radiation in the optical region is proportional to log γ while in the x-ray region it is linearly proportional to γ. When foils of thickness just thicker than the formation zone (<20 μm) of such radiation are stacked with appropriate spacing (<1 mm), sufficient x-ray photons will be generated and can be detected by proportional counters or solid

state detector arrays. The total length of the detector needed is much less than that of a corresponding threshold Cerenkov counter whose length increases proportionally to γ^2. (9)

(5) Total Absorption Spectrometers

(a) Calorimeters: Usually the particle and its reaction products, excepting muons and neutrinos, are completely contained within the bulk of a stack of iron. Its energy is proportional to the total ionization that is sampled by layers of plastic or liquid scintillation counters. Corrections must be made for undetected energy of nuclear disintegration and the estimation of energy loss in iron by the measurement of ionization in the scintillators. The best energy resolution is about 10-20%, depending on design parameters.

(b) Total absorption nuclear cascade counters: In contrast to the sampling nature of the calorimeter, all of the particle energy which finally appears in the form of collision loss to the atomic electrons in large slabs of scintillation crystals is detected. Since the absorption mean free path is at most slowly varying at extremely high energies, there is virtually no limit to the highest energy detectable. Besides, energy resolution of close to 1% can be achieved.(10)

C. RELATIVE MERIT

There are at least a dozen properties that an ideal detector should have. The most crucial ones are of course high detection efficiency, high energy resolution and possible particle identification. It would also be extremely helpful to have high multiparticle efficiency and a large dynamic range of energy measurement. Furthermore, it would be nice if the particle will survive the measurement. When events are very frequent, one would like it to have good time resolution and repetition rate. And when events are very infrequent or when background rate is high, one would like it to have large acceptance and capability for external triggering. Other important features concern the speed of data reduction and possible on-line operation or decision making. Finally there is the inescapable question of cost.

The ideal tool does not exist. In order to choose the proper weapon for a specific situation, it may be helpful to list some of the long and short ends of the alternatives:

Table 1

Some Detector Properties

DETECTOR	ADVANTAGE	DISADVANTAGE
Time of Flight	Fast and simple.	Low maximum detectable momentum.
Cerenkov Counter	Good velocity selector and particle identifier at moderate energies.	Can be excessively long. Low admittance.
Bubble Chamber	Excellent spacial resolution. Ionization information. Detection medium can also serve as target. Excellent vertex detections. Isotropic.	Non-triggerable. Expensive. Long dead time (~1 sec)
Wide-gap Spark Chamber	Excellent angular resolution. Easy to build very large and simple systems. High multiple track efficiency.	Non-isotropic. No ionization information. Moderate time resolution (~1 μsec) and dead time (~0.1 sec)
Cloud Chamber	Ionization information.	Very long dead time (~10 sec)

Table 1 (continued)

DETECTOR	ADVANTAGE	DISADVANTAGE
Streamer Chamber	Ionization information. Isotropic. High multiple track efficiency.	Low light output. Moderate time resolution and dead time.
Emulsion	Unsurpassed spacial resolution.	Serious background loading problem. Awkward to use.
Wire Spark Chambers	On line analysis. High repetition rate. Large system possible.	No ionization information. Low multiple track efficiency. Moderate spacial resolution.
Counter Hodoscope	On line analysis. Very high repetition rate.	Poor spacial resolution.
Proportional Counter	Particle identification	Limited by density effect and ionization fluctuations.

Table 1 (continued)

DETECTOR	ADVANTAGE	DISADVANTAGE
Thin Film Secondary Electron Detector	True log γ measurement.	Limited size, thus admittance and efficiency.
Transition Radiation Detector	Linearly Proportional to γ. Large dynamic range.	Limited size. Non-isotropic.
Calori-meter	Good energy threshold triggering device.	Destructive measure-ment. Non-isotropic. Moderate energy re-solution. Bulky, thus limited admittance to diverging particles.
Total Absorption Nuclear Cascade Detector	Excellent energy reso-lution. Homogeneous. Particle identification. Unsurpassed dynamic range.	Destructive measure-ment. Limited admit-tance. Expensive.

D. THE EMERGENCE OF THE SMW TRIO

Since all radiations eventually lose a significant fraction of their energies through ionization of the medium, gas filled detectors form the oldest and most reliable family of nuclear workhorses. The ionization chamber, proportional counter and Geiger-Müller counter differ little more than different voltage regions of operation. They indeed formed the first trio of nuclear detectors.

The early spark chamber was actually a transformation of the G-M tube with plane electrodes. But when its reliability was improved by voltage pulsing and noble gas filling, it had possessed the outstanding capability of displaying spacial information. This fact, together with its good time resolution and intrinsic simplicity, had enabled it to blossom into a field of its own. The depth and diversity of its development was phenomenal. One measure of its growth is the number of pages per review article that was devoted to it in the decade of the Sixties as shown in Figure 1.

It is not necessary to mention here the various possibilities and modes of operation of spark chambers. They can be found in the review articles (11-16). Charpak also has a good summary of spark chambers with automatic filmless readout or data recordings in ref.(17). But even with such a large spectrum of spark chamber types they

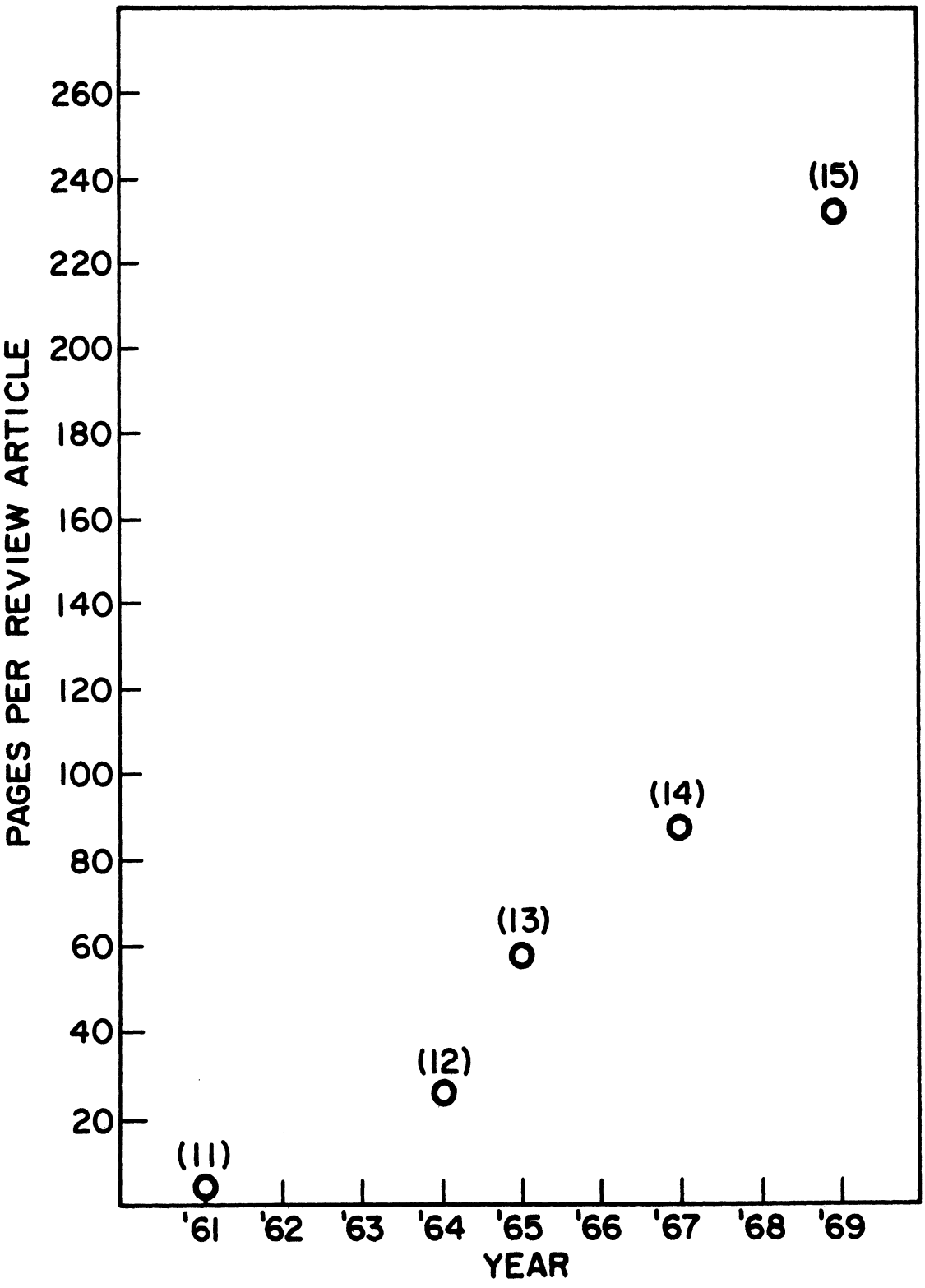

Fig.1 Growth of Spark Chamber Research

generally fall under two catagories, i.e. wide-gap and narrow-gap chambers.

The electrode spacings of narrow-gap chambers are typically under 1 cm and the voltage pulse required is usually under 15 kV, which can be easily provided by the switching of a thyratron or a single spark-gap. With the application of clearing field or quench gas, the time resolution can be made very short, and together with digitized readout they are particularly suited for rapid on-line analysis in intense particle beams.

However, the spark in a narrow-gap chamber generally follows the electric field line rather than the actual trajectory of the particle. Therefore one can get only one set of 2-dimensional spacial information, which is accurate to about 0.2 mm, from each gap. In other words, the information density is not high for narrow-gap chambers. and unless one is at liberty to place chambers arbitrarily far apart, with the correspondingly low detection solid angle, narrow-gap chambers are not the best choice as far as the question of maximum detectable momentum is concerned. Furthermore, multiple-particle and large-angle (with respect to electric field) detection efficiencies are moderate. Ionization information is not available either.

On the other hand, the electrode spacings of wide-gap spark chambers are usually tens of centimeters and voltage pulses of hundreds of kilovolts are required. If

the high voltage pulse width is sufficiently large to allow the development of a full spark channel, the spark will follow the trajectory of the particle (except at regions of within 1 cm from the electrodes) up to about 40°. Beyond that point, tracks are more diffused and finally disappear at about 60° with respect to the electric field. But if the pulse width is shortened to under about tens of nanoseconds, the development of each ion pair will be limited and generally prevented from coalescing with their neighbors. The resulting track of truncated streamers not only registers almost isotropic 3-dimensional spacial information about the particle trajectory, it may also provide ionization information for relativistic rise measurements.

Whether it is operated in streamer mode or in spark mode, multiple track efficiencies are extremely high. It is the combination of high information density (up to the reciprocal of ion density along the track), high efficiency, intrinsic simplicity (hence practicality for large and precise systems) and the capability for post event triggering that makes them most attractive for ultra-high energy applications.

As we have seen that wide-gap chambers while enjoying certain advantages as a class by themselves also bear more stringent requirements. In order to achieve optimum operations, they need high voltage pulses of hundreds of kilovolts with fast rise-times and minimum delays. But

as far as voltage availability is concerned, there seems to be a natural barrier at about 30-50 kV, beyond which general insulating problems become rapidly more difficult. Common electronic components and switching by thyratrons or single spark-gaps have reached their practical limits. Here is where the Marx generator comes to the rescue.

Marx generators work on the simple principle of charge conservation. If n capacitors charged in parallel to a d.c. supply voltage of V_o are rapidly switched by spark gaps to series connections, and if all capacitors are isolated from each other by large enough resistors such that the RC time constant of any part of the circuit is much larger than the switching time, a voltage of nV_o will be developed across the series. The optimization procedures to meet the demands of wide-gap chambers will be the subject of chapter III. It is thus clear that Streamer chambers, Marx generators and Wide-gap spark chambers intimately support and complement each other to form a unique family of detectors for ultra-high energy physics. Indeed, they are the SMW trio.

E. THEORY OF GAS DISCHARGE

Gas discharge is the basic mechanism that is common to all members of the SMW trio. The beauty of the SMW Trio is their intrinsic simplicity; and they can be made operational without a detailed knowledge of the gas dis-

charge mechanism. However a brief description of several pertinent aspects may clarify some of the optimization procedures involved.

Table 2 lists some of the commonly used chamber gas properties under typical operational condition of electric field E=10 kV/cm and at one atmosphere. More complete data on the variation of these properties with various parameters are available; but these may serve as guide lines.

When a charged particle passes through the chamber fill gas, a trail of ions will be left along its trajectory (Fig.2A). The diffusion constants of positive ions are a few orders of magnitude smaller than those of electrons, so one only needs to be concerned with electron motions. Upon the arrival of the uniform high voltage gradient E, each electron will initiate a cascade of ionizations, called an avalanche, towards the anode as illustrated in Fig.2B. The multiplication factor is described by $e^{\alpha x}$ where α is known as the first Townsend coefficient of ionization, and x is the distance from the original ion. The drift velocity v for $\frac{E}{P} > 10$ is [22]

$$v = 2.6 \times 10^6 \sqrt{\frac{E}{P} - 1.5} \text{ cm/sec}$$

where E is in V/cm and

P is in torr

Ordinarily the avalanche will propagate with a velocity of 10^7 cm/sec until the external electric field is

TABLE 2

Some Noble Gas Properties at E=10 kV/cm and P=760 torr

	Helium	Neon	Argon	REF.
First Townsend Ionization Coefficient α (cm^{-1})	60	70	10	(19)
Electron Diffusion Coefficient D (cm^2/sec)	4400 310*	8100 2000*	1100 370*	(20)
Electron Mean Free Path λ (μm)	2.7	1.8	1.2	(15)
Ionization Potential (eV)	24.5	21.5	15.7	(19)
Metastable States (eV)	20.7 19.8	16.7 16.6	11.7 11.5	(19)
Primary Specific Ionization (ion pairs per cm)	6.6	15	30	(21)

* Diffusion coefficient with E = 0

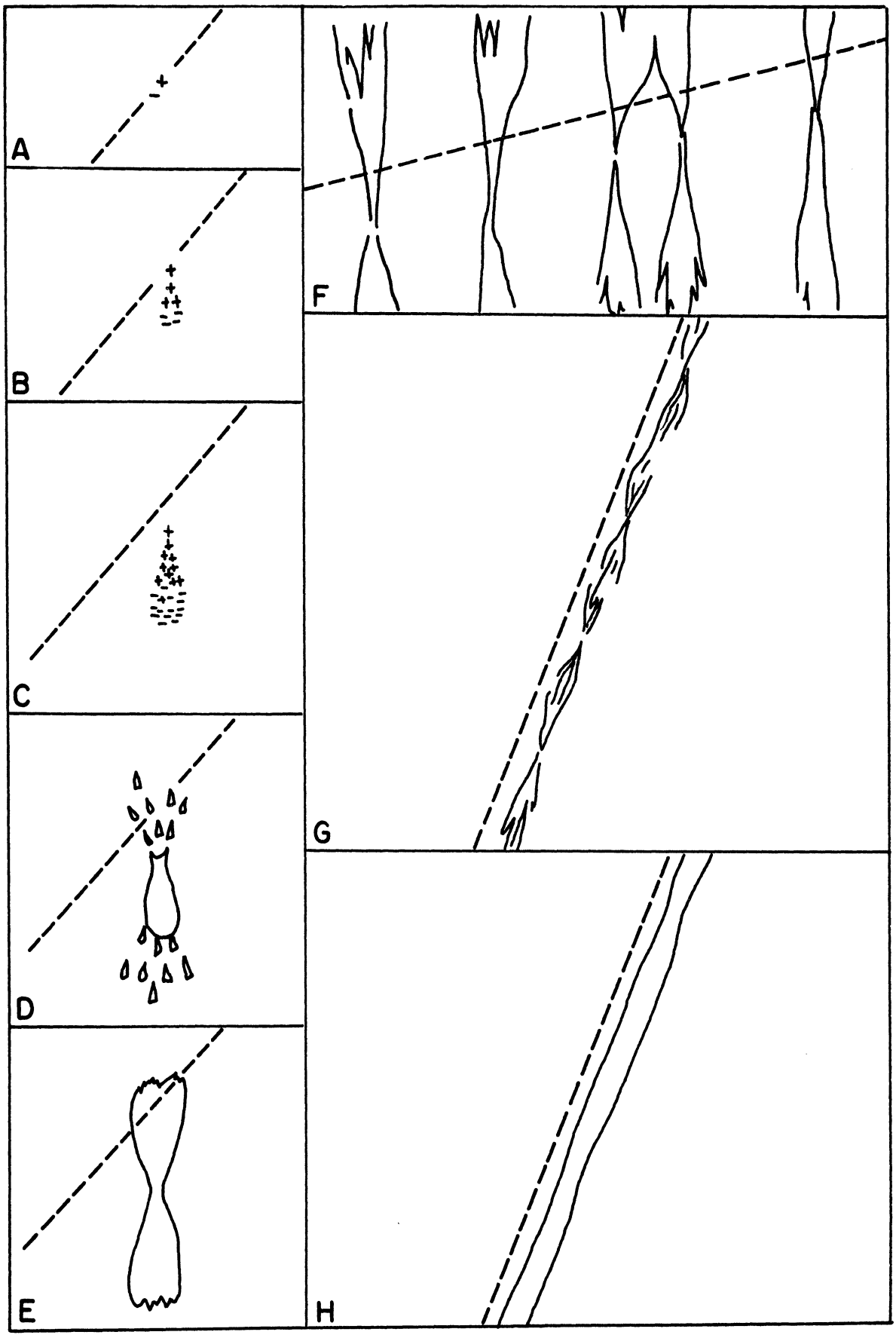

Fig.2 The Evolution of a Spark Channel

locally cancelled by the roughly dipole field of the space charges; this is known as the Meek condition (Fig.2C). At this point multiplication by collision will cease. But if it has reached such a magnitude that $\alpha x = 20$ (or an ion density of about 7×10^{11} cm^{-3}) sufficient energetic photons will have been produced to induce photoionization.[23] Photoionizations cause secondary avalanches to form near the head and the tail of the avalanche, where the electric field is most intense (Fig.2D). Electrons are expelled away from the negative head of the original avalanche and are drawn into the positive tail. These secondary streamers coalesce and transform into positive and negative streamers (Fig.2E). They grow in opposite directions along the electric field lines at about 10^8 cm/sec. If the voltage is sharply switched off at this stage, as in the case of streamer chamber operation, the streamers will be "frozen" in space to yield spacial information about the particle. The avalanches are not visible and the empirical relation for the young streamers to become sufficiently bright for photographic recording is (for neon) [24]

$$\frac{E^2 \tau}{P} = 9.1 \pm 1.5$$

where E is in kV/cm

τ is the pulse width in nanoseconds, and

P is in torr.

If the pulse width is made longer, streamers will continue to grow, and branching may take place along adjacent field

lines.

The coalescence of secondary streamers will result in a highly conductive channel of plasma. The chamber will be called a projection chamber or a wide-gap spark chamber, depending whether the conducting columns are formed out of independent primary ion pairs (Fig.2F), or out of the linkage of neighboring streamers (Fig.2G) along the trajectory of the particle to form a rather uniform spark (Fig.2H). In either case, voltage is terminated by the spark channels themselves. Such a spark formation time τ_F is shown to be primarily depending on the Townsend coefficient α and electron drift velocity v, and only mildly varying with chamber size and circuit parameters:

$$\tau \approx \frac{29.5 \pm 0.5}{\alpha v} \ (\mu \text{ sec }) \ .$$

Measurements by Fisher and Zorn are shown in Fig.3. [25]

The performance of the wide-gap chambers are heavily dependent on the nature of the working gas. The questions of proper choice, the control of impurities and, in particular, the effects on space and time resolutions will be explored further in Chapter IV.

F. COSMIC RAY EXPERIMENT

Particle accelerators in nature existed long before artificial ones. Cosmic rays, which are mainly protons with a decreasingly small percentage of heavier nuclei, rain on the earth from all directions. Some are prevented

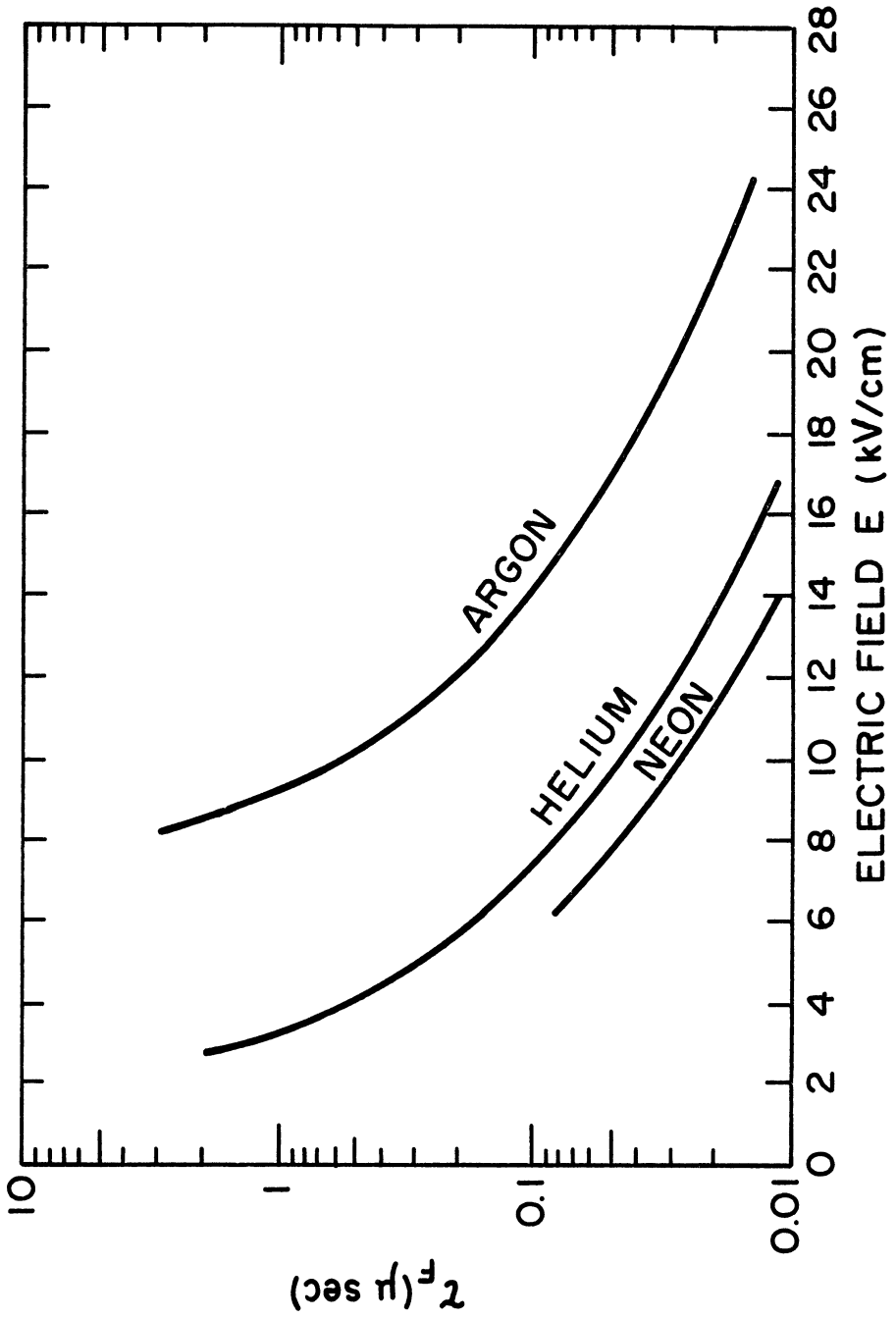

Fig.3 Spark Formation Time

from reaching the surface due to the deflection in the earth's magnetic field and by the attenuation of the atmosphere. Taking 0.31 gauss as the equatorial magnetic field and 6.38×10^8 cm as the earth's radius, any particle with a magnetic rigidity of greater than 59.3 GeV can always reach the earth. The atmosphere being 1030 gm/cm^2 thick provides about eight absorption mean free paths of shielding against energetic protons. The integral spectrum of primary cosmic rays above 1GeV is roughly 0.3 cm^{-2} sec^{-1} sterad^{-1} while the flux above energy E is proportional to $E^{-1.7}$. Some particles had been recorded with energy exceeding 10^{20} ev.

Thus by setting up an experiment as high above the atmosphere and with as large a detector as is practical, one could get a preview of ultra-high energy interactions before the arrival of super accelerators in the hundreds or even thousands of GeV range.

This is what we have done at Echo Lake, Colorado which is at an altitude of 3230 m or above one third of the atmosphere. Fig.4 shows Sigma Hall, the building which houses the main apparatus and the fast logics. The adjacent 40 foot trailer houses other electronic control and recording systems.

Fig.5 is a schematic of the experimental set up. A coincidence of pulses from the top counter, the second layer of the calorimeter, the sum pulse of the entire calorimeter exceeding a preset threshold of 36 or 90 GeV, and

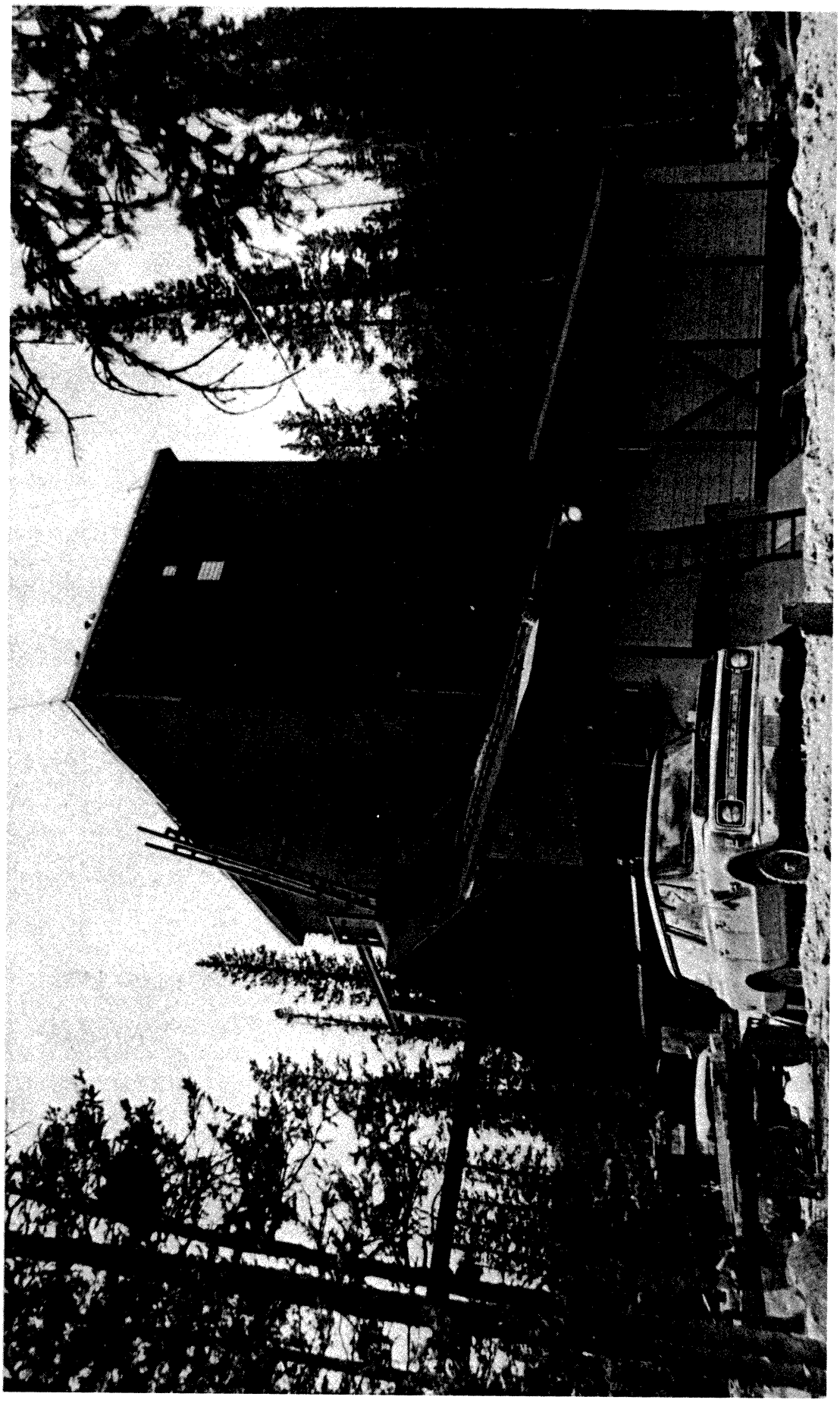

Fig.4 Echo Lake Laboratory

Total Cross Section Experiment

Front View

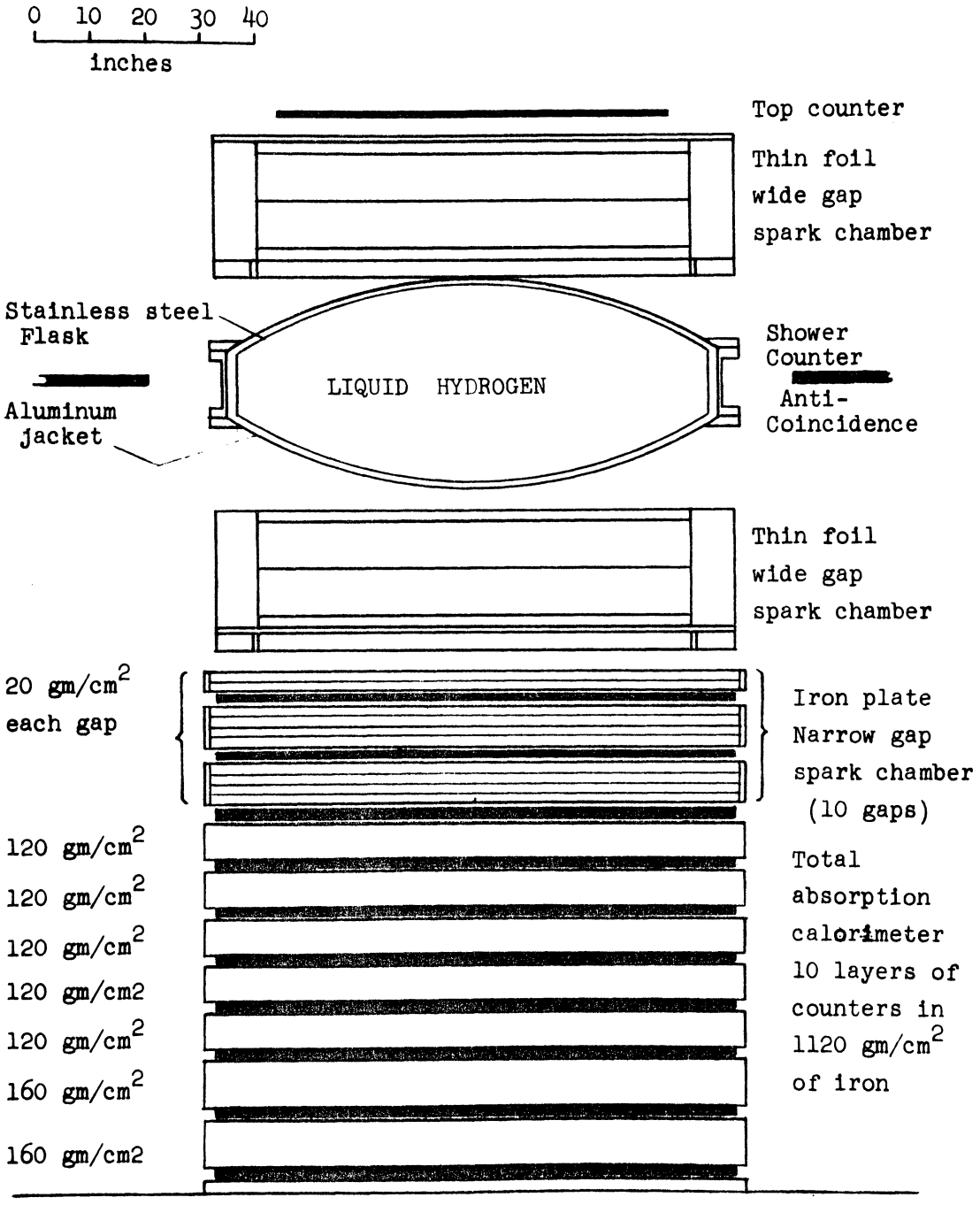

Fig.5 Front View of Experimental Arrangement

no signal from the anti-coincidence shower counter guard ring would constitute a trigger. The thin foil wide-gap chambers which straddled the target would record the incident and out-going particles through two 90° stereo cameras. All of the layer information from the calorimeter was recorded either on magnetic tape or by an array of binary neon lights photographed together with the spark chambers. The apparatus has an effective admittance of 0.94 m^2 sr through layer 8 of the calorimeter, and the trigger rate for charged hadrons of greater than 90 GeV was about 20 per hour.

Besides liquid hydrogen, other targets of carbon, aluminum, iron, tin and lead had also been used. The arrangement was basically a transmission experiment to measure the proton inelastic cross-sections above 70 GeV, together with studies of angular distributions and average multiplicities with various targets and energies. A bonus of this experiment was the precise measurement of energy dependence of proton-iron inelastic cross-section by studying the interaction of the transmitted proton flux in the calorimeter. A detailed analysis of this measurement will be the subject of chapter V.

CHAPTER II

STREAMER CHAMBER

A. THE IDEAL

The ideal streamer chamber is not intended to be a detector for all occasions. A detector will be considered ideal if all its unique properties are abundantly realized.

The very fact that the discharges are decoupled almost guarentees that a streamer chamber will have 100% multiple track efficiency when lateral track spacings are smaller than streamer lengths. This decoupled nature of streamer development undoubtedly allows relative if not absolute ionization measurements.

The near isotropic property of the chamber was well demonstrated by Chikovani et al. [26] when spiral tracks were observed in the magnetic field.

Due to the low density of the gas medium, the chamber is well suited to observe low energy recoil or short lived decaying particles. A 4π detection geometry is possible when targets are inserted into the active volume if the gas is not served as target itself.

All of these good characteristics can be realized if the streamers will produce sufficient light for recording.

B. DESIGN PRINCIPLES

(1) Electrical Requirements:

To achieve the best spacial resolution, it is important that the high voltage pulse be delivered with minimum delay such that electron diffusion will be kept to a minimum. For the sake of achieving isotropy as well as spacial resolution and dense shower efficiency, it is desirable to keep the streamer lengths to a minimum. Furthermore, the streamer brightness at a given length will increase with electric field E, as shown in Fig.6, up to about 15 kV/cm. (27) All these constraints point to the requirement that the voltage pulse must not only be of large amplitude but the rise-time must be extremely short in order to reach the optimum voltage level before the pulse is sharply turned off to limit the streamer length.

Such a requirement can be best realized in small chambers with Marx generator pulsing and crowbar (shunting spark gap) switching. But for a large chamber whose transit dimension is comparable to the pulse width, it should be treated as a terminated transmission line and be pulsed by a Blumlein with impedence matching. In any case, a Marx generator is involved and its development will be the subject of the next

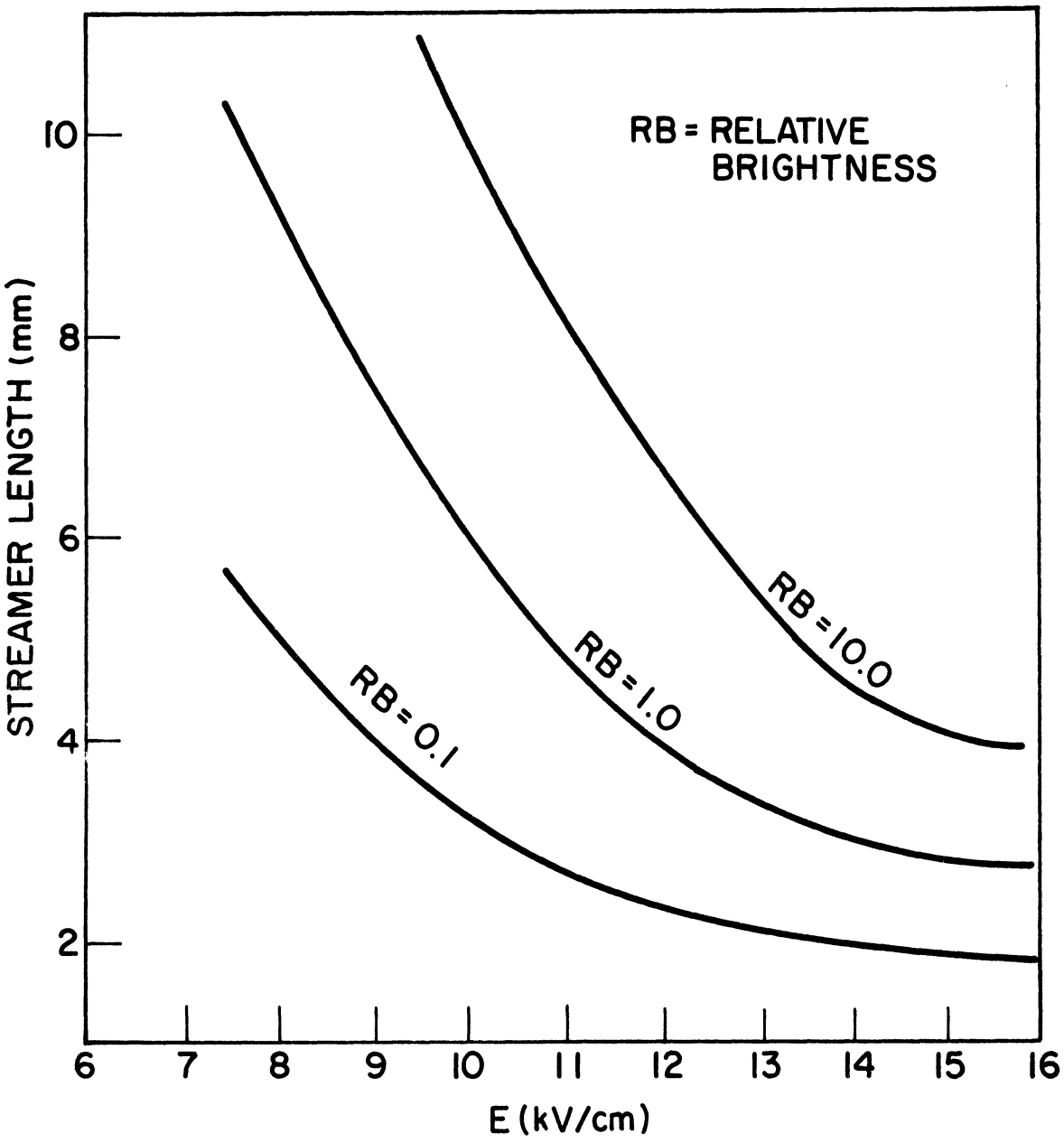

Fig.6 Variation of Brightness with Streamer Length and Electric Field

chapter.

(2) Optical Requirements:

The minimum photon density required to register an image on a very fast photographic film (ASA > 1000) is about 2×10^6 photons/mm^2. [28] In Fig.6, the curve labled with relative brightness = 1 corresponds to the case where 50% of the streamers will be recorded at f:1.5 and film speed of ASA 1500. Thus it is seen that tracks of less than 2 or 3 mm can hardly be recorded by direct photography.

The other aspect of the optical requirement has to do with the depth of field. This is particularly serious with large volume chambers.

Consider a simple lens that is focused at infinity. A point source at a distance H from the lens of focal length F will form an image at a distance q behind the lens. But in the film plane, it will have a circle of confusion of C_F. From geometrical consideration it is seen that

$$H = \frac{F^2}{fC_F} \equiv \text{hyperfocal distance} \quad ,$$

where f is the usual F to aperture ratio.

If the lens is focused on a point at distance p from the lens, there will be far and near planes p_1 and p_2 in which the circles of confusion C_o are the

same:

$$C_o = D\, C_F$$

where D is the demagnification $\approx \frac{p}{F}$.

Explicitly, $$p_1 = \frac{Hp}{H-(p-F)} \approx \frac{Hp}{H-p} ,$$

$$p_2 = \frac{Hp}{H+(p-F)} \approx \frac{Hp}{H+p} .$$

Thus the depth of field

$$\Delta p = p_1 - p_2 \approx \frac{2Hp^2}{H^2-p^2} .$$

To see the relations between Δp, D, f and C_o, we note that

$$\Delta p = \frac{2D^2 f C_F}{1-\left(\frac{p}{H}\right)^2} \approx 2D^2 f C_F = 2DfC_o .$$

This shows that the depth of field Δp is directly proportional to f, D, and C_o, but the maximum value of each is not without constraint. If N denotes the total number of photons and A the area normal to the optical axis,

$$\frac{N_F}{A_F} = \frac{N_o}{A_o} \frac{1}{16} \frac{1}{f^2} ;$$

therefore the maximum value of f is limited by object brightness and film sensitivity. C_o must also be limited to be smaller than the object size in order that the object brightness will not be significantly diminished. Finally, D is limited by film resolution, hence when demagnification is high, space resolution will be correspondingly low.

It is towards the goal of breaking the aforemen-

tioned constraints and the goal of achieving an ideal detector that the following feasibility study of the use of image intensifier with streamer chamber was initiated.

C. DESCRIPTION

A detailed description of the experiment can be found in reference (29). It is intended here to briefly review some general features of that study.

Fig.7 shows the experimental arrangement. The chamber of $23 \times 15 \times 6$ cm^3 active volume was viewed directly by a 3-stage image intensifier. A 90° stereo view parallel to the electric field was photographed by means of a mirror looking through the transparent screen electrode.

The streamer chamber was pulsed by a simple 5-stage Marx generator as shown in Fig.8 and the crowbar shunting spark gap was pre-triggered by a pulse from the first stage of the generator to reduce time-jitters in the switching action. The size of the crowbar gap controled the duration of the pulse hence the length of the streamers.

D. PERFORMANCE

Streamers of any length can be obtained just by a dial of the crowbar. Fig.9 is an overexposed picture of a full length streamer track showing the field of view covered by the image tube and the extent of distortion in-

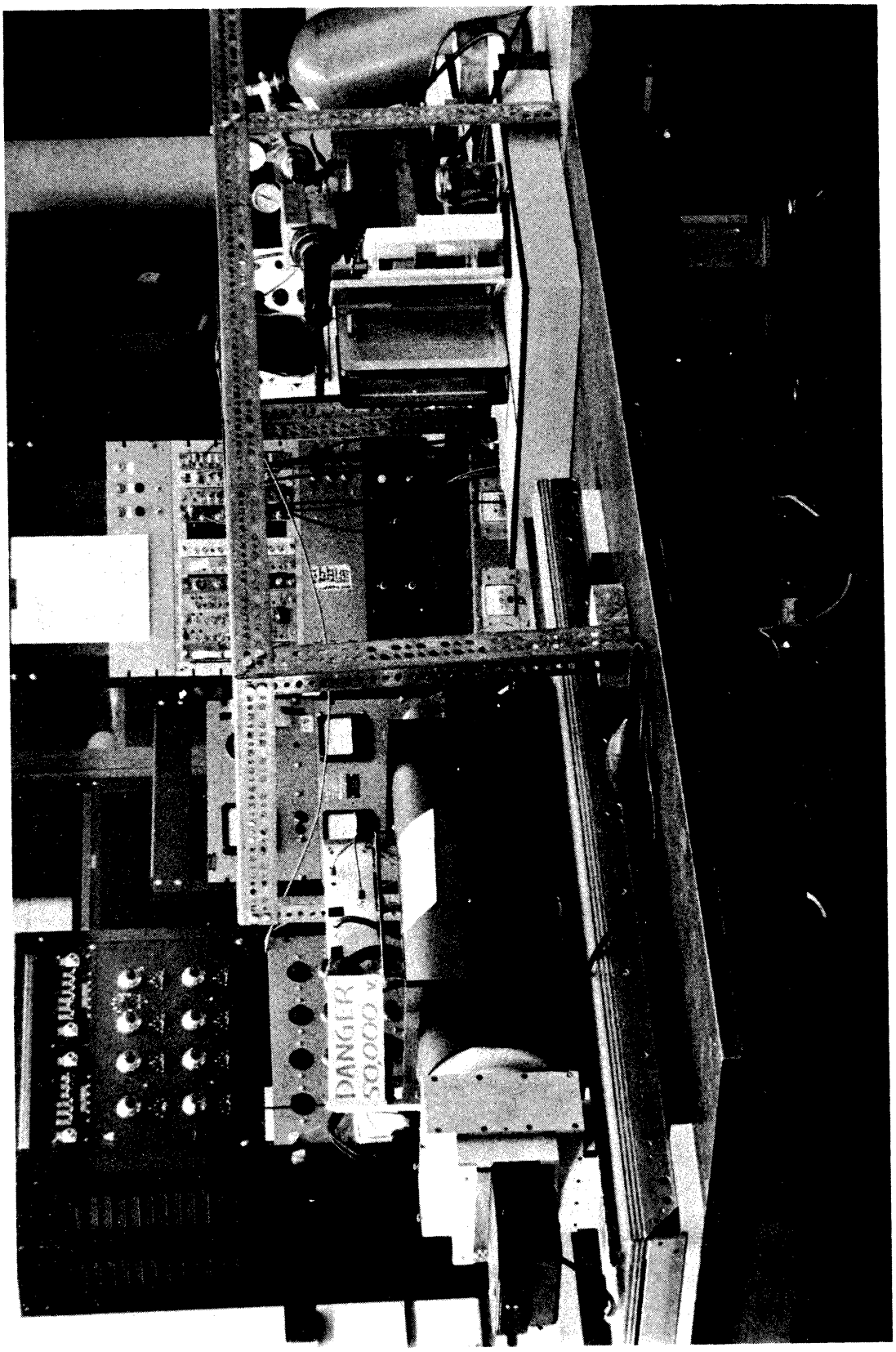

Fig.7 Arrangement of Apparatus with Light Tight Walls Removed

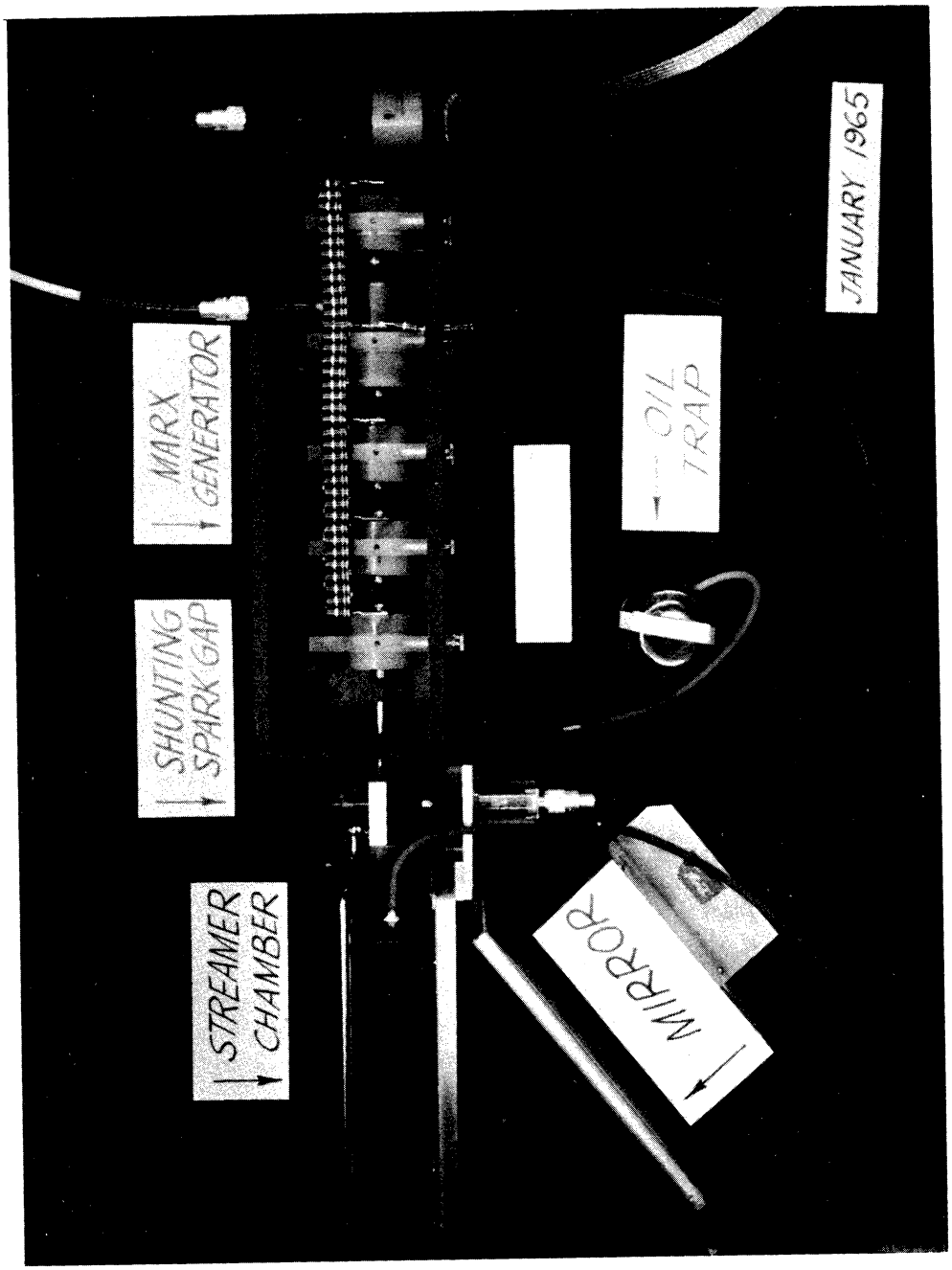

Fig.8 Details of the Streamer Chamber and Marx Generator

volved. Samples of scattering from chamber walls or in chamber gas at various streamer length settings are illustrated in Fig.10-18. They correspond to streamers of about 1.5 mm to 5.5 mm in 0.5 mm increments with f-stops ranging from 4.5 to 16. The control of average streamer length at a given setting is shown in Fig.19.

All the pictures were taken at the same voltage gradient of 17 kV/cm (assuming peak voltage is reached) and comparisons indicate that there is approximately a factor of 2.5 increase in brightness for every mm increase in streamer length.

Some 3 mm streamers have been photographed directly with a 76 mm lens at f:0.87. Assuming that 2×10^6 photons/mm are needed for recording, and taking an effective streamer width to be about 0.5 mm, the number of photons liberated is estimated to be 3.6×10^7.

The observed streamer density along a track was about 6 per cm in a 85-15 nelium (or neon-helium) mixture at one atmosphere. This is less than the primary ion density, but due to fluctuation in avalanche development, not all avalanches are expected to turn into visible streamers within a given time. Unless the gas density is low, there is also a finite probability for avalanches to merge with their close neighbors.

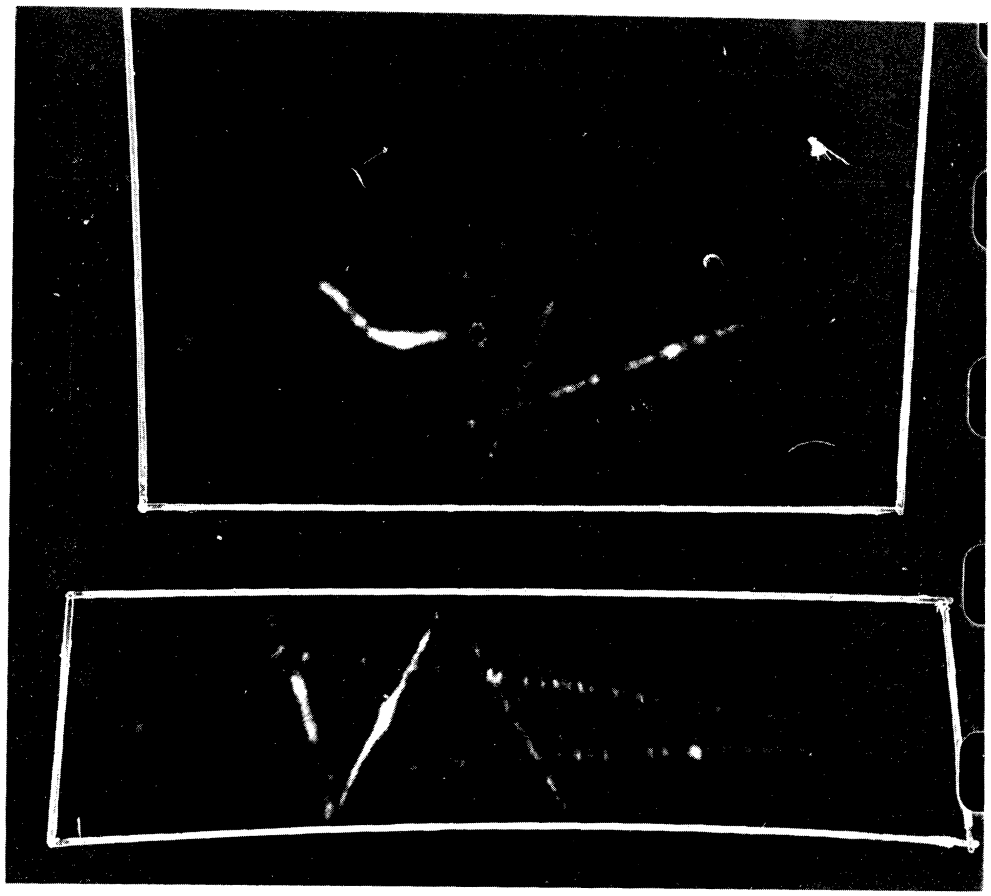

Fig.10 1.5 mm Streamers at f:4.5

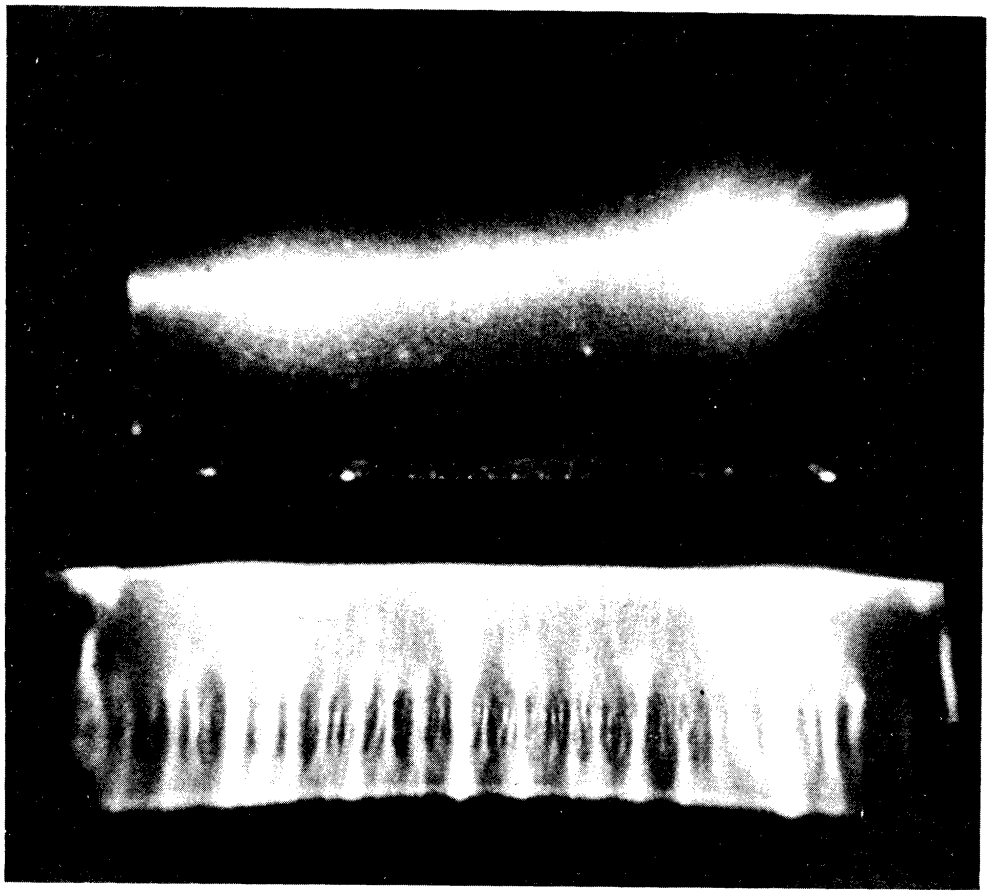

Fig.9 Full Length Streamers

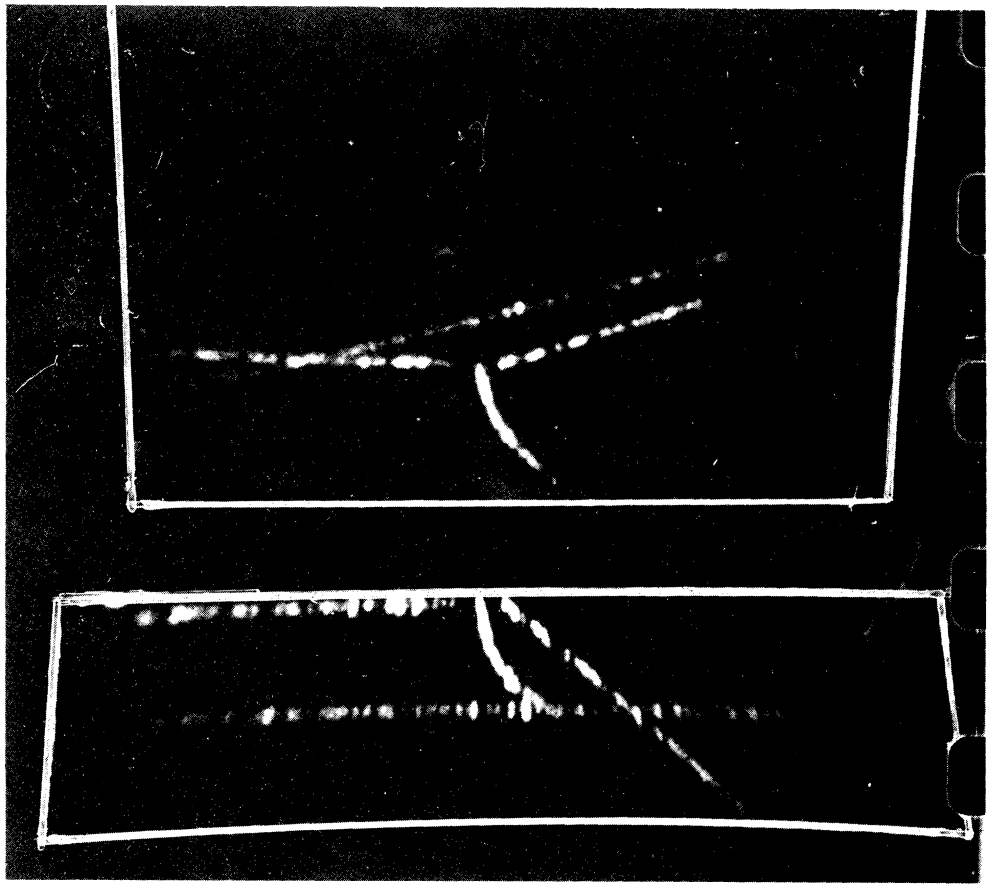

Fig.12 2.5 mm Streamers at f:5.6

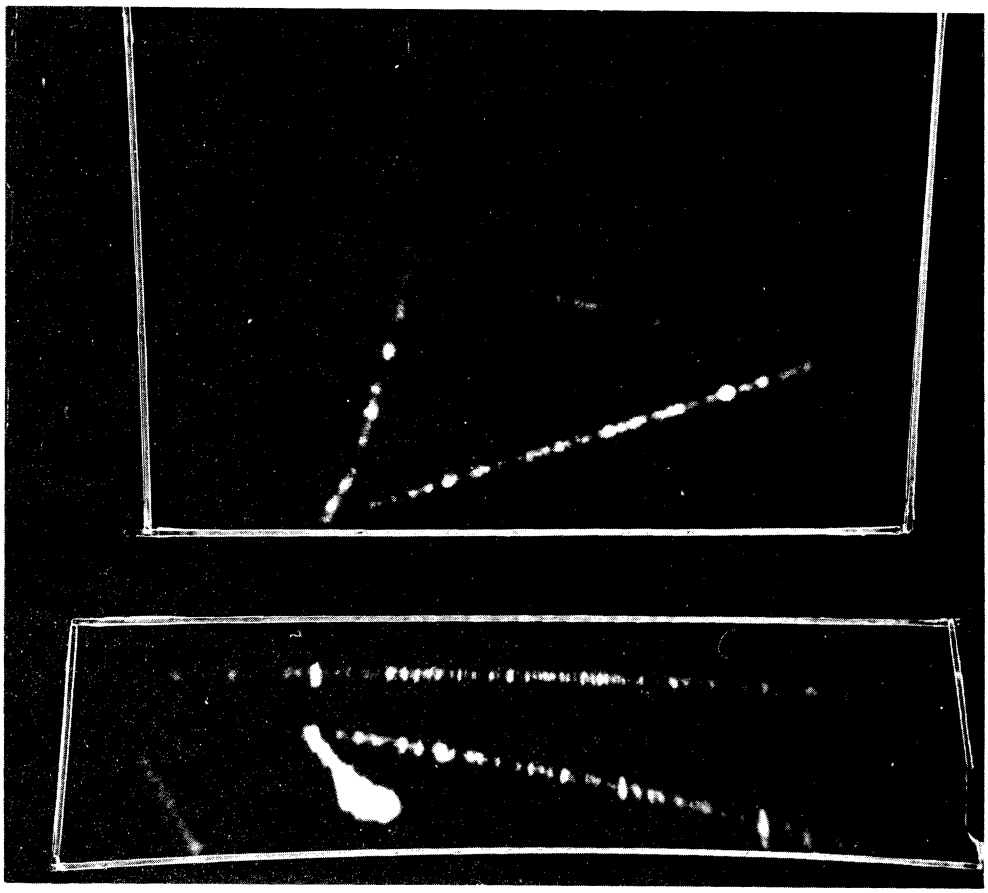

Fig.11 2.0 mm Streamers at f:4.5

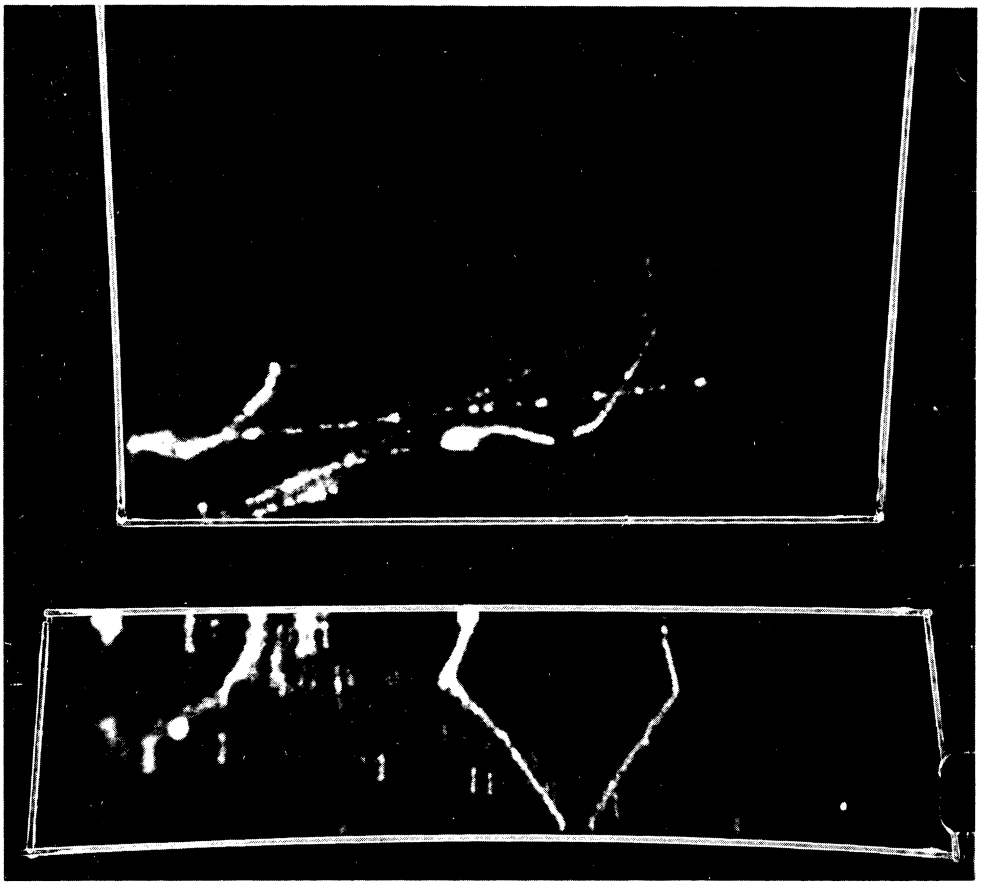

Fig.14 3.5 mm Streamers at f:8

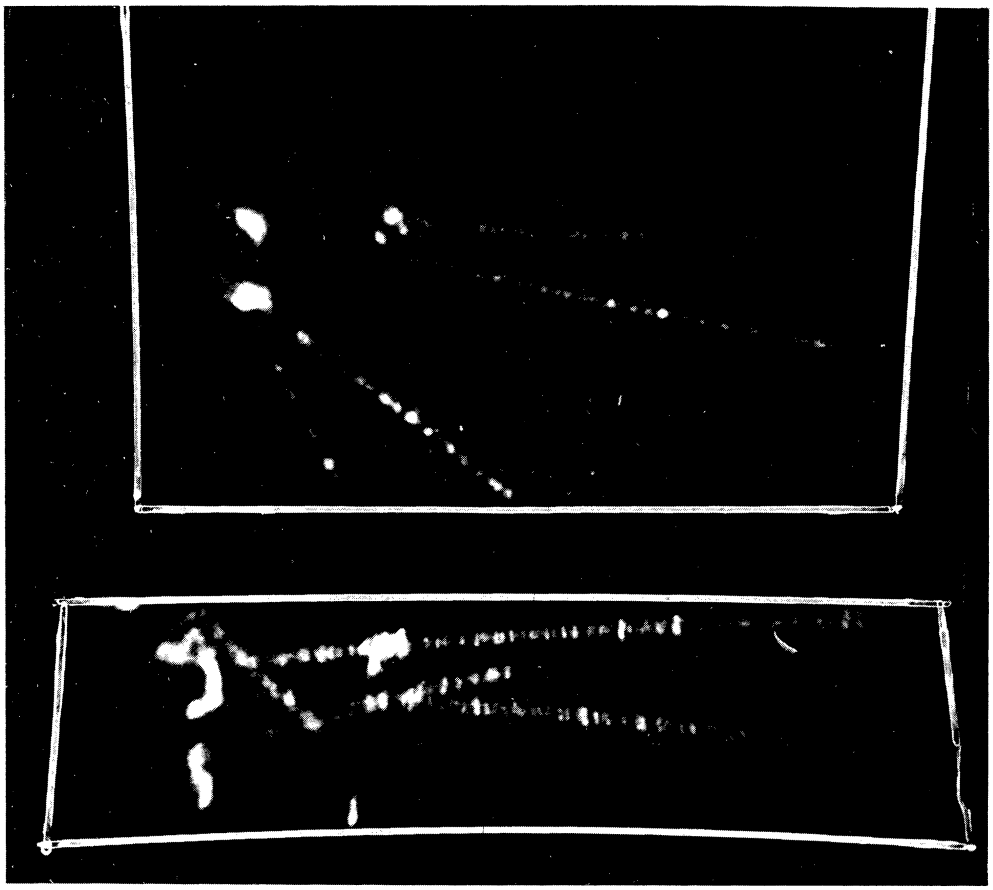

Fig.13 3.0 mm Streamers at f:5.6

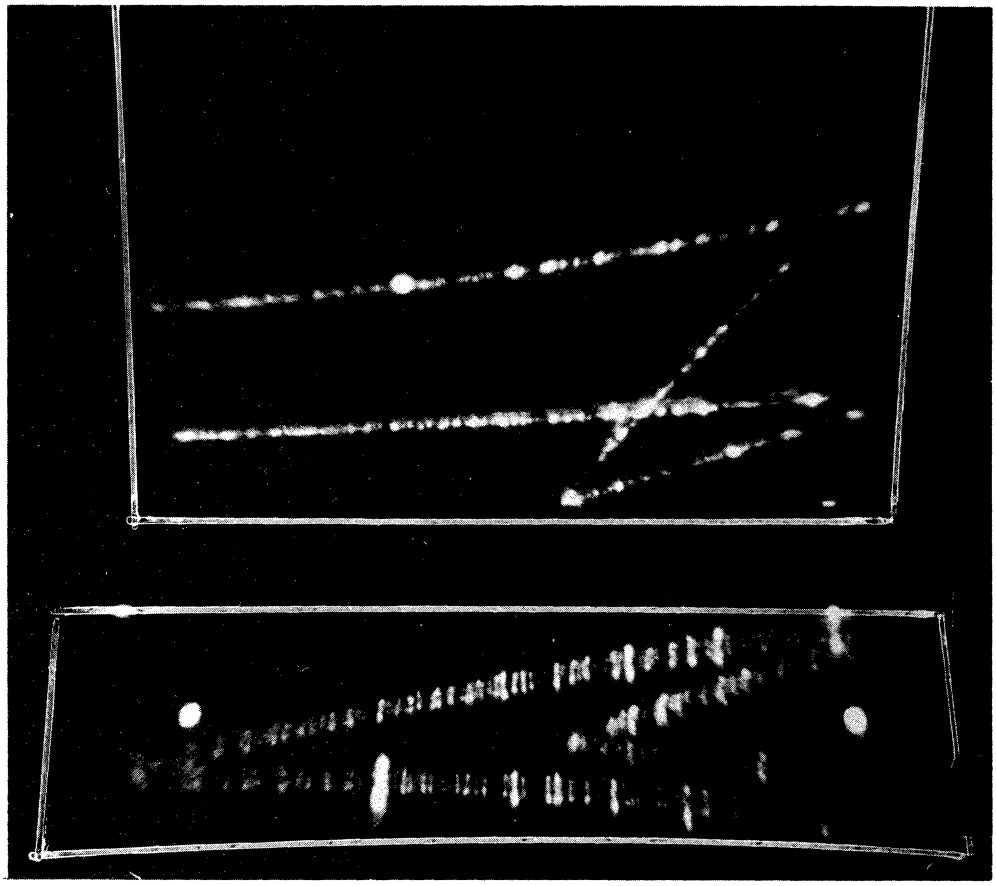

Fig.16 4.5 mm Streamers at f:11

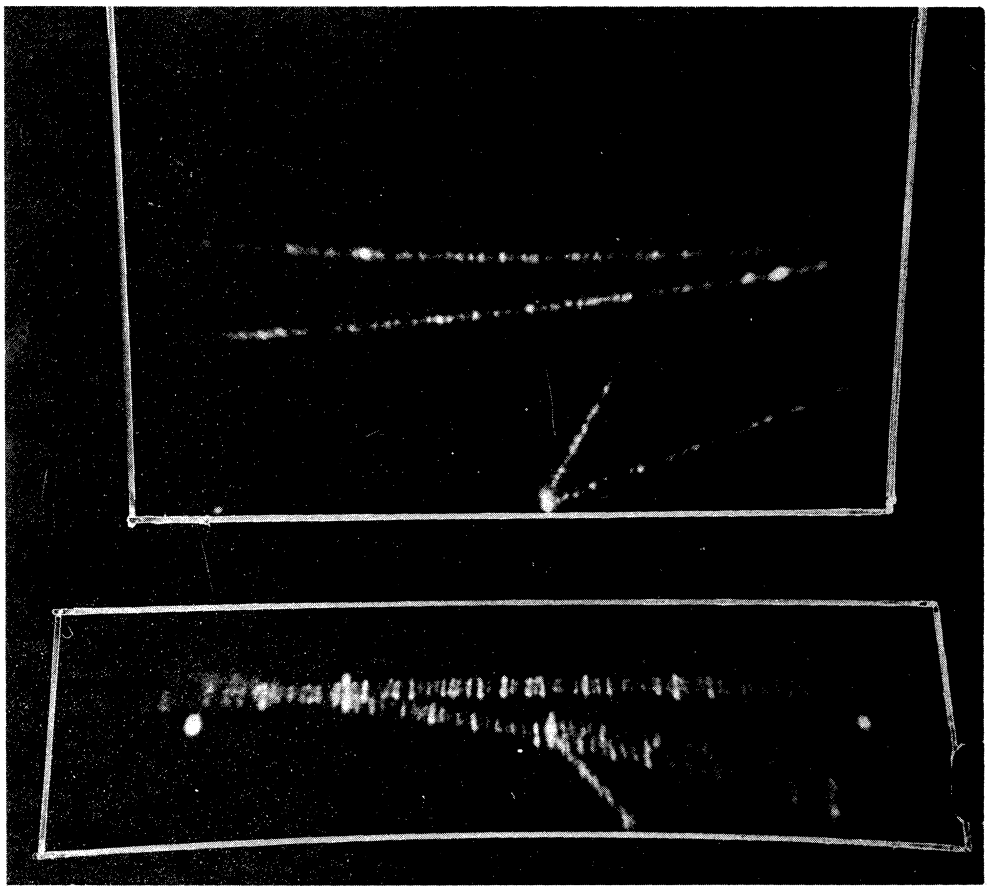

Fig.15 4.0 mm Streamers at f:11

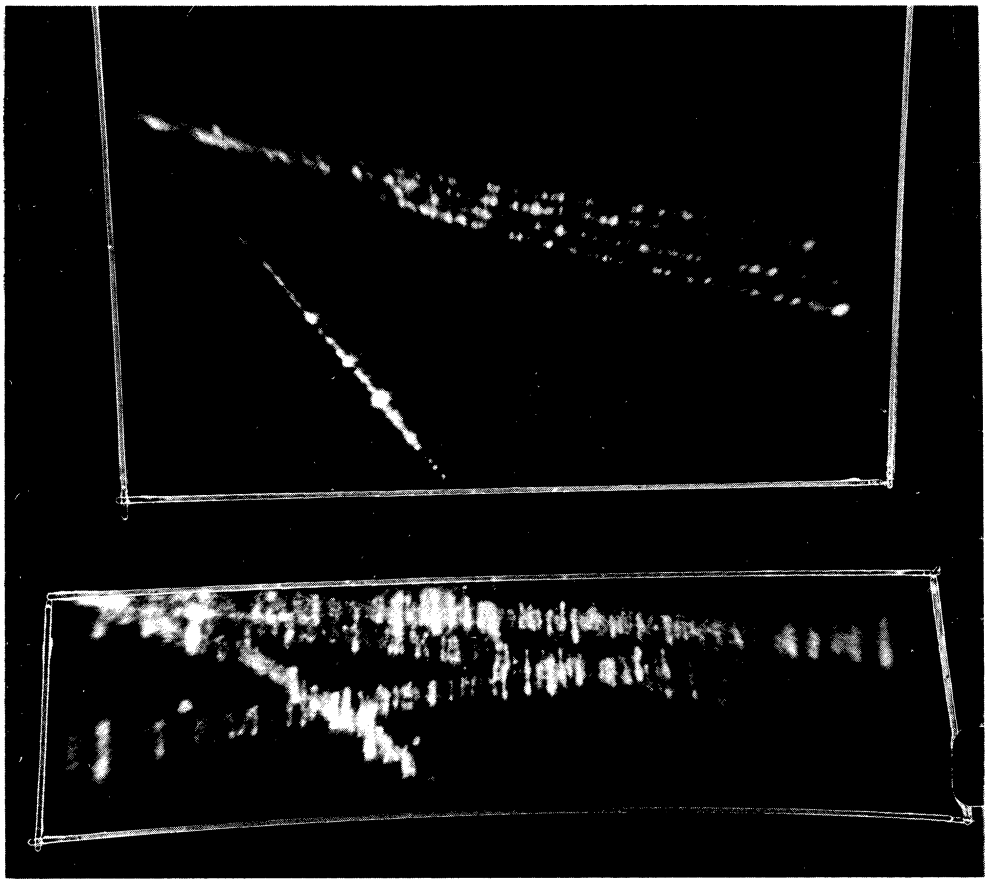

Fig.18 5.5 mm Streamers at f:16

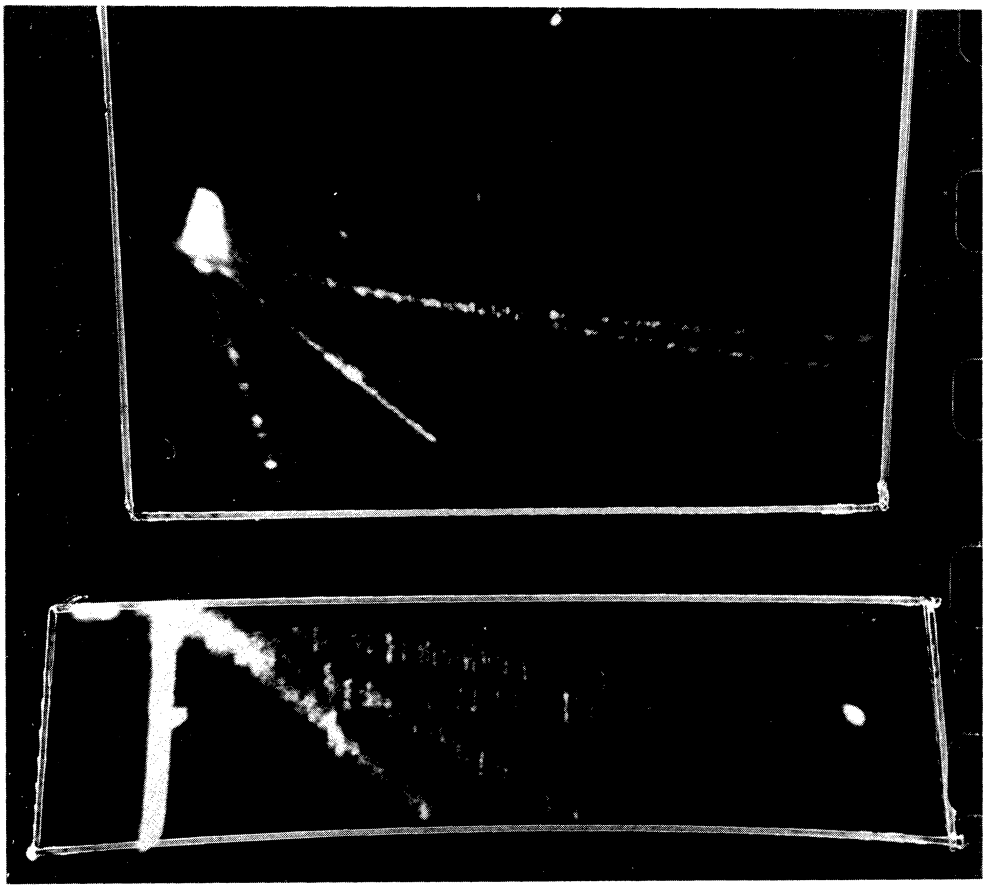

Fig.17 5.0 mm Streamers at f:16

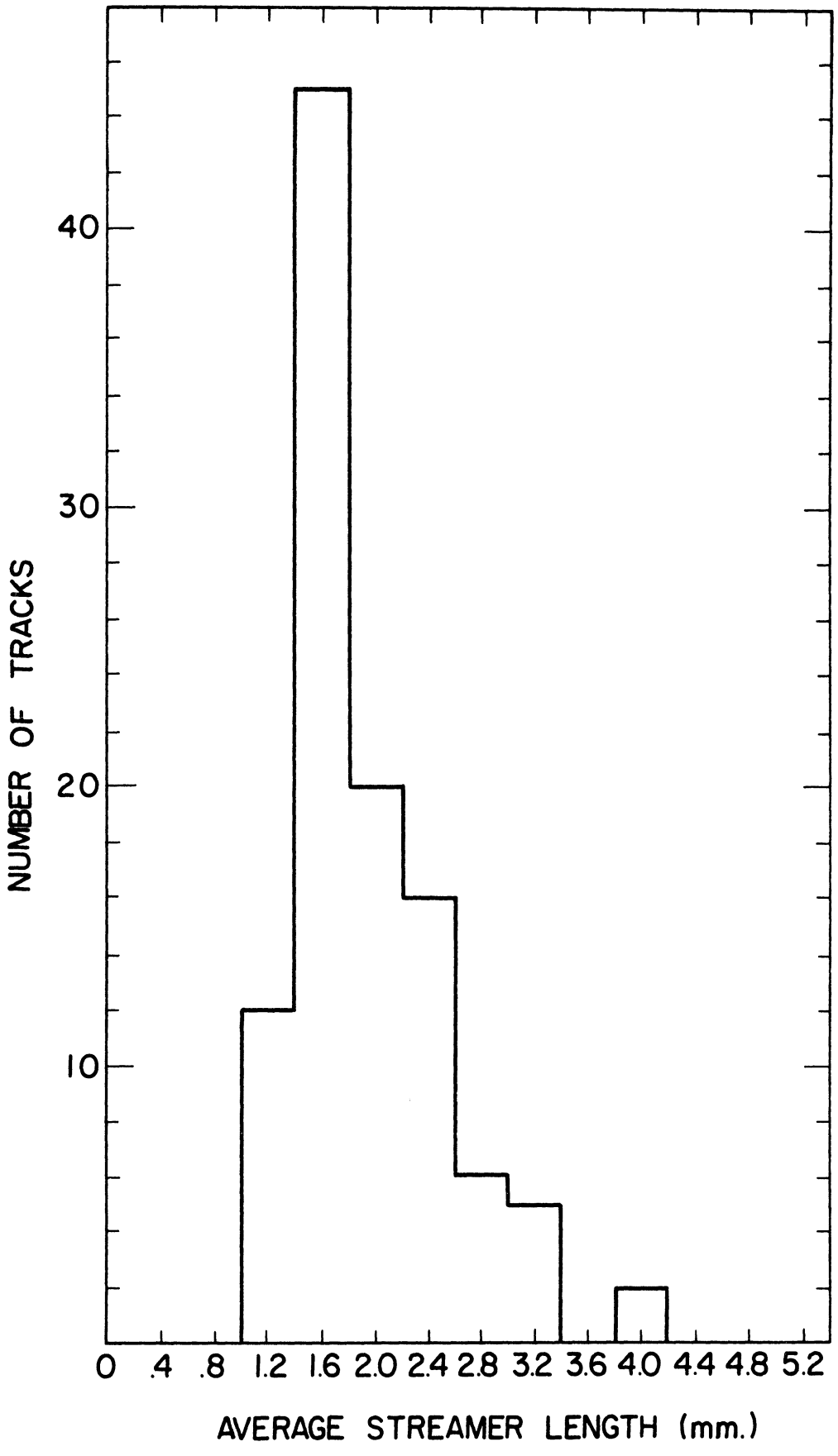

Fig.19 Streamer Length Fluctuations at a Given Setting

E. CONCLUSION

It is concluded that this experiment even in its unsophisticated form has demonstrated the immense potential of the streamer chamber as a research tool. The coupling of the image intensifier certainly has overcome the light output and depth of field weaknesses and paves the way towards automatic digitization.

Needless to say the Marx generator and image intensifier used in 1964-5 were primitive by today's standard. The voltage characteristics were not optimized, which could account for the apparently low light output compared to the observed 10^8 photons for a 1 mm streamer; [30] and the image tube distortion was excessive. But far superior instrumentation is now available, and the intrinsic advantages of the streamer chamber have been realized. Its growing popularity as a detector in experiments at several major accelerators attests to this fact.

CHAPTER III

MARX GENERATORS

A. THE IDEAL

It is clear from the discussion of the previous chapters that an ideal Marx generator must have minimum delay-time and rise-time ($< 10^{-9}$ sec if possible) besides the capability of delivering a peak voltage of hundreds of kilovolts. If the load impedance is low, the generator's internal impedance must be correspondingly low. If the capacitive load is high, its output capacitance must be correspondingly high. Often, the amount of stored energy, compactness and reliability are of concern. Thus there may be many variation of the ideal generator depending on specific applications. Unlike the optical problems encountered with streamer chambers, there is no sharp exclusive nature among the desirable features. It is a question of optimization to attain them all.

B. DESIGN PRINCIPLES

The basic element in the operation of a Marx generator is the switching action by spark-gaps. Spark-gaps are preferred because of their unsurpassed simplicity, speed, and high-current handling capability.

The risetime T of the voltage pulse (10-90%)

switched by a spark-gap can be expressed as [31]

$$T = 2.2 \left(T_L + T_R \right)$$

where T_L is the exponential risetime due to the inductance of the sparks and circuit elements while T_R is the exponential risetime associated with the formation of a plasma in a spark channel. More explicitly

$$T_L = \frac{L}{Z} \ ,$$

where L is the inductance and Z is the load impedance. For a conducting column of length z and radius r (typically 0.1 mm) [32]

$$L = 2x \left(\ln \frac{2x}{r} - 0.75 \right) \text{ [in nanohenry] } .$$

On the other hand,

$$T_R = \frac{200 \ \rho^{1/2}}{Z^{1/3} \ E^{4/3}} \text{ [nsec] } \ ,$$

where E is the electric field in kV/mm,

Z is the impedance across the gap in ohms, and

ρ is the density ratio of the gas to standard air.

Therefore, the risetime can be minimized by keeping circuit inductance and spark lengths to a minimum. Statically, $V_o = Ex$ is to be set on the verge of the spontaneous breakdown voltage of a gap and is proportional to ρx; hence T_R is proportional to $\rho^{-5/6}$, and density in turn is proportional to pressure. Thus high pressure operation will reduce both T_L and T_R.

The final risetime of the output pulse may be further sharpened by a spark gap in series.

The overall delay is of course very much related to the risetime of individual gaps. Under a given set of V_o and x, the breakdown time is determined by the amount of overvoltage and the presence of free electrons.

Free electrons may be provided by a continuous discharge from a corona needle or by ionization with UV photons.

Suppose the DC supply voltage is positive, then a Marx generator of n stages can be used to generate a negative pulse or a positive pulse depending whether it is triggered by shorting the high voltage electrode of the first capacitor to the ground (Fig.20), or to the DC ground electrode of the second capacitor (Fig.21) respectively. In either case an overvoltage of magnitude V_o is applied to the remainder of the circuit. As far as fast pulses are concerned, the circuit to the right of the first gap is an alternate series of (n-1) storage capacitors C_o's and inter-electrode capacitance C_g's. Since $C_o >> C_g$ an overvoltage of $\frac{V_o}{n-1}$ will appear across each gap. When the second gap is shorted, an overvoltage of $\frac{2V_o}{n-2}$ will appear across the remaining gaps, and so on. Thus when n is large, the delay will be long due to the small overvoltage. This difficulty is overcome by the introduction of coupling capacitors C_c as shown in Fig.22.[33] If $C_o >> C_c >> C_g$ then almost the full

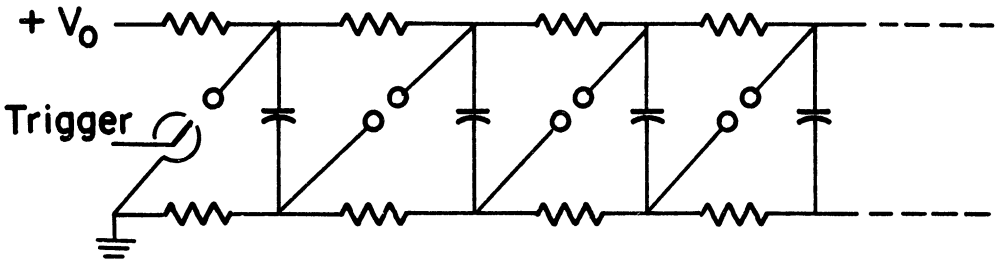

Fig.20 Marx Circuit for Generating a Negative Pulse

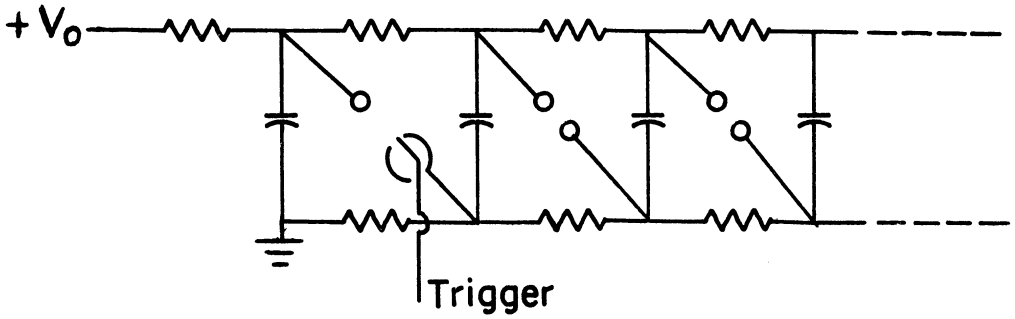

Fig.21 Marx Circuit for Generating a Positive Pulse

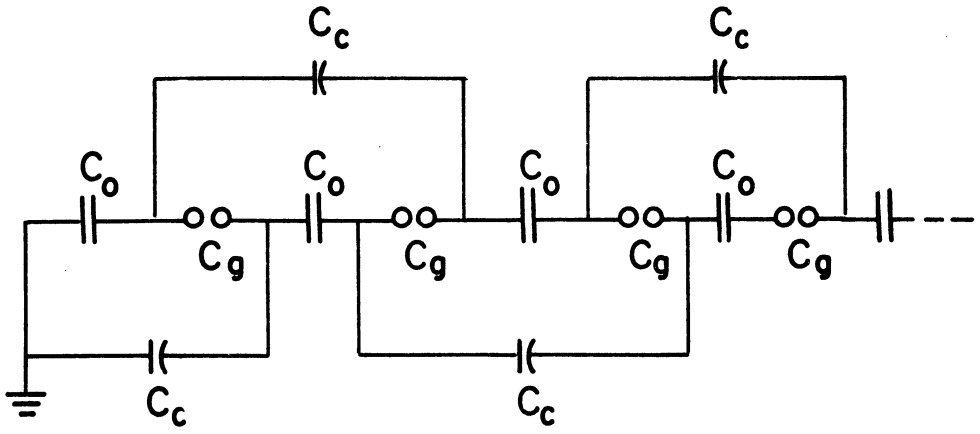

Fig.22 Marx Circuit with Coupling Capacitors

overvoltage will appear across the next gap to be broken down because C_c provides a relatively low impedance path to the ground.

In short, best results can be achieved with small gaps, high pressure, corona source, and coupling capacitors. Topologically, the components should be arranged with minimum circuit inductance and the gaps should "see" each other such that they are linked by UV radiation for fastest action.

When a Marx generator fires into a chamber of load capacitance C_L the voltage across the chamber V is a damped oscillation of frequency

$$\omega = \sqrt{\frac{1}{LC} - \frac{R^2}{4L^2}} \quad ,$$

where L, R and C are the series combination of the load and generator circuit parameters. When the damping is small or for the initial part of the wave, V behaves approximately as

$$V = nV_o \frac{C_o/n}{C_o/n + C_L} (1 - \cos \omega t) \, .$$

Thus the actual gain in peak voltage of V will be leveling off with increasing n when C_o/n becomes comparable with C_L. Again, it is seen that small L lead to high ω hence fast risetime. Sometimes it is also necessary to keep C_o large if too high a voltage is undesirable but sufficient total energy $\frac{n}{2} C_o V_o^2$ must be provided, such as to support very

high multi-particle events in wide gap spark chambers.

For compactness, capacitors are usually made of ferroelectric materials such as barium titanate which has a dielectric constant of about 4000.

Since most capacitors have a height to diameter ratio $\frac{H}{D}$ of less than unity and since all the capacitors eventually will have to discharge in series, the most compact Marx generator will be the size of a cylinder of length L = nH and diameter D. The minimum L is determined by the highest voltage required and the dielectric strength of the material.

For instance, if a pulse of 300 kV is needed and if a convenient 30 kV power supply is available, then n will be 10, and H will be determined by the dielectric strength (for common Sprague door-knob capacitors it is about 15 kV per cm at which field the capacitance will also drop down to 60% of the field free value), and C_o will be determined by D. Note that for a given D, output capacitance and voltage are rather unaffected by variations of n and V_o as long as nV_o is constant. But switching will be faster for large n (within practical limits) because the overvoltage will be large compared to V_o in each gap.

C. MARX GENERATOR DEVELOPMENT

(1) Model A

This simplest version of a five stage generator

is shown in Fig.8 and the circuit was that of Fig.21. Each capacitor (Type 715C, Sprague Electric Co.) has a capacitance of 2500 pf and is rated at 30 KVDC. Copper electrodes were fastened directly to each screw terminal and the gap spacings were adjustable.

The trigger electrode had a trumpet shape with a peripheral gap of 0.1 mm at the center and flush with the cup electrode. A 7 kV trigger pulse would break down this gap rapidly, producing sufficient photoelectrons to break down the main gap.

The gaps were not pressurized. Neither were they optically or capacitively coupled. Nevertheless, it was able to pulse the small streamer chamber reliably with a delay-time of about 70 nsec.

(2) Model B

This generator was designed to drive the $(2m)^2$ thin foil wide-gap spark chambers used in the Echo Lake Cosmic Ray Experiment. Its circuit was similar to that beautiful design by Gygi and Schneider.[33] A two-column arrangement effectively realized the circuits of Fig.21 and 22 with all the gaps seeing each other.

Figs.23 and 24 are the side view and end view of the generator with the pressure vessel removed. The principles mentioned earlier can be visualized as follows:

Imagine a vertical long cylinder of bare $BaTiO_3$

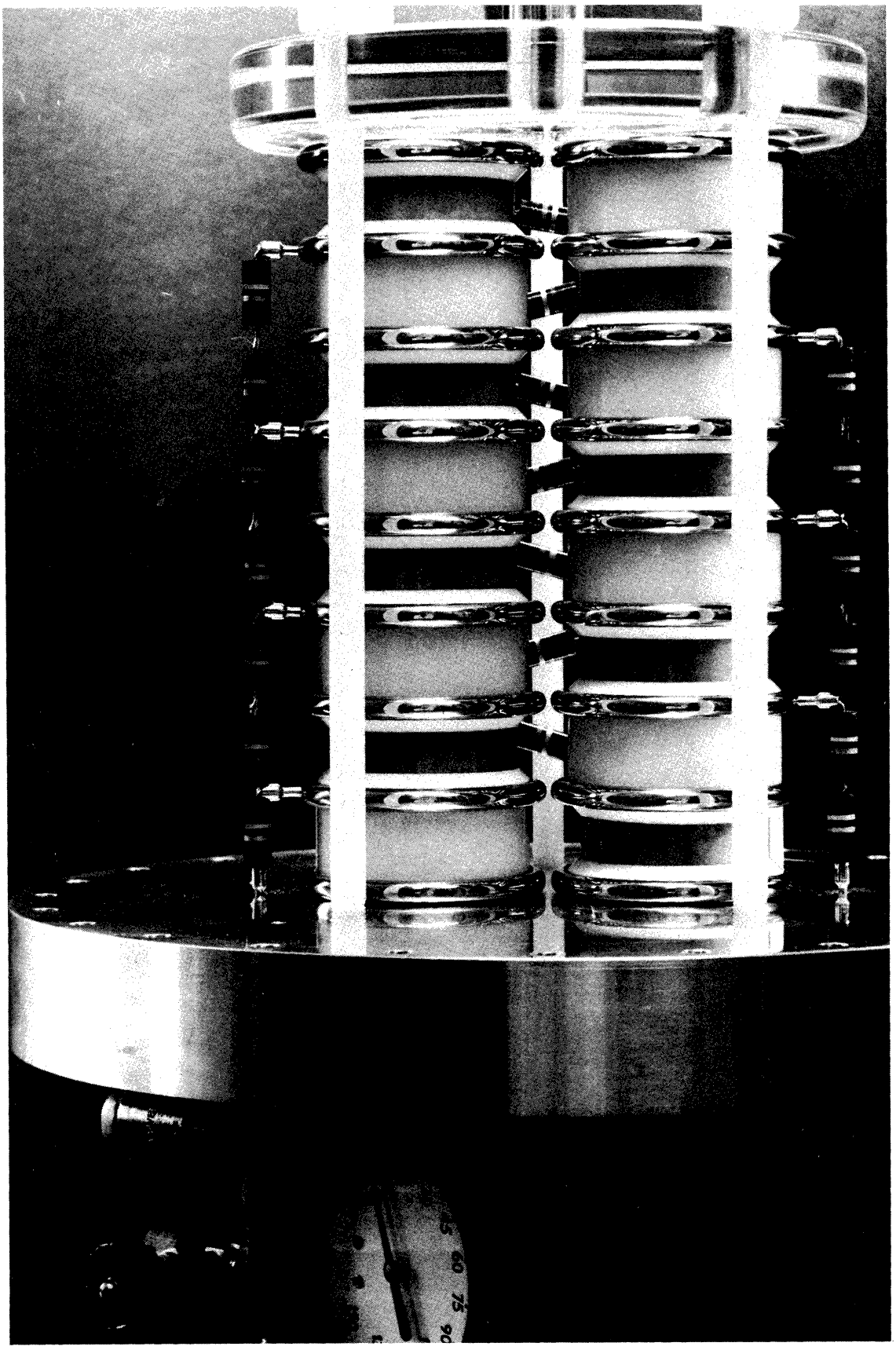

Fig.23 Side View of Model B Marx Generator

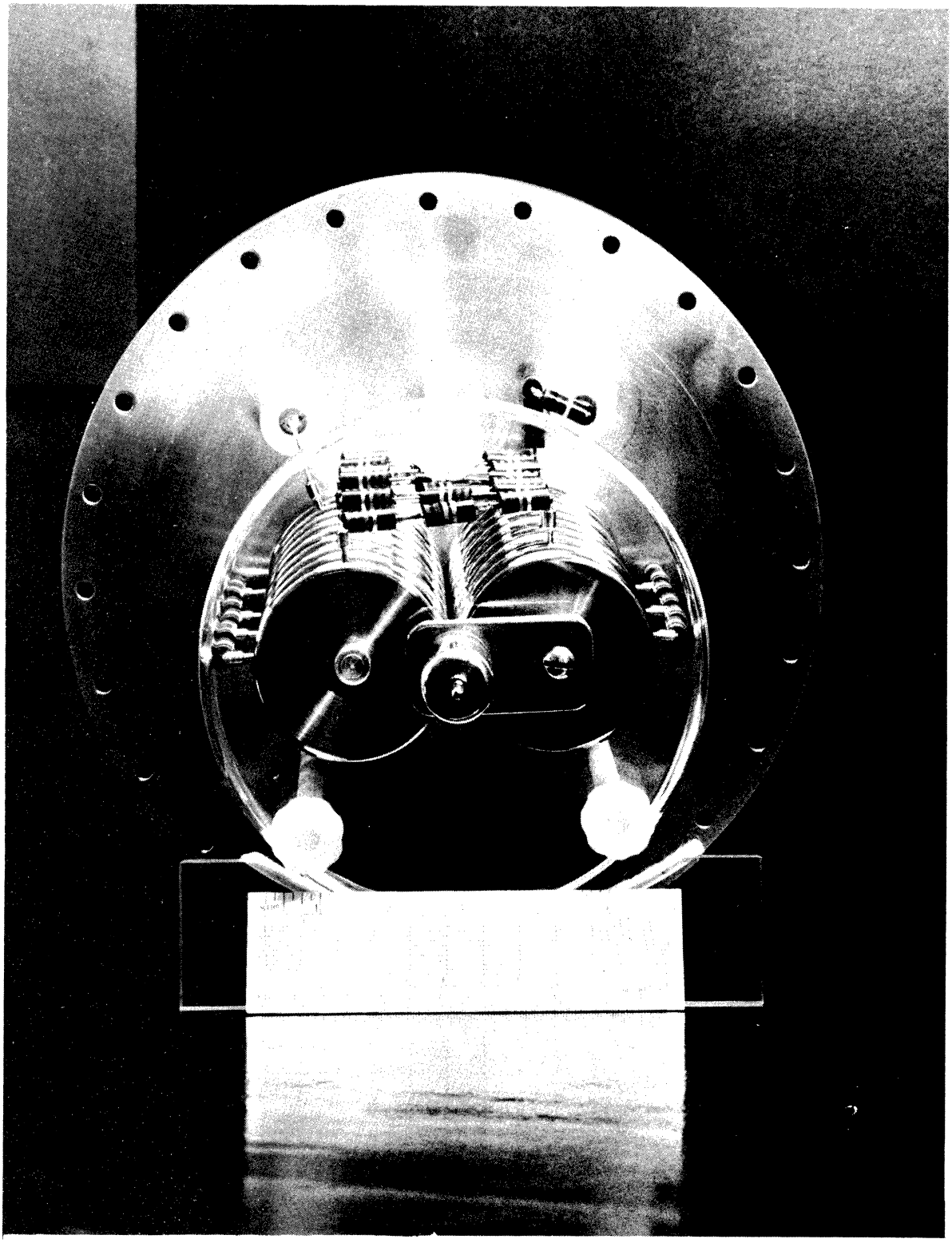

Fig.24 End View of Model B Marx Generator

sliced into eight equal short cylinders. If every other piece is moved sideways and the spaces created are filled with nylon cylinders, there will be two side by side columns. Disc stainless steel electrodes are then inserted between each cylinder to turn them into columns of alternating capacitors whose values are determined by

$$C = 0.885\ \epsilon\ \frac{A}{H} \quad ,$$

where ϵ is the dielectric constant and A and H are the circular area (cm^2) and height (mm) of the cylinder. The white cylinders are nylon ($C_c \approx 5$ pf) and the grey ones are $BaTiO_3$ ($C_o \approx 3900$ pf).

The top electrode of each C_o is charged to V_o through the zig-zag resistor string while the bottom ones remain at dc ground but are isolated from each other. The isolated resistor strings are chosen such that the n^{th} ground electrode from the bottom will see $n \cdot 100$ kΩ to the bottom ground plate. All resistors are connected to electrodes with miniature banana plugs for easy disassembly. It is seen then a voltage V_o appears across each gap of the two columns. When all the gaps are short-circuited by sparks, all the C_o's will be connected in series and a pulse of $8 \cdot V_o$ is generated at the top output electrode. Since all RC time constants are much longer than the switching time, the resistors play no part during the switching moment and behave just like open circuits. And since all the interelectrode capacitance C_g's are only a fraction of a

pf, the condition $C_o >> C_c >> C_g$ is satisfied and full overvoltages are developed across each gap and full amplification is achieved over each column.

Unlike the circuit shown in Fig.21 there is actually no internal trigger electrode. The switching is initiated by applying a negative trigger pulse, which is generated by an external spark gap (15 kV) and amplified by a 3:1 auto-transformer, to overvoltage the first gap. Not shown in the figures is a sharp 1.6 mm tungsten corona needle between the first and second gap. No significant difference was found between electron libration by positive ion bombardment on the cathode and from plain field emission. The corona current was limited by 22 megohms of resistance.

The $BaTiO_3$ cylinders (cores of Type 715C, Sprague Electric Co.) are bare slugs with silver plating on the flat faces and without the usual epoxy encapsulation and screw terminals for compact low inductance assembly. Since their dimensions are not precisely controlled by the manufacturer, teflon rings were press-fitted on each end, then machined to be truly round and concentric in order to fit the recesses in the disc electrodes. 0.25 mm thick indium foil sandwichs were used to ensure uniform disc-silver-plating contacts.

In order to achieve optimum performance, all the gap spacings must be well controlled. Since the amount of

overvoltage is lowest at the lowest stages, the breakdown voltage should be determined by the first gap. This is accomplished by fixing the end electrodes of the columns so that the gap spacings are exactly 1.52 mm. The lowest nylon cylinder in each column has an ecentricity of 0.25 mm between the end circles such that, by controlled rotation, the first gap can be set at 1.45 mm and the second gap at 1.47 mm. Thus there will be a taper of 0.05 mm from the second to the top gap.

The generator has a 9.5 mm aluminum cylindrical pressure vessel with a plexiglas lining of the same thickness and a 7.6 cm opaque nylon window at the HV end. It is pressurized with nitrogen and a pressure relief valve is set at 16 atmospheres. Usually the pressure is adjusted to give a spontaneous breakdown voltage of a few hundred volts above the operating voltage V_o which has a range of 5-30 kV.

(3) Model C

A large volume multi-wide-gap spark chamber presents a larger capacitive load to a Marx generator. Thus a correspondingly larger output capacitance is needed to achieve a required peak voltage. More important is the energy storage requirement when a high peak voltage is not desired.

For example, the two new high-precision chambers of the Echo Lake Experiment each has four 20.5 cm gaps and

a total capacitance of 700 and 800 pf. For such gaps filled with 90-10 nelium at 2/3 atm. the threshold voltage for track formation is about 55 kV. Photographing at f:16, the energy required per spark to register a marginal track on Tri-X film is 0.1 joule. However, 0.5 joule per spark is preferred in actual data taking. This is the motivation for designing the new ten-stage Marx generator with a total capacitance of 0.08 μf. This means that it can produce high quality single particle tracks, at f:16 and 7 kV per stage, or marginally support a dense shower of 250 particles, at f:8 and 25 kV per stage, in all four gaps. Single tracks in pure helium have been photographed at 20 kV per stage and f:90.

The optimum arrangement is a four column design. It is somewhat similar to placing two Model B generators side by side with all 22 spark gaps "seeing" each other and all mirror image electrodes synchronized. The main difference is that there are internal tungsten trigger electrodes with $BaTiO_3$ sleeves in the first gaps of each column and they utilize lower and faster trigger pulses. The built-in redundancy cuts inductance and time-jitter by halves besides improving on the reliability factor. Unlike Model B, a negative pulse is generated because the circuit is similar to the combination of Figs.20 and 22. Light weight aluminum electrodes all with long wearing elkonite inserts are also incorporated.

Fig.25 is a scaled assembly drawing showing half of the mirror image columns and partial construction details. The electrical circuit is also schematically superimposed. Details of the trigger assembly are shown in Fig.26.

Fig.27 shows all the components of a Model C Marx Generator. The enumerated components are described below: (for convenience, dimensions are given in inches)

(1) Pressure Vessel: $3/8$" aluminum cylinder 18 $3/4$" long with 12" ID and welded to end flanges.

(2) Base Plate: 1 $1/2$" aluminum plate, 14" in diameter.

(3) Plexiglas Liner: $3/4$" cylinder, 17 $3/4$" long with 12" OD. It also helps to compress the O-ring in the nylon window.

(4) Nylon Window: Black 3" thick nylon insulator. It can withstand at least 20 atmospheres of pressure.

(5) Output Electrode: 1" aluminum rod with banana plug connections to other rods.

(6) Pressure Control: Safety relief valve is set at 16 atmospheres.

(7) Bolts: $1/4$-20 holochrome bolts, 2 $1/2$" long. The base plate is fastened to the pressure vessel by 24 of these.

(8) Trigger Cables: RG-8 cables with banana plug connections. They bring triggers from the Science

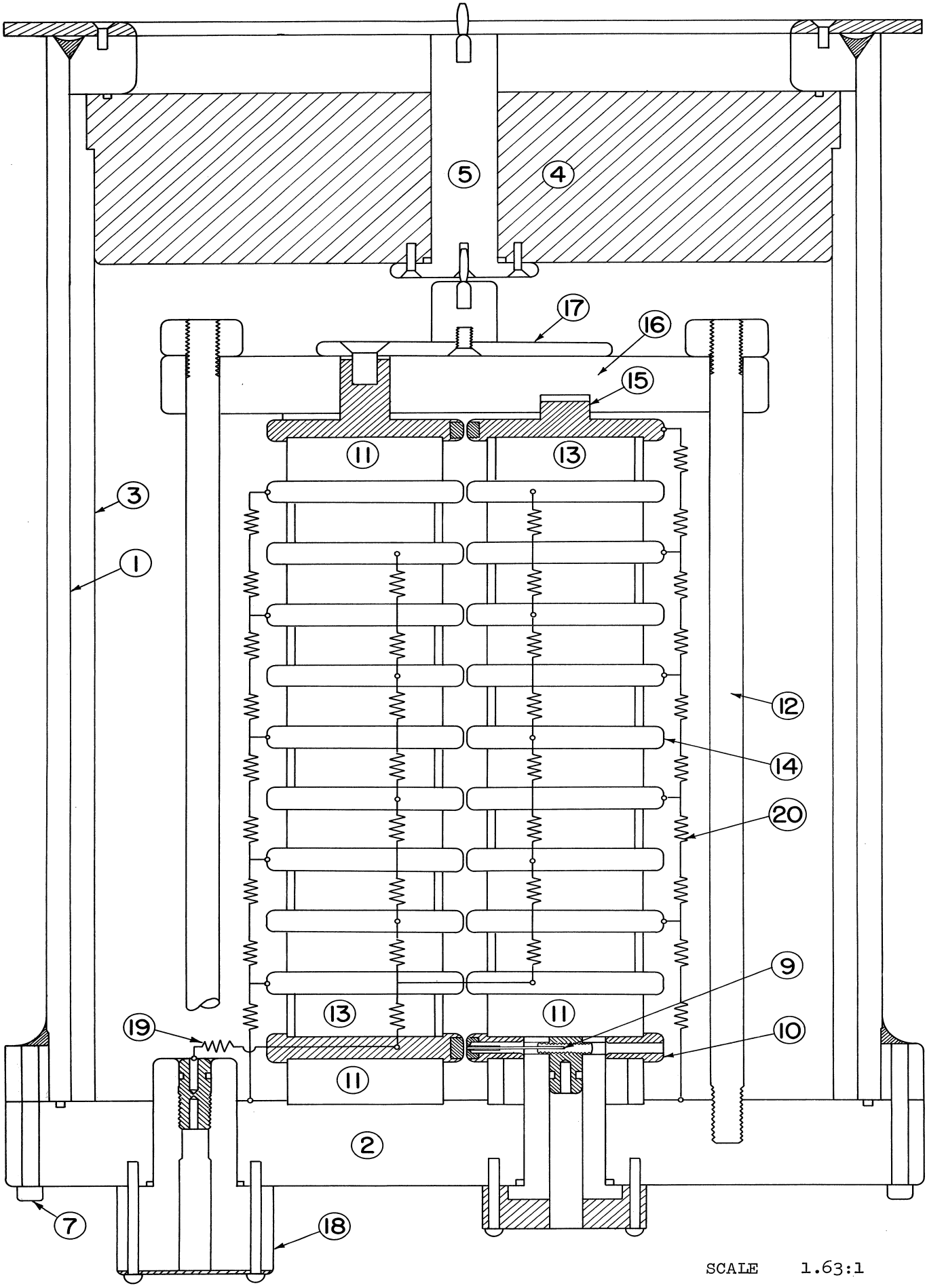

Fig. 25 Partial Assembly Drawing of Model C Marx Generator

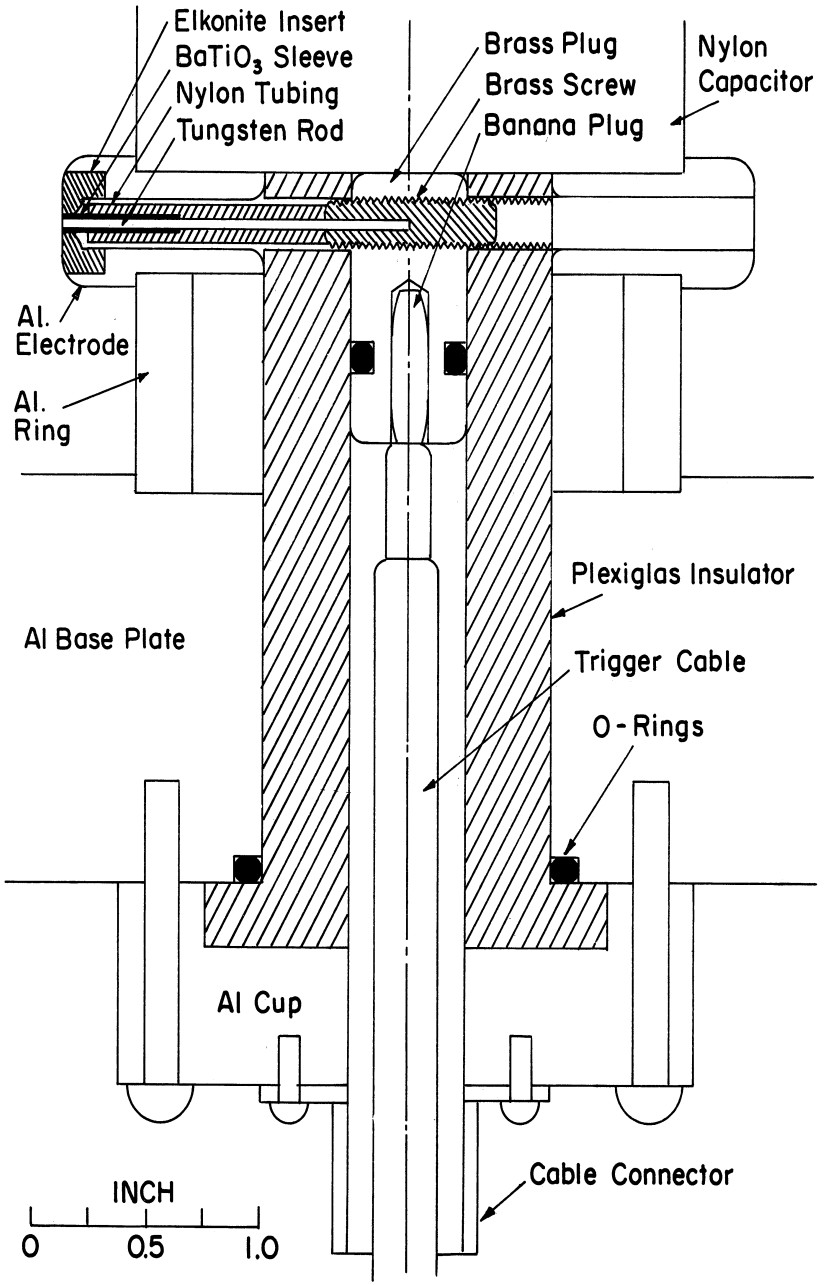

Fig.26 Details of Trigger Assembly of Model C Marx Generator

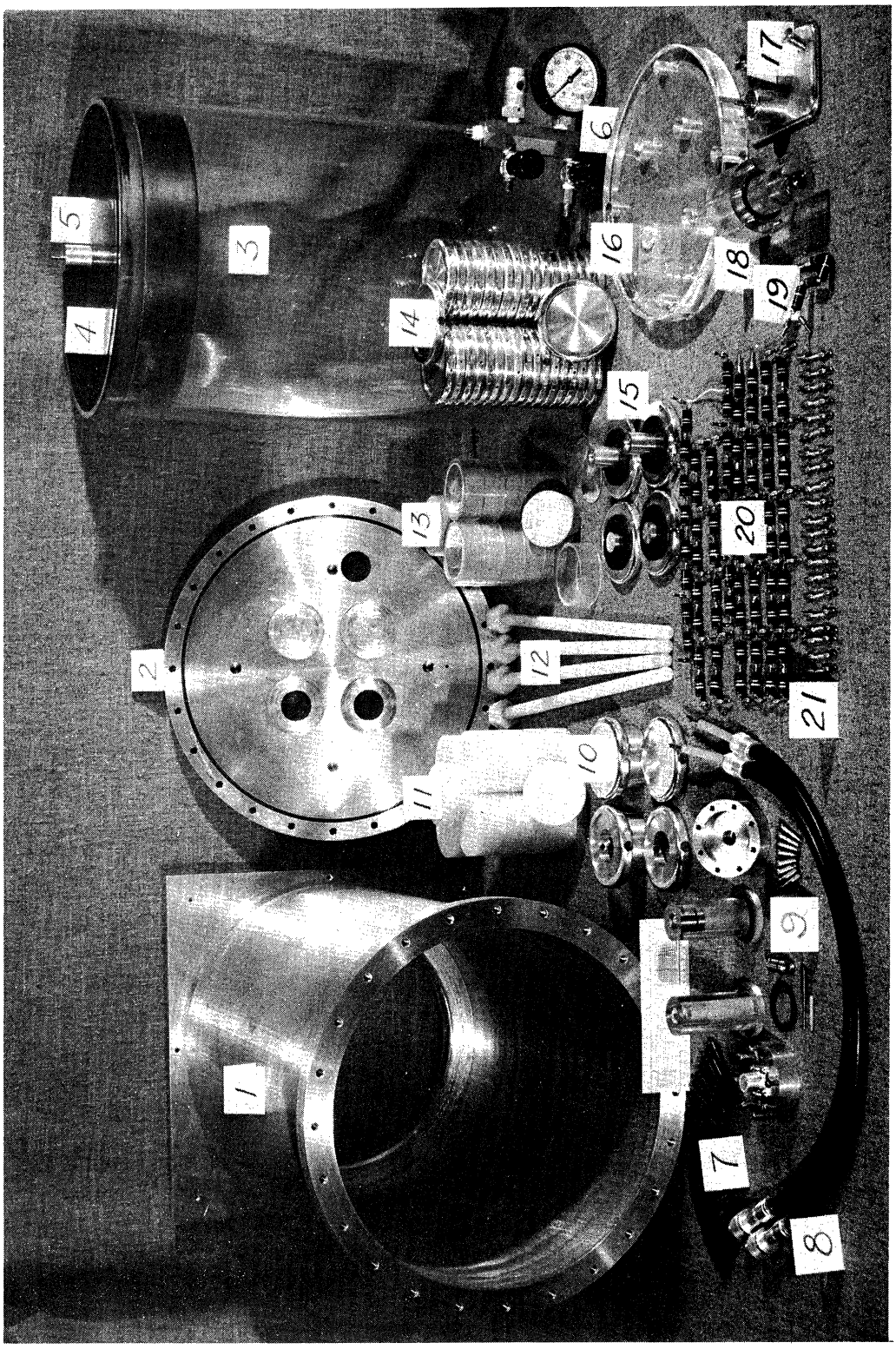

Fig.27 Complete Components of Model C Marx Generator

Accessory Spark Gap Pulser.

(9) Trigger Components: As it can be seen in Fig.26 the brass plug which receives the trigger cable is being pushed outwards by the inside nitrogen pressure, thus good contact is maintained with the screw head of the trigger pin. The tip of the $1/32$" tungsten rod has a thin $BaTiO_3$ sleeve and fits snuggly into the center hole of the first ground electrode. The high dielectric constant of the sleeve causes a very intense field concentration at the thin air space, resulting in a rapid discharge at the tip of the trigger electrode. A 1.2 kV trigger is needed in an unpressurized gap. With the gap pressurized, there is no significant reduction in delay-time beyond a few kV.

(10) Trigger Electrodes: $1/2$" aluminum discs with $3/8$" elkonite inserts.

(11) Nylon Capacitors: 2 $3/8$" diameter, 0.850" high. They serve as coupling capacitors of $\sim$ 5 pf, ensuring full overvoltages be developed across each gap. The lowest two in the column have a 0.010" eccentricity between the two ends so that gap spacings can be precisely controlled by their relative rotations.

(12) Tie Rods: $1/2$" nylon rods with threaded ends and nuts, 14 $1/2$" long.

(13) Barium Titanate Capacitors: 20 capacitors of silver end platings. The sides were painted with glyptal

resin. Since they are not perfectly round, they are made to sit loosely in plexiglas rings that are machined to be truly concentric cylinders to fit the recesses in the electrodes. The vertical spacings are maintained by the $BaTiO_3$ with 0.010" indium foils sandwiched between electrodes. It was necessary to sort these capacitors according to their varying thickness such that the four columns will be equally tall.

(14) Electrodes: $3/8$" aluminum discs with $5/16$" elkonite inserts. They are 3" in diameter and recesses of $1/16$" deep are machined into both sides for alignment purposes.

(15) Top Electrodes: They fit the top plate to locate the four columns. $1/8$" thick rubber gaskets are used to assure even compression in each column.

(16) Top Plate: 1" plexiglas disc, $9\ 1/4$" diameter. It maintains the top electrode spacings and holds the columns in position by means of four tie rods.

(17) Connecting Plate and Rod: It unites the outputs of both columns into the output electrode.

(18) High Voltage Inlet: Plexiglas insulation with brass plug at the center to receive banana plug connection from the dc power supply.

(19) Charging Resistors: Four 1 megohm resistors to match the current capacity of the power supply.

(20) Isolation Resistors: All 100 kΩ 2W resistors. They play no part in the switching circuit except to isolate the stages during the discharge and allow them to return to equilibrium afterwards. Miniature banana plug connections are for easy disassembling.

(21) Synchronization Wires: They connect all mirror image electrodes even though they are only 0.010" apart.

Figures 28 and 29 illustrate the two views of an assembled generator.

D. PERFORMANCE

Three Model B generators were built for the Echo Lake Experiment. One had survived four years of continuous operation without any servicing. Another one, due to a faulty HV connector from the triggering spark gap, had been suspected and had its electrodes cleaned twice. The spare third was never needed.

Two Model C generators were built to drive the new multi-wide-gap spark chambers and are currently in operation with 100% efficiency even when V_o is set at 30% below the breakdown voltage.

Two of the Model B generators will be triggered in parallel to drive a two ($2 \times 2 \times 0.18$ m^3) gap chamber, whose middle electrode has a 6.35 mm lead sandwich for studying neutral particle production in energetic interactions.

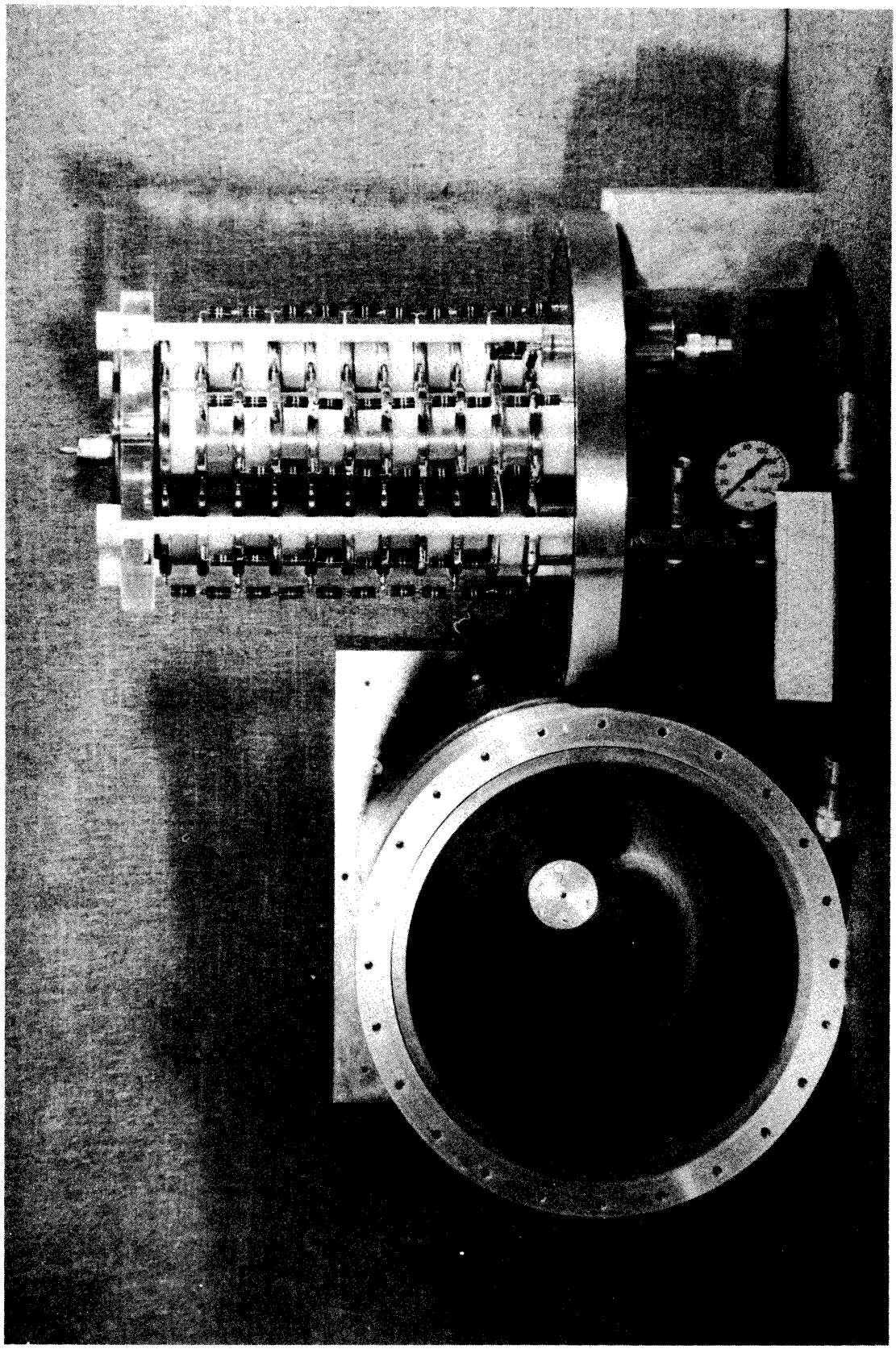

Fig.28 Side View of Model C Marx Generator

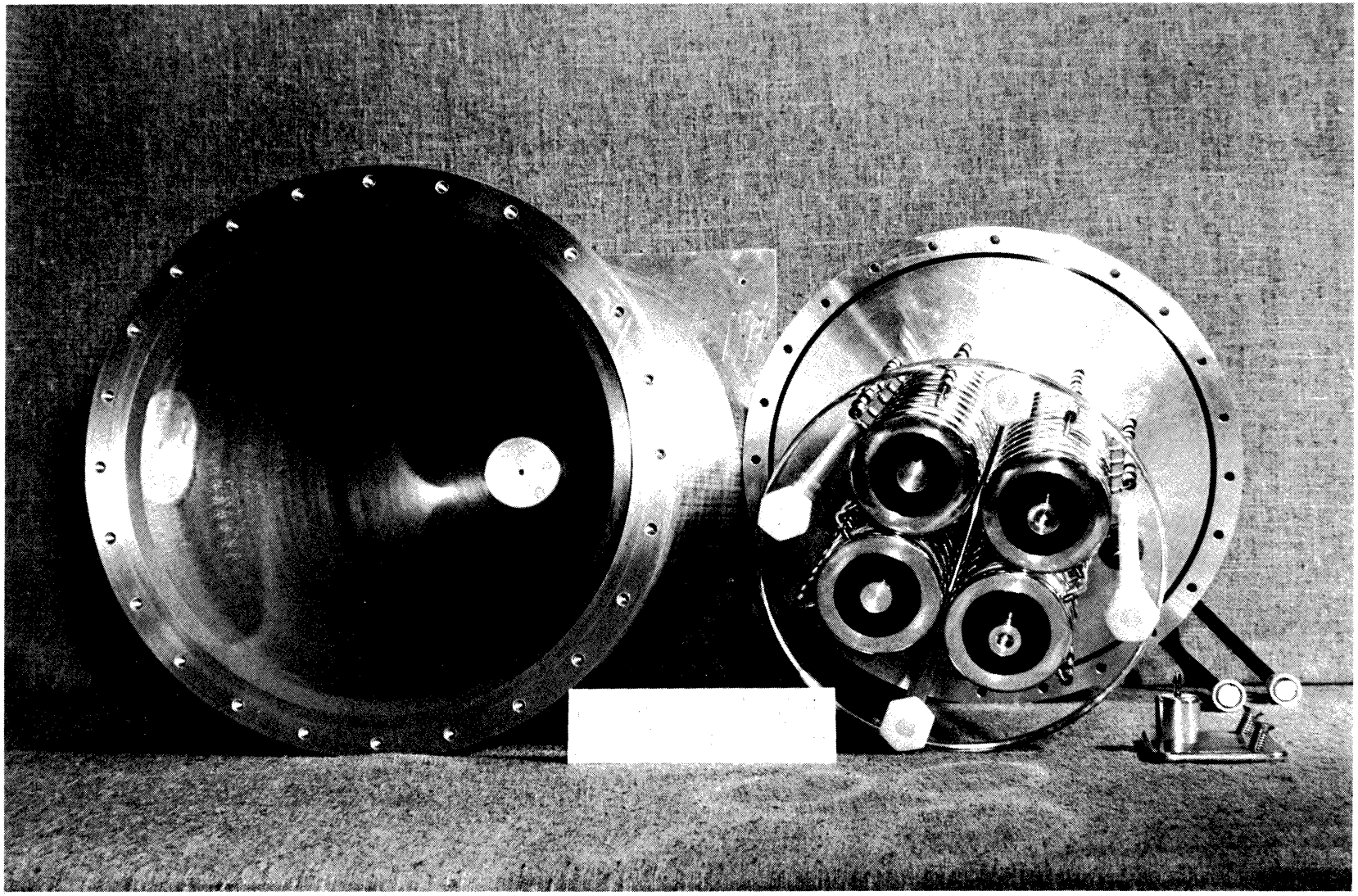

Fig.29 End View of Model C Marx Generator

A cylindrical transmission line with gold plated capacitive divider probe and liquid teminating resistors was constructed to measure the risetime of the generators. But due to conflicting schedules, it was never completed. Instead, the risetime was crudely estimated from the signal tapped off the voltage dividing resistor string at the corner of a thin foil chamber. If one could take the risetime as one half the period of the ringing frequency, then it would be 4 ± 4 nsec. The error reflects the uncertainty in the oscilloscope trace.

The delaytime of the Model C generator has been measured as a function of trigger voltage. It was done by placing a pickup coil directly next to the Science Accessory Pulser, which was triggered by muon coincidence, such that the signal from the firing of the Marx generator will have an opposite polarity to the signal from the firing of the spark gap. This eliminated any cable corrections and the zero crossover point was markedly distinct. The zero-delay position was varified by turning off the HV supply to the Marx Generator. The pressure of the generator was set such that spontaneous firing will occur at 12.8 kV per stage. At this level, no attenuators or change of scale was necessary because the two pickup signals had about the same magnitude. The result of the measurement is shown in Fig.30. It is observed that operating at 300 volts below spontaneous firing, the delaytime was zero with a 3 nsec uncer-

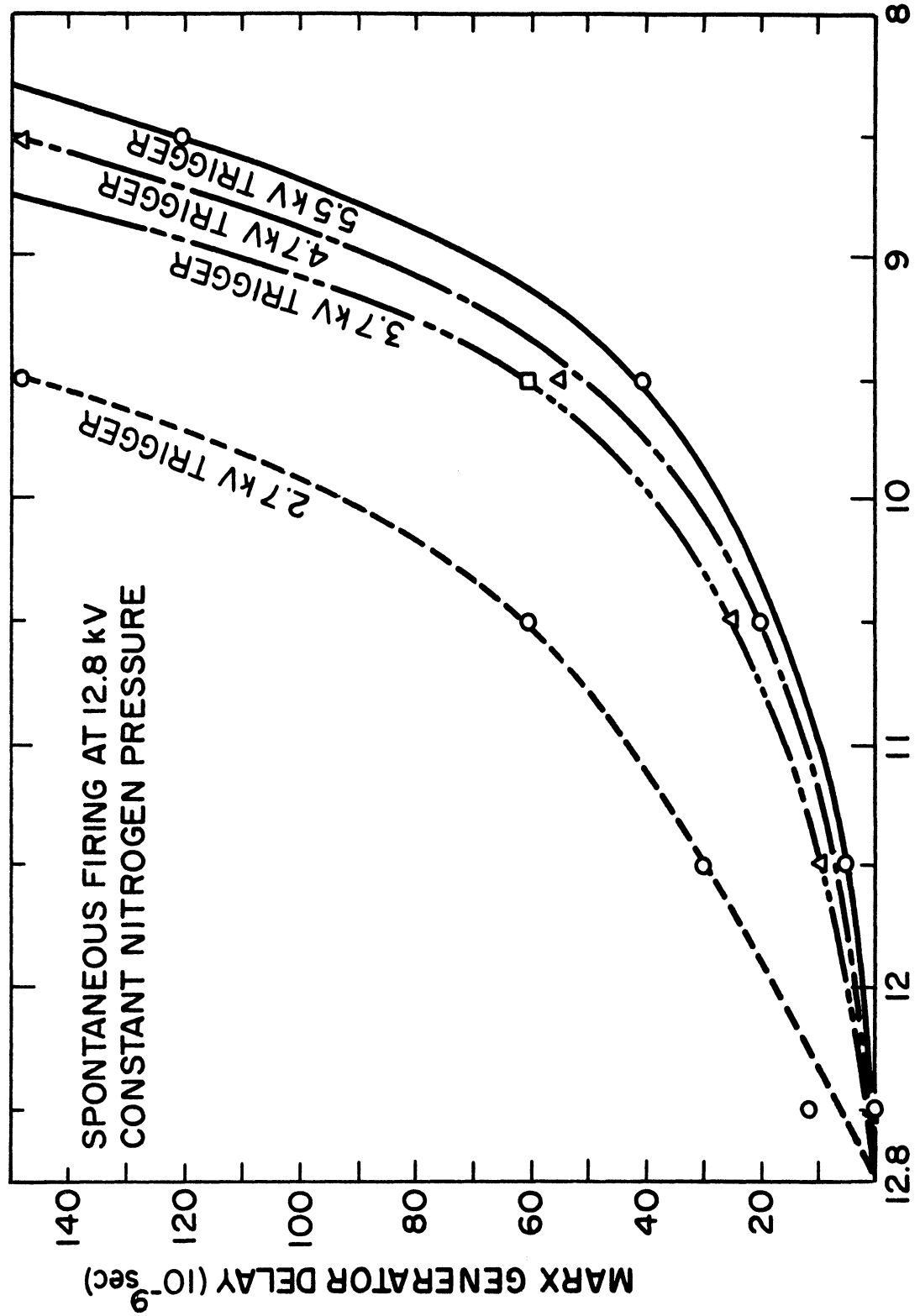

Fig.3C Variation of Delaytime with Trigger and Bias Voltages at Constant Pressure

tainty of the oscilloscope trace; time jitter was only observable for V_o's at a considerable ($\sim$ 20%) margin below breakdown.

E. CONCLUSION

It is seen that based on simple design principles, Model C has reached a fairly high degree of optimization in fulfilling the goals of supporting other members of the Trio. If subnanosecond risetimes are really desired, one has to be much more concerned with impedance matching and special care in preparing for the output gap.[34] Another feature that may be desirable in other applications is that of rapid cycling. But this is usually done by proper energy storage and switching external to the Marx generator.

CHAPTER IV

WIDE-GAP SPARK CHAMBERS

A. THE IDEAL

As we have noted in chapter I, a wide-gap spark chamber has some distinct advantages and disadvantages.

In the first place, the formation of a spark channel virtually wipes out all ionization information except perhaps allowing crude estimates by spark width measurements. Secondly, the formation of a spark channel depends on the linkage of neighboring streamers; since streamers propagate in the direction of the local electric field, isotropy cannot be expected. For particle trajectories at large angles to the applied electric field, neighboring streamers may fail to link, and detection efficiency will be necessarily low. The actual cutoff point depends on the strength and width of the voltage pulse or actually on its closeness to the streamer mode operation. Typically one can count on 100% detection efficiency up to 30° and 0% at about 60°.

The long memory time which enables post-event triggering is, from another point of view, a handicap in high flux operations. Due to their limited mobility, electrons cannot be effectively swept out of the large gap by a clearing field. However, small amounts of electronega-

tive quench gas such as 0.1% CH_4 or 10^{-5}% CCl_4 may reduce the memory time by an order of magnitude to about 1 μsec.[35]

Thus all these limitations are to be expected and tolerated even for the ideal wide-gap spark chamber. The real question lies with how to exploit its good characteristics, how to take the full advantage of its simplicity and high multiple-track efficiency, and how to press for the ultimate precision that its high information density tracks have to offer.

B. PRELIMINARY INVESTIGATIONS

A test chamber with two 127x76x20 cm^3 gaps was constructed to gain a feeling of the spacial and angular resolutions that one might obtain with this type of chamber. Much of the construction was similar to the thin foil chambers which will be described in section C of this chapter.

The experimental arrangement is shown in Fig.31, and schematically illustrated in Fig.32. The two fiducial crosses were in line with the zenith. The two smaller 5.1 cm gap chambers placed above and below the wide-gap chamber were to define a reference trajectory of zenith angle θ_3 and intercept of x_3 with the center electrode. Similar θ_1, x_1 and θ_2, x_2 were to be determined by the upper and lower sparks of the wide-gap chamber respectively. The system was triggered by cosmic ray muon coincidence from two count-

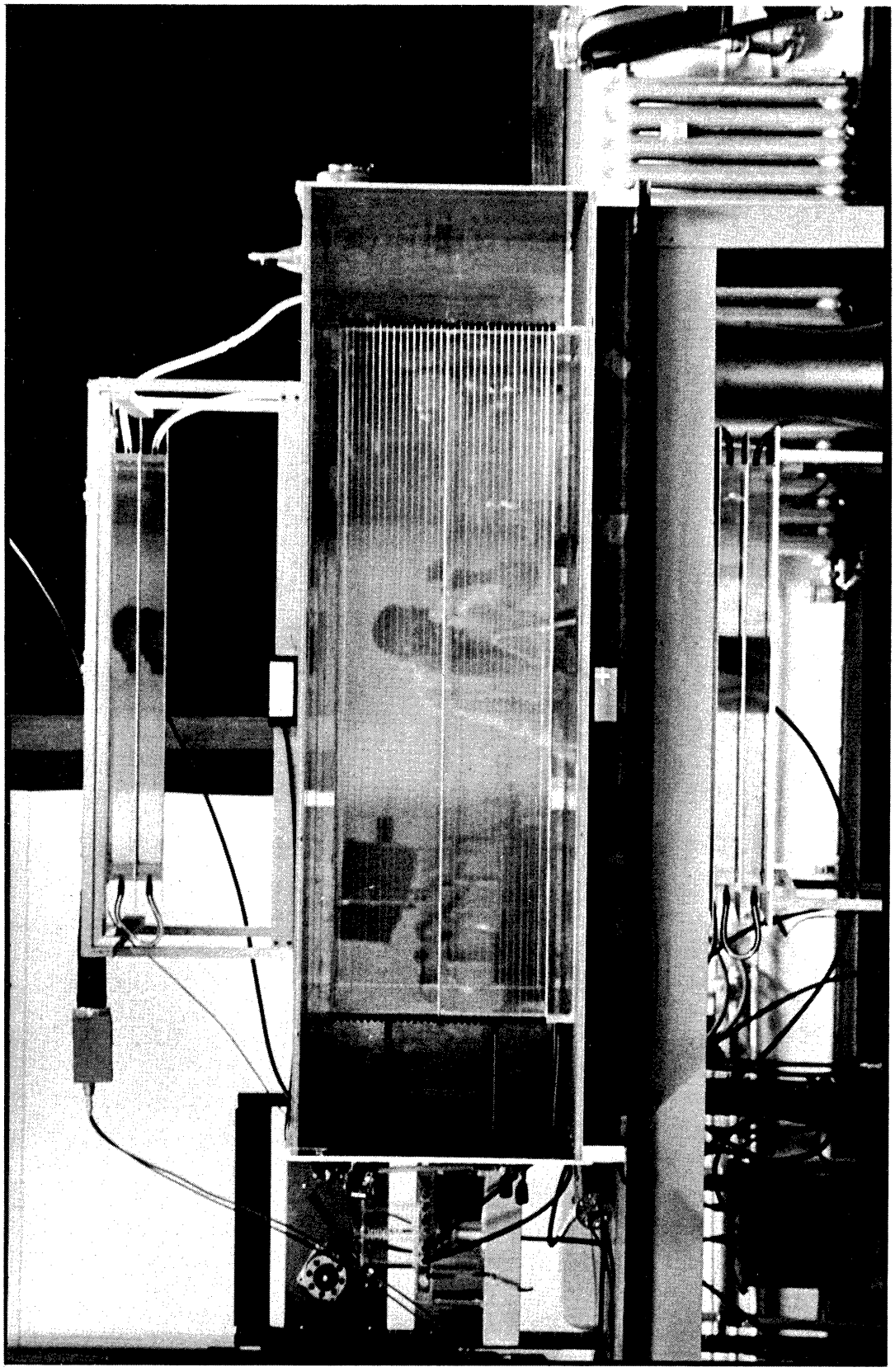

Fig.31 Arrangement for Testing of a Wide-Gap Spark Chamber

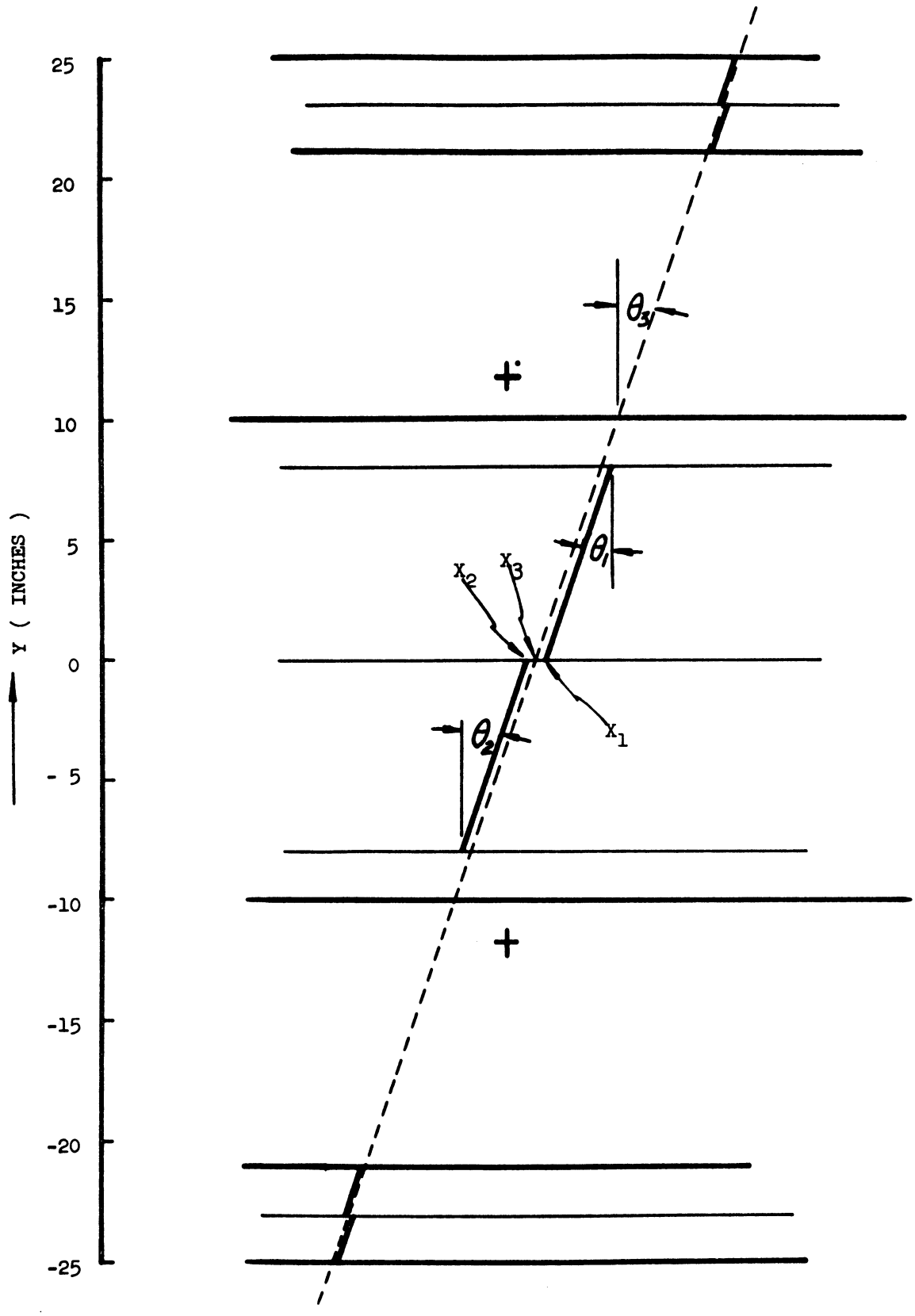

Fig.32 Schematics of Chamber Testing Facilities

ers with 23 cm of lead between them.

Fig.33 shows a typical muon test track . Note that because the wide-gap chamber was pulsed by a Model B Marx Generator which had a positive output, the sparks show a coherent drift of about 5 mm towards the center electrode. The opposite effect is seen in the end chambers which were driven by a -25 kV pulse from a single spark gap.

The test pictures were taken with 30:1 demagnification and were measured on a 3 μm least count film-plane digitizer. The recording density was two digitization points per cm of track length. First order pin-cushion distortion of the lens was corrected through photographing tungsten plumb lines that were electrically heated to glow by means of mercury pool contacts.

The angular and spacial resolutions were measured by

$$\Delta\theta = \theta_3 - \tfrac{1}{2}(\theta_1 + \theta_2)$$

and

$$\Delta x = x_3 - \tfrac{1}{2}(x_1 + x_2)$$

respectively, and their distributions were plotted in Figs. 34 and 35. The rms spread of $\Delta\theta$ was observed to be 0.88 mr while that of Δx was 0.23 mm.

Unfortunately a calorimeter was not available to trigger on very energetic particles and the 23 cm of lead provided essentially a 300 MeV/c muon trigger. The pro-

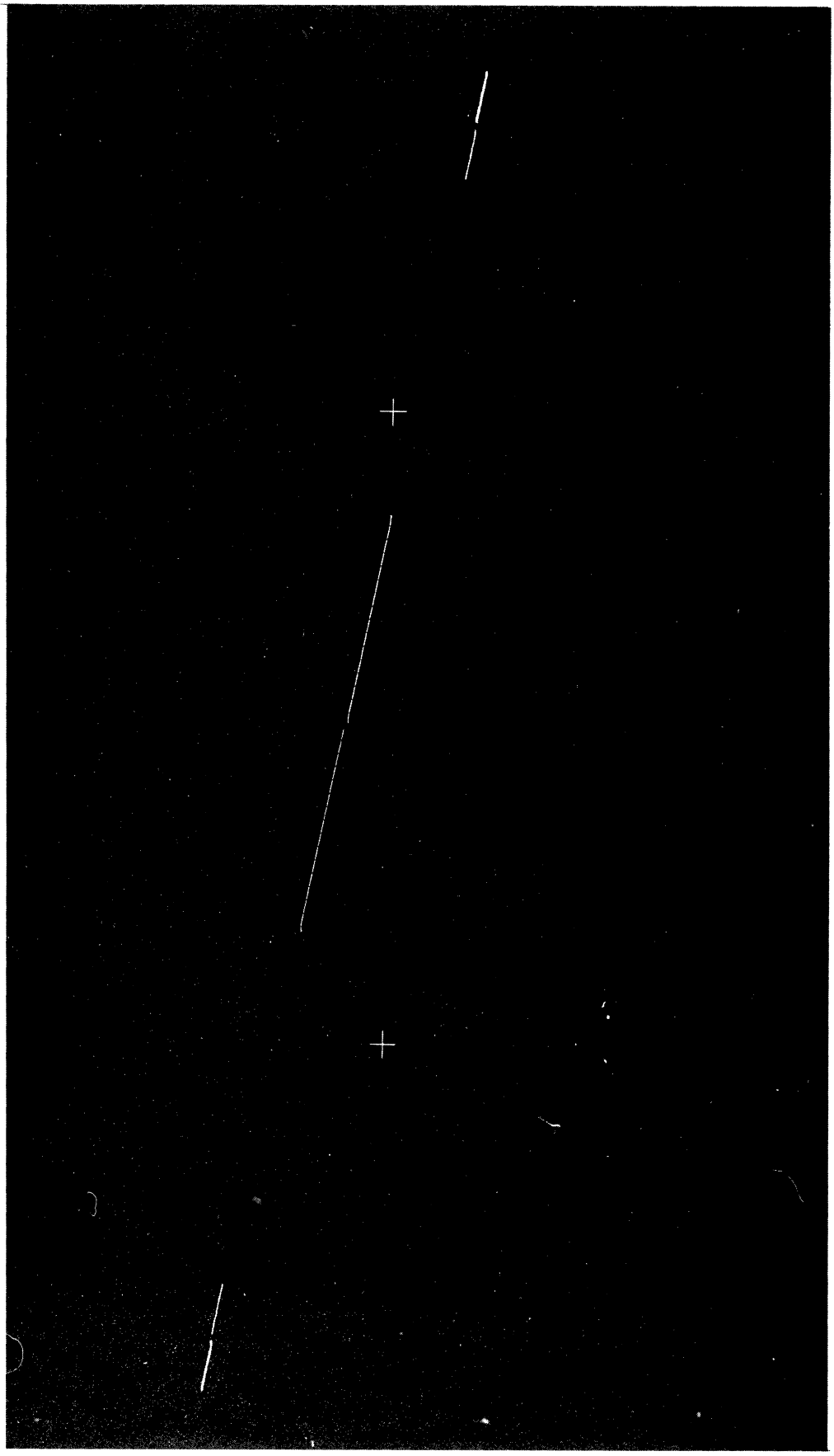

Fig.33 Typical Muon Test Tracks

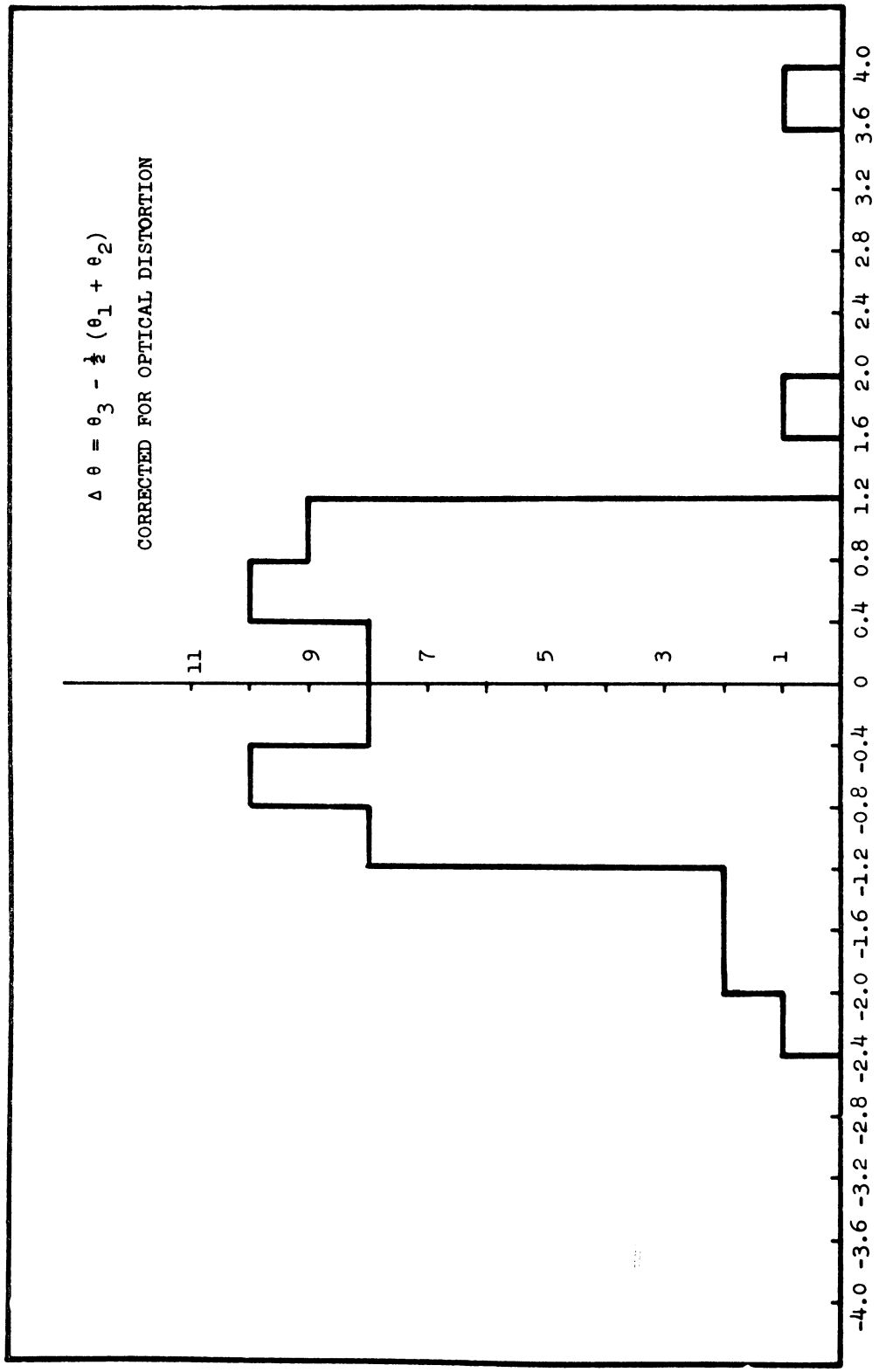

Fig.34 Distribution of Angular Errors in Test Chambers

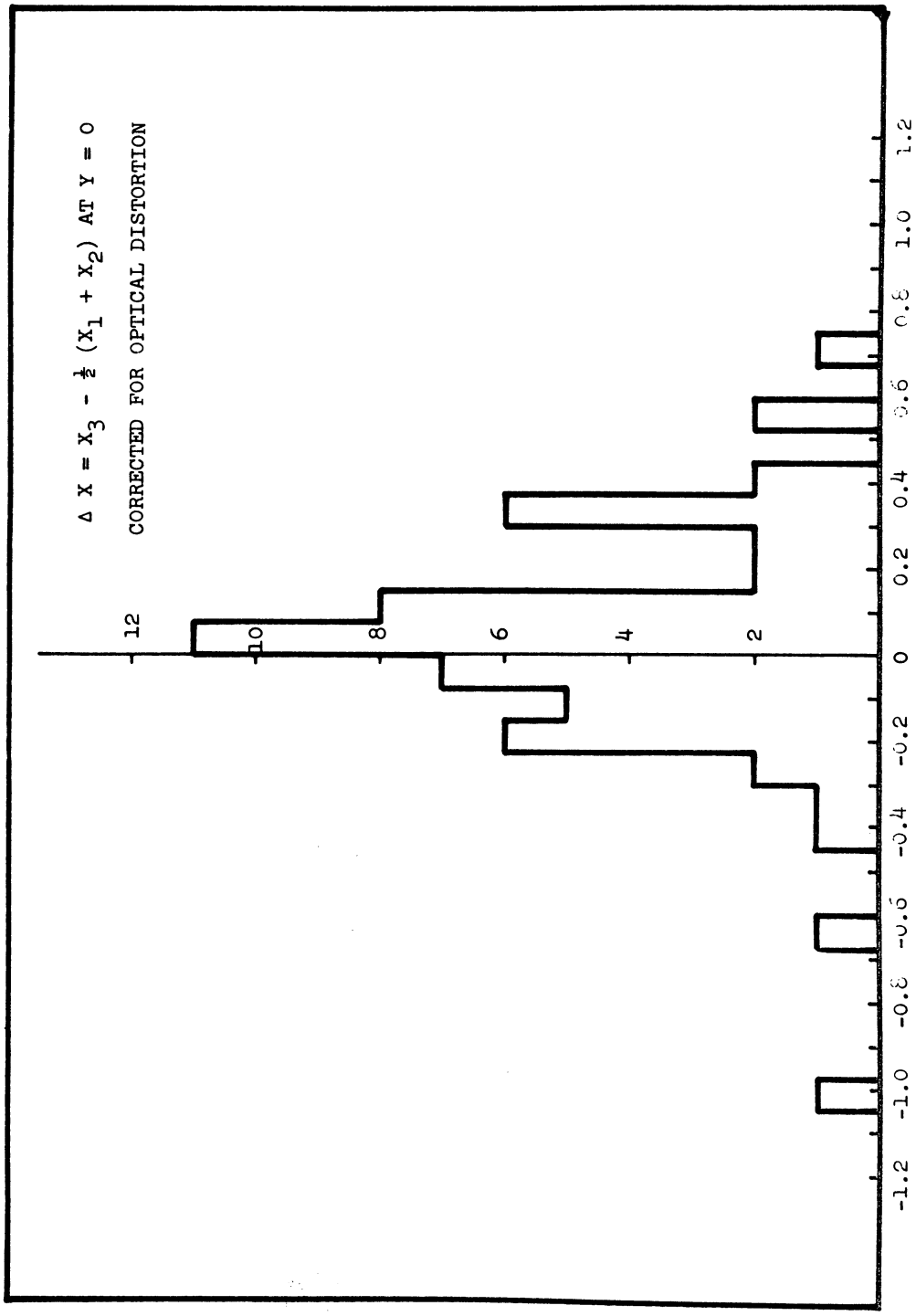

Fig.35 Distribution of Position Errors in Test Chambers

jected rms multiple scattering of such a particle in a 50 μm aluminum electrode is 1.2 mr, and in a .75 mm electrode of the end chamber, it is 4.6 mr. Therefore the observed $\Delta\theta$ and Δx above were completely accountable by multiple scattering. Comparing just the tracks in the wide-gap chamber, the spread of $(\theta_1-\theta_2)_{rms}$ was 0.9 mr. Thus we might conclude that the accuracy of the chamber was surely superior to the observed values.

On the other hand, there was additional information in the variation of the digitized points along the best fitted straight line to a single spark. Fig.36 is a typical example. It shows that the points were randomly distributed with a rms spread ϵ of about 100 μm in real space.

If L is the spark length and N is the total number of uniformly spaced digitizations, the rms angular uncertainty due to the point uncertainty ϵ is

$$\Delta\theta = \left[\frac{\epsilon^2}{L^2} \frac{6N}{(2N^2+1)} \right]^{\frac{1}{2}} .$$

Therefore when $N \gg 1$

$$\Delta\theta \approx \frac{\epsilon}{L} \sqrt{\frac{3}{N}} ,$$

and for the test tracks cited above, (ϵ = 0.1 mm, L = 180 mm, N = 40) the angular resolution for a single spark was 0.15 mr.

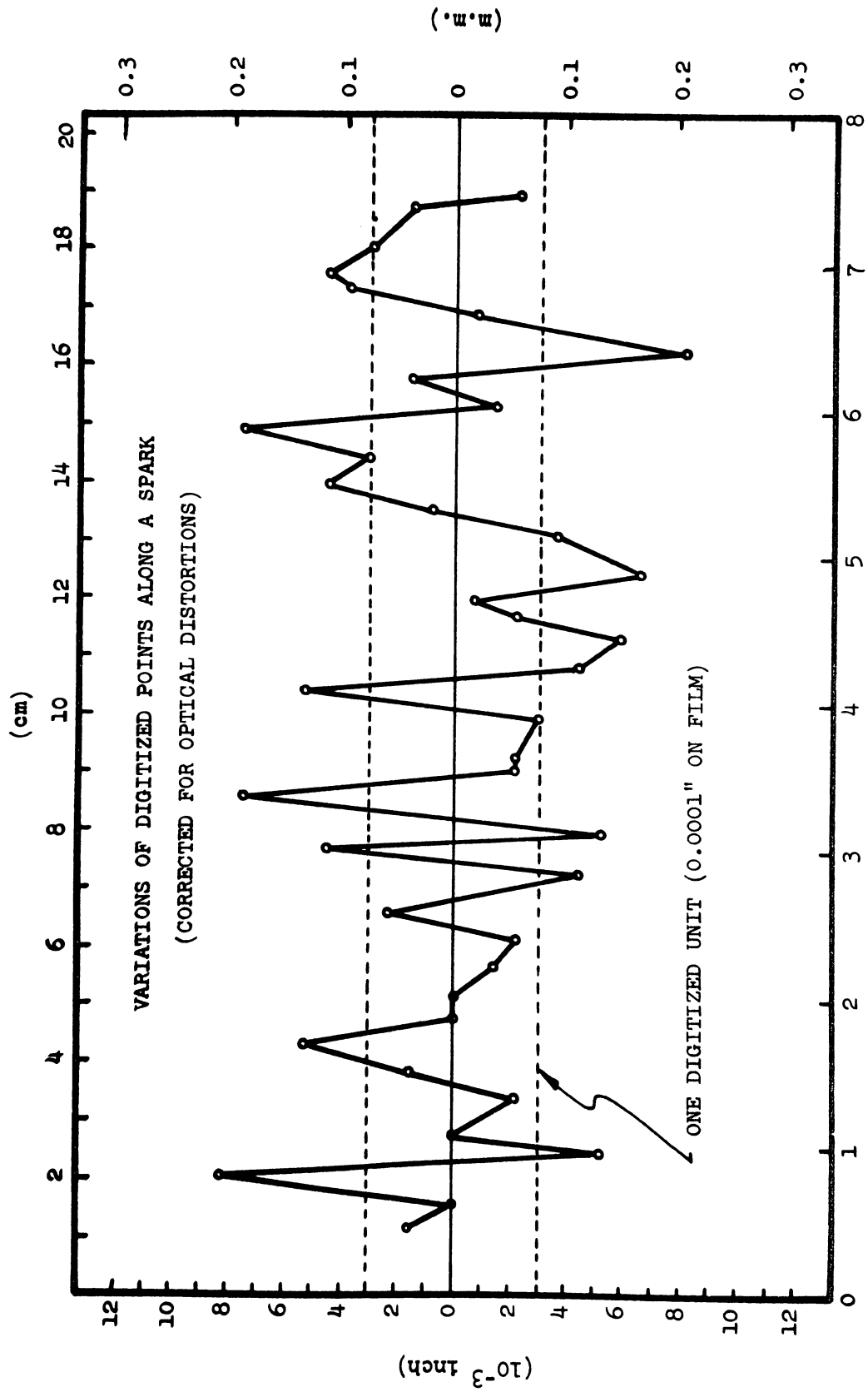

Fig.36 Variations of Digitized Points Along a Spark

Other properties of wide-gap spark chambers are best displayed by the following figures:

Fig.37 is a superposition of eight triggers to illustrate the degree of isotropy for small angle tracks. The apparent curves in the ends of the sparks are reflections from the upper and lower electrodes. The actual amount of deviation from a straight track can be seen near the center electrode. Such deviations are generally contained within one cm from the electrodes, thus a 20 cm gap will have a useful region of about 18 cm.

Fig.38 is a track at 42° with respect to the electric field. It typifies the increased flaring at the ends of larger angle sparks where the formation of plasma channels directly to the electrode is becoming more competitive to the linkage of neighboring streamers.

Fig.39 shows the effect of replacing the center electrode with wires of 1 cm spacing in a small 15 cm gap test chamber. Wire electrodes have significant constructional advantages when considering building chambers of ~ 10 m long. It is seen that much of the track length is wasted by the flaring in the non-uniform electric field. However, when the same chamber was filled by 85-15 nelium with 10% saturated C_2H_5OH vapor, the flaring was drastically reduced as shown in Fig.40. This again illustrates the dominant roll of photo-ionization in the streamer formation process.

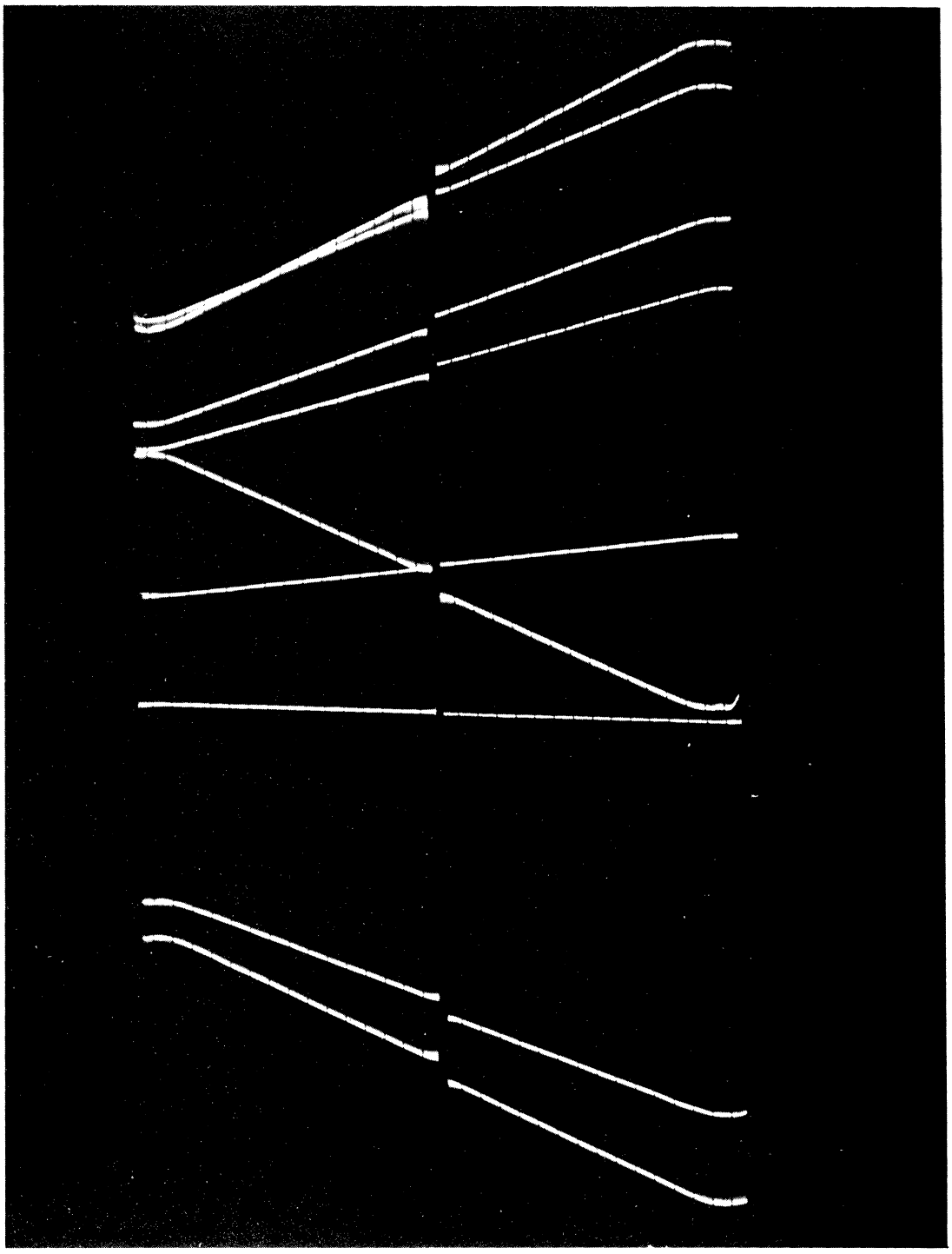

Fig.37 Uniformity of Small Angle Tracks

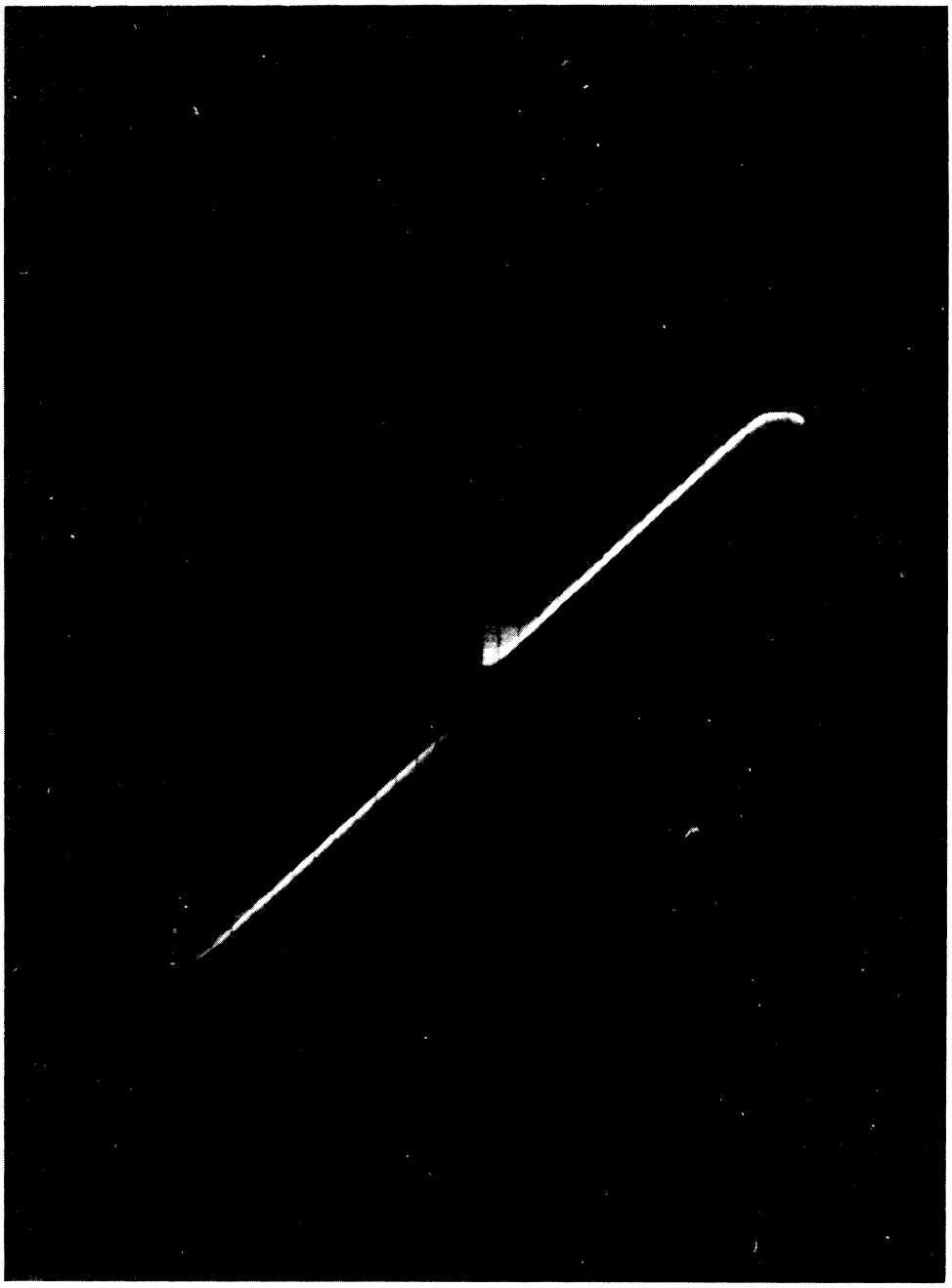

Fig. 38 Appearance of Large Angle Tracks

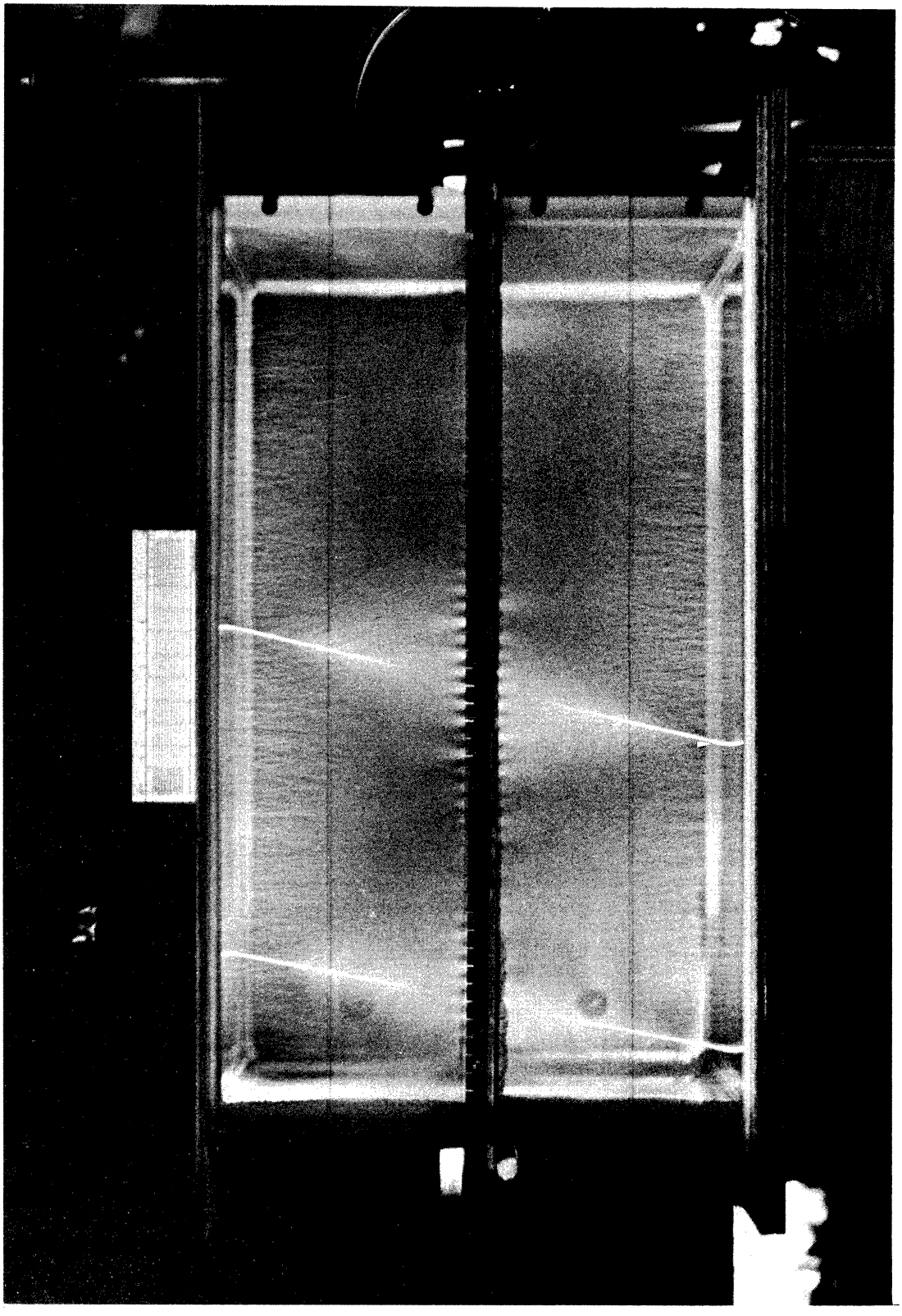

Fig.39 Effects of Wire Electrodes on Discharge

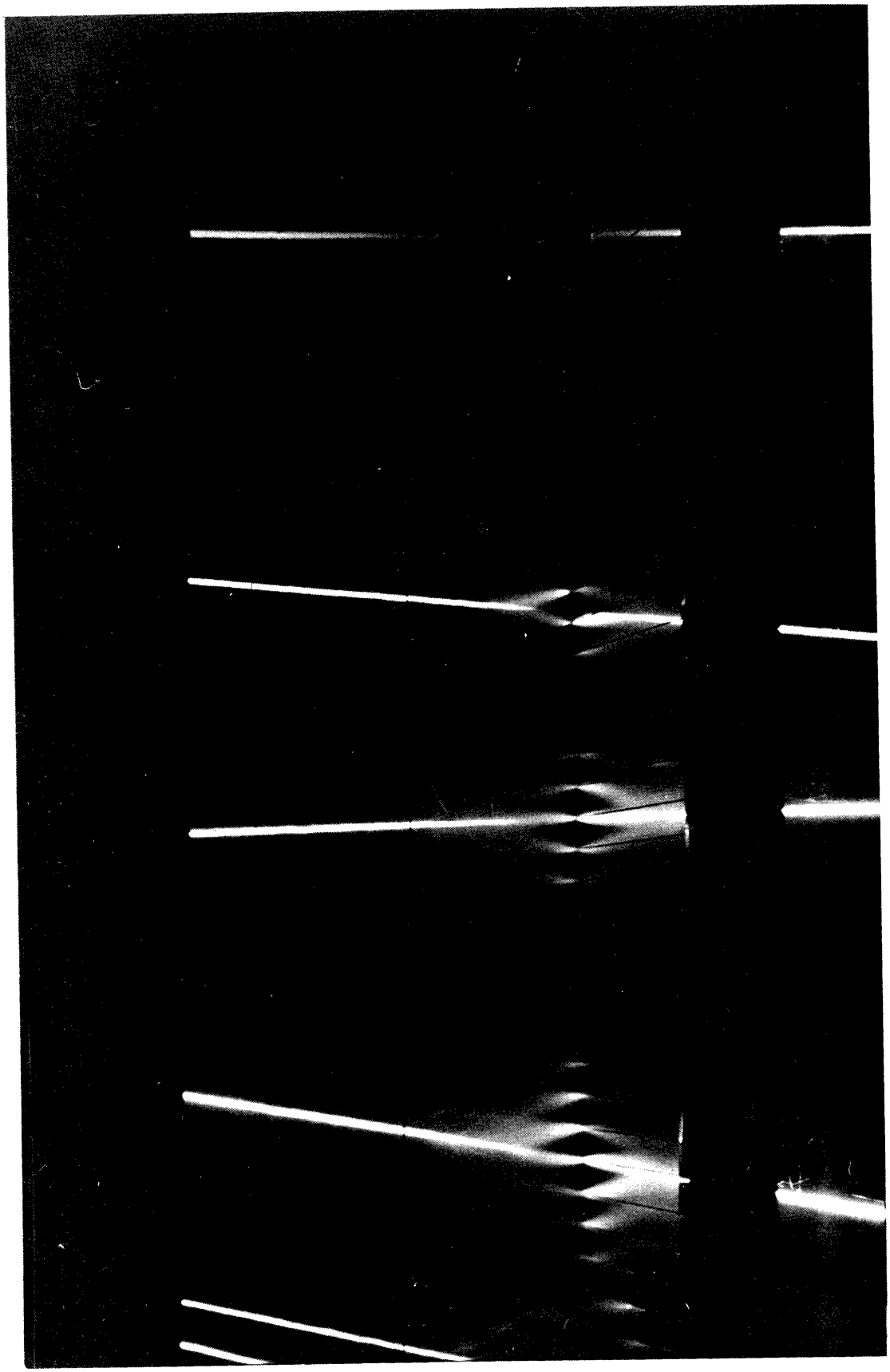

Fig.40 Effects of C_2H_5OH on Spark Discharge

A quick test was also done on the feasibility of placing chamber gas within boxes of dielectrics and inserting them between separate plane electrodes. As it can be seen in Fig.41, extensive distortions were developed, evidently from the transient surface charge distribution on the dielectrics. Such effect was not observed in streamer chambers since little current flow was allowed.

C. THIN FOIL CHAMBERS

Two thin foil wide-gap spark chambers were constructed for the Echo Lake Cosmic Ray Experiment. As shown in Fig.5, they were to detect the incident and emerging particles from the target.

Wide-gap chambers were chosen because of their high multiple-track efficiency, ease of photographic recording and low chamber capacitance. In a cosmic ray background of about one unacompanied particle per 4 m^2 detector area per 250 μsec, the 10 μsec memory time of the chamber was not a handicap. Thin foil electrodes and windows were used so that angular distributions and multiplicities may be studied with a minimum amount of multiple Coulomb scattering and delta ray productions.

Fig.42 is a partial assembly drawing of one of the thin foil chambers. The chamber walls were made of 1.26 cm plate glass for good optical quality and minimum

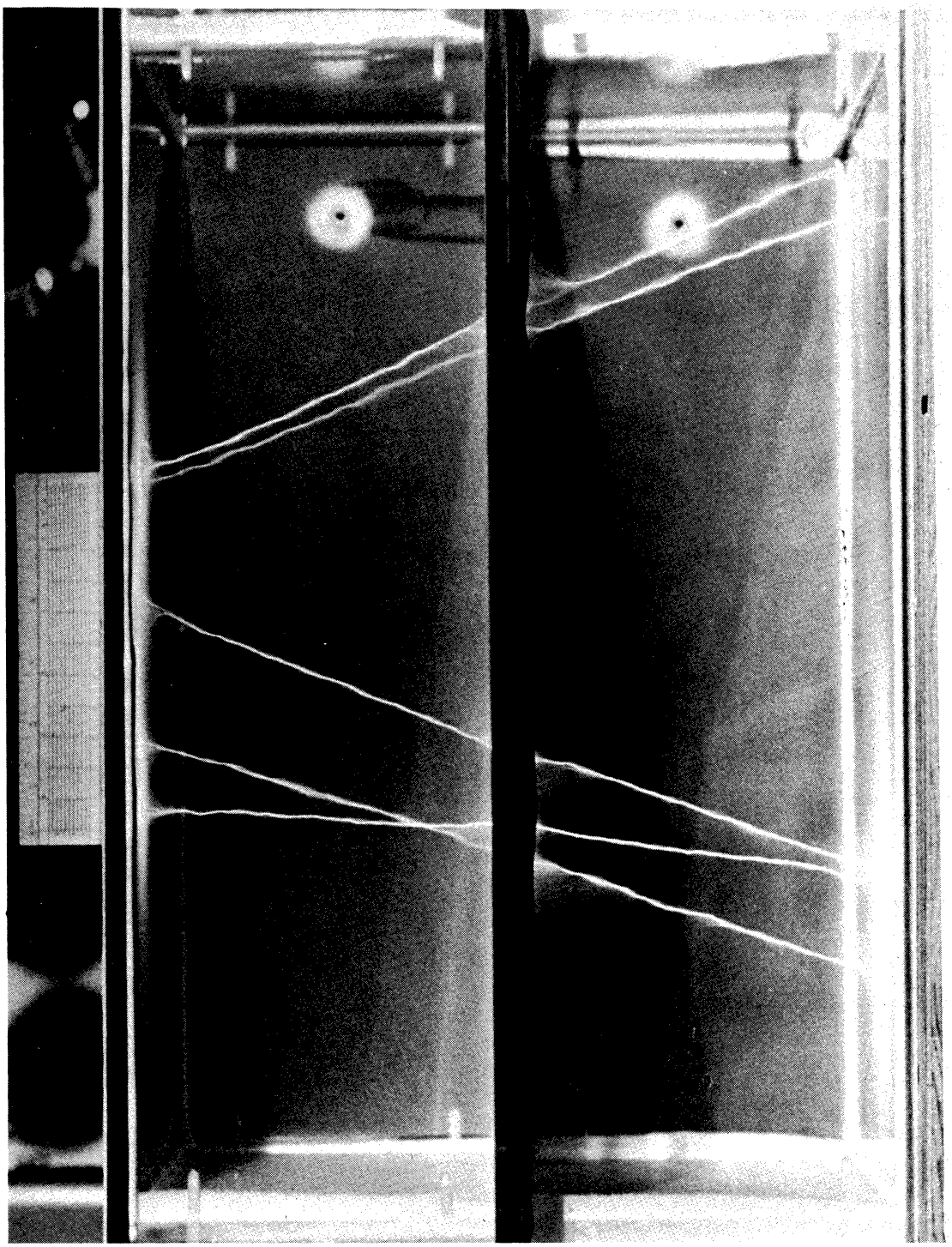

Fig.41 Effects of Dielectric Layers on Discharge

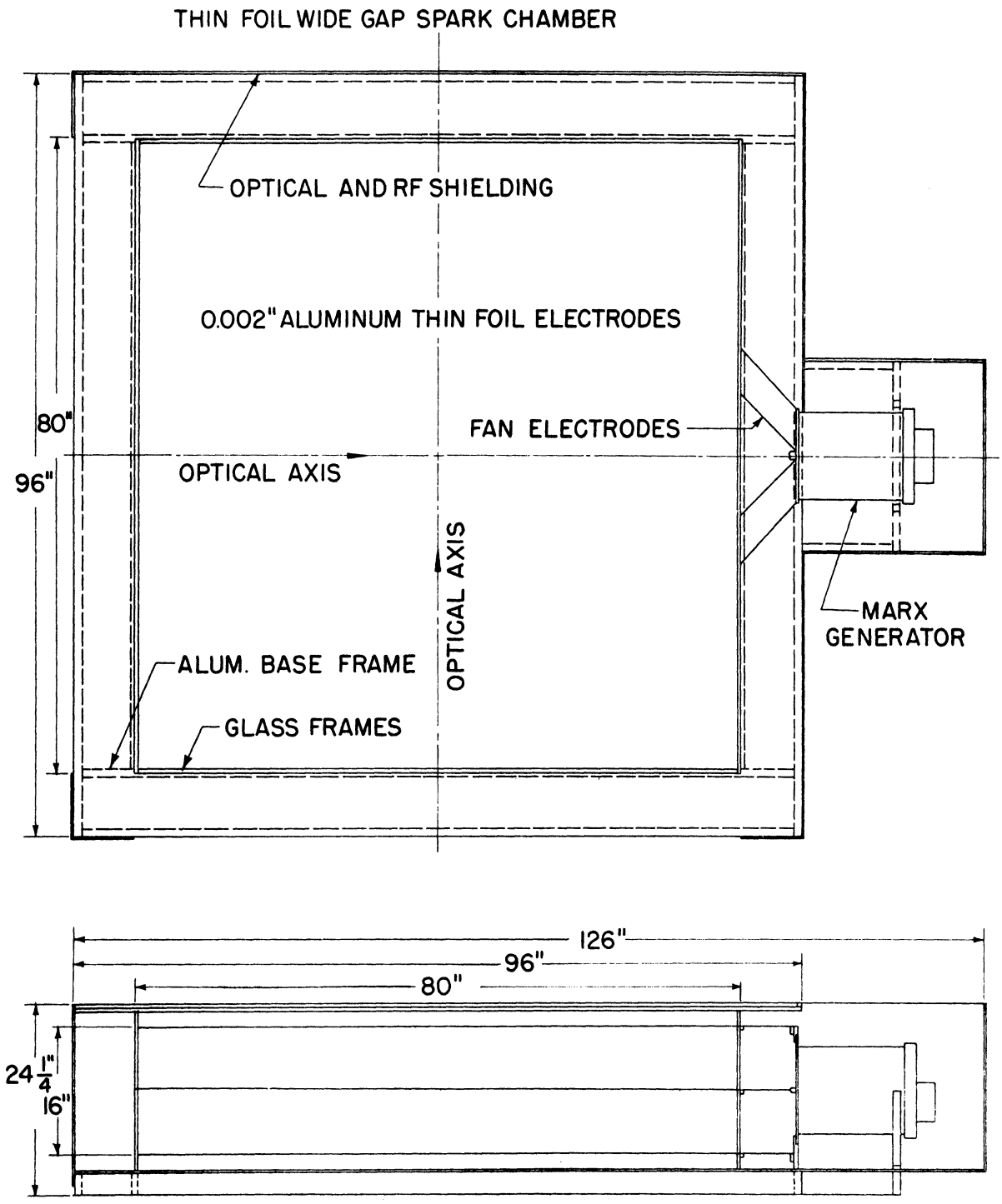

Fig. 42 Partial Assembly Drawing of a Thin Foil Chamber

out-gassing. There were two 20.5 cm active gaps and two outer 5.1 cm dummy gaps whose functions were to shield the RF radiation and to insure that active electrode positions were unaffected by ambient pressure changes.

The electrodes were 50 μm hardened aluminum foils. Each piece was spliced from two sheets in the middle with 25 μm mylar tapes. It was slightly but uniformly stretched over a flat surface, then cemented to a 2x2 m^2 glass frame with Dow Corning 891 RTV to form a section of the chamber. There was also a peripheral layer of 0.25 mm thick by 12.7 cm wide mylar tape between each foil and glass, to prevent surface breakdowns which might result from dielectric discontinuities and minor surface flaws. Wires were stretched over the external surface at 1.27 cm intervals and interconnected by 1.5 kΩ 2W resistors at all four corners to reduce the non-uniform fringe fields. With the chamber capacitance at 360 pf, this arrangement produced a 1.1 μsec decay constant as well.

Pairs of fiducial crosses 1 mm wide by 2.5 cm long and 162.56 cm apart were sand blasted onto the glass frames such that one pair would be on the front and back planes in each view of each chamber. These crosses were only lit for calibration purposes. During a normal run, four external fiducials designed for automatic scanning were used in each view. The inner surfaces of the glass frames at the far sides of the cameras were sand blasted

to eliminate reflections.

Fig.43 shows one of the two large volume thin foil chambers which was assembled and tested at the University of Michigan. It was then completely disassembled for shipment to Echo Lake, Colorado. The thin foil window which faced the target had a 125 μm thick protective mylar lining, and its strength was being tested while disassembling as shown in Fig.44.

The static pressure in the chamber was monitored by a Mercoid Type PQ sensor which would actuate a solenoid valve to let in gas from the supply bottle whenever the chamber gauge pressure dropped below 0.2 torr. A safety bubbler set at 0.4 torr would bleed off any excess pressure. The gas was also slowly recirculated at about one chamber volume per day through a purifier which consisted of a cartridge of type 13X Linde Molecular Sieves followed by a cartridge of calcium chips maintained at about 350° C. The former removed all molecules with large electric dipole moments electrostatically while the latter removed oxygen and some nitrogen chemically.

Each chamber was driven by a Model B Marx generator at typically 14 kV per stage, and had been continuously operational for four years. Photography was done by two 90° stereo cameras (Flight Research Model 207) at f:8 and a demagnification of 65:1. Each light ray would encounter two mirror reflections before reaching the camera

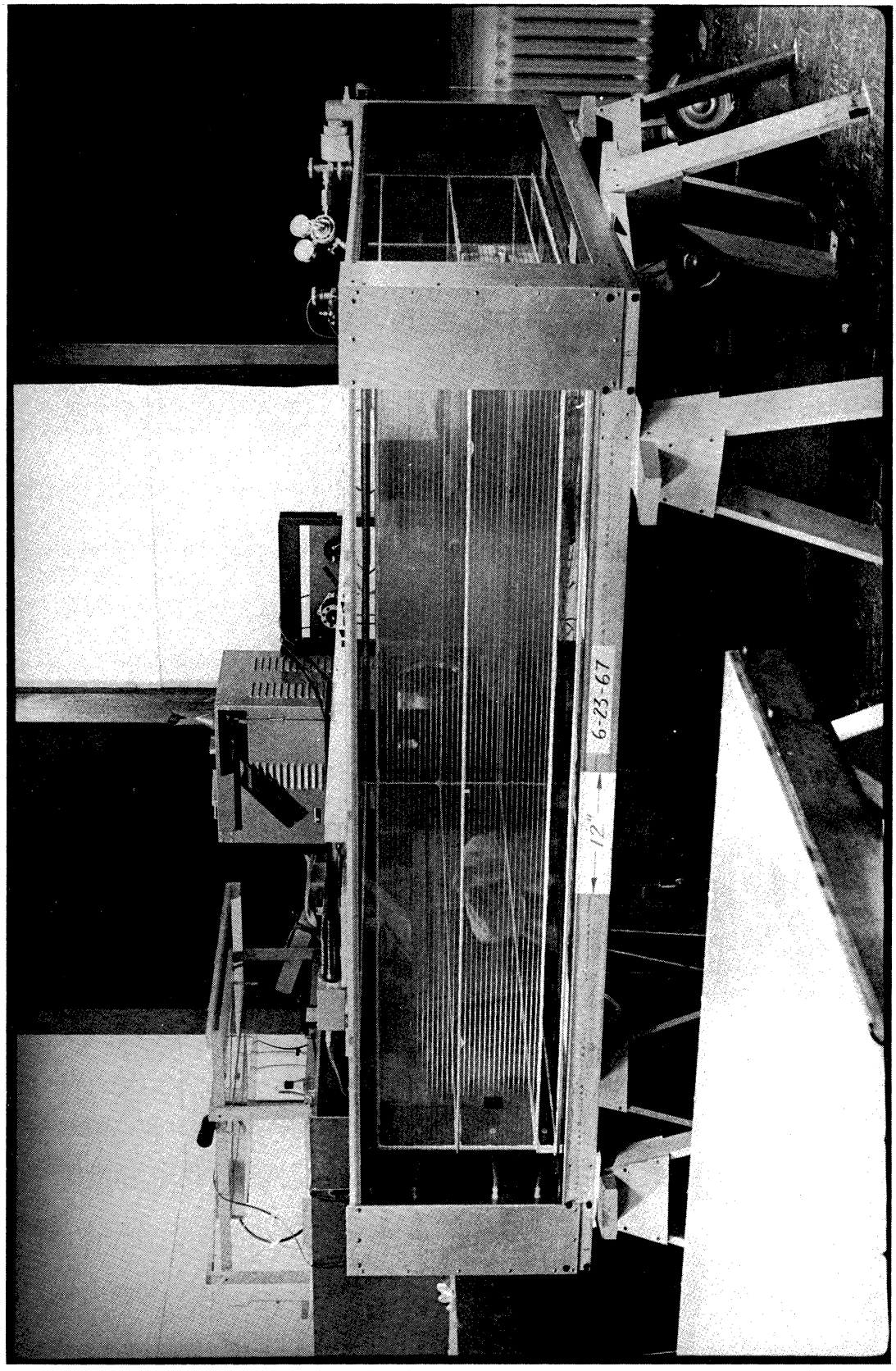

Fig.43 A 2x2 m^2 Thin Foil Wide-Gap Spark Chamber

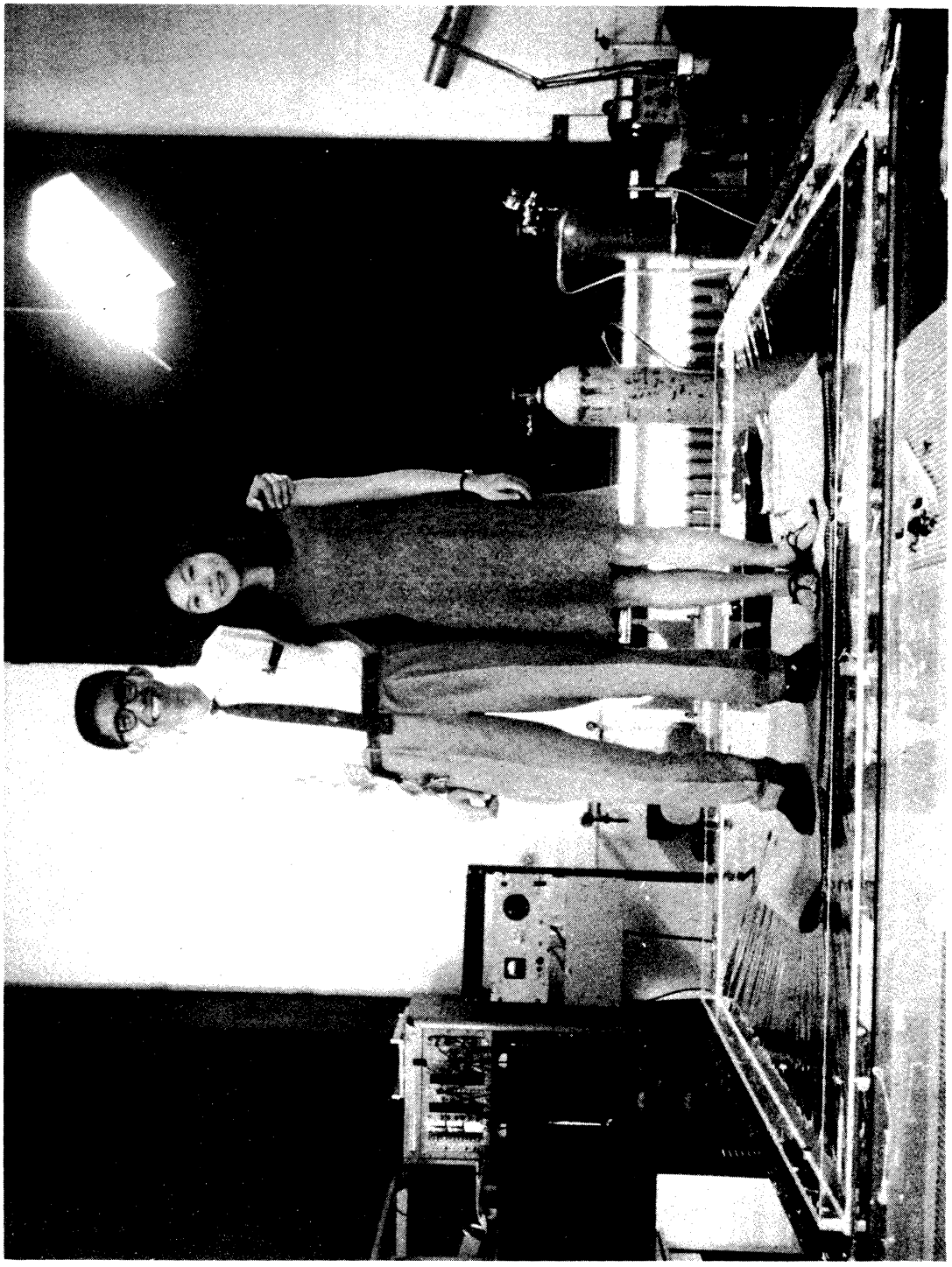

Fig.44 Strength of the Thin Foil Window

such that all spark chamber information was folded into a single 35 mm film format. The rather low f-stop used was to ensure that all secondaries emerging from the target would be recorded.

The single gap detection efficiency was defined as the ratio of the number of tracks resolved in the gap to the maximum number of tracks resolved in any view of any gap. This efficiency was observed to be 96% for large multiplicity tracks with angles of less than 35°. The missing tracks were partly due to some local intensity differences between the two gaps and partly due to shadowing effects among the tracks themselves. Thus the combined detection efficiency for both gaps was virtually 100% and rather independent of multiplicity.

The smallest angle observed between two very close tracks near a vertex was 2 mr. This means their separation at the far ends was about 0.8 mm. Considering the mechanism of spark formation, two tracks are expected to be resolvable as soon as their lateral spacing is comparable with the reciprocal of the ion density along the tracks. For neon at two thirds of an atmosphere, this is about 1.0 mm.

The angular resolution determined through comparisons of tracks in the two chambers was 2 mr. This was quite adequate for all the data analysis that were intended excepting elastic scattering measurements. But it fell far

short of the intrinsic resolution of such chambers.

One of the major sources of error was the lack of sufficient number of fiducial marks and the knowledge of the precise locations of the existing marks, whose positions in real space were not known to better than 0.5 mm. Another complication was the compound distortions in the mirrors; even with the aid of a fiducial grid, it was not possible to untangle all the distortions down to 0.1 mm. A third possibility was the distortion of sparks in a non-uniform electric field. Each electrode had the same maximum sag of about 1.3 cm at the center; but some small unmatched ripples of about one mm were present over surface lengths of several centimeters. The fringe field correction by voltage dividing wire planes was perhaps only partially effective.

D. HIGH PRECISION MULTI-WIDE-GAP SPARK CHAMBERS

(1) DESIGN PRINCIPLES

Unlike many other processes, the momentum analysis by magnetic deflection is a direct and absolute measurement.

The most accurate determination, as it was pointed out in chapter I, is to have detectors placed before and after a deflection magnet. At relativistic energies, the momentum p in GeV/c of a singly charged particle is

$$p = \frac{300}{\theta} \int B_{\perp} \, dl \quad ,$$

where θ, the deflection angle, is in mr and the magnetic field integral is in Tesla-meters. Therefore, for a given magnet, the momentum resolution is equal to the angular resolution.

A 1.3 Tesla-meter superconducting magnet which was originally designed for a balloon-borne cosmic ray experiment was on loan from Alvarez et al. to the Echo Lake Experiment. Two spark chambers of four 20.5 cm gaps each were designed to match the magnet. The incorporation of this spectrometer to the original Echo Lake Experiment is illustrated in Fig.45.

The sole purpose of the chambers is to measure as accurately as possible the deflection angle θ. An angular resolution $\Delta\theta$ of 0.1 mr will correspond to a maximum detectable momentum M.D.M. of 3.9 TeV/c.

The chambers were designed for making direct angular measurements rather than deducing angles from spacial determinations for several reasons:

First, long leverage arms cannot be utilized in order to maintain a sufficiently large admittance of the apparatus. Second, the zenith or the level provides the most convenient common reference; thus no complicated chamber to chamber and view to view correlations are necessary for angular measurements. Third, angular errors due to non-

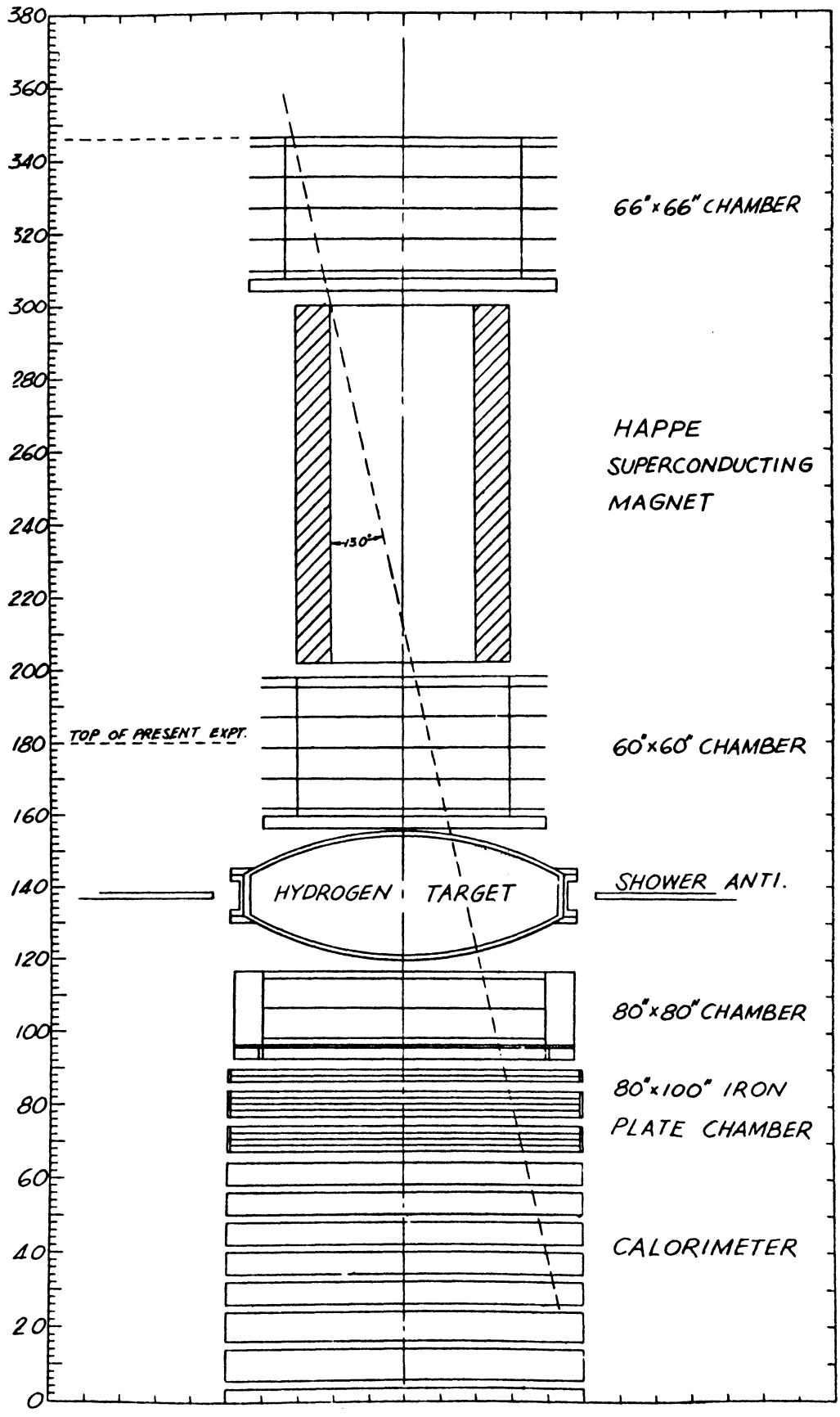

Fig.45 The Modified Echo Lake Cosmic Ray Experiment

uniform fringe field tend to cancel in mirror image gaps but position errors do not. Last but most significantly, lateral mechanical stability of the apparatus is far worse than rotational or level stability. Besides, the latter can be easily monitored throughout the experiment.

Having decided on the type and modes of operation of the chamber, the remaining question was how to assure that sparks would faithfully reproduce the particle's angle in the critical view parallel to the magnetic field lines. The deciding factors are summarized as follows:

(a) Electron Diffusion: Prior to the arrival of the voltage pulse, the electrons diffuse away from the original column. This one dimensional projected rms spread Δr is given by

$$\Delta r = \sqrt{2Dt} \quad ,$$

where D is the diffusion constant and

t is the diffusion period or voltage delay-time.

It is a priori that delaytime should be kept to a minimum.

(b) Electric Field: An ion column will drift a few mm along the electric field before a spark channel is formed. If the field lines are not parallel along all portions of a track, a rotation of the spark will result. Assuming the drift of a track is 5 mm, then the directional field uniformity must be better than 0.4% along

the track for a rotation to be less than 0.1 mr. The maximum zenith angle of a track within the fiducial volume of the apparatus is 13° corresponding to a lateral displacement of 6.6 cm in a 20 cm gap. If this displacement is allowed to subtend an angle of 4 mr with the center of curvature of the electrode, then the maximum allowable sag in the electrode of a 168 cm span will be 2.14 cm. Similarly, surface bumps of 1 mm high should not have a wavelength of less than 36 cm. In practice, electrodes with maximum sags of less than 1 mm and surface waves of less than 0.5 mm over distances longer than 30 cm have been achieved. On the other hand small bumps over distances much smaller than the gap spacing will not have much effect. Due to geometrical constraints the zenith angle distribution of the actual flux is rather vertically peaked, and the probability of a large angle track passing through consecutive bumpy regions in all the gaps is small indeed.

A fluid mapping was done to study the fringe fields between thick electrodes and near by shieldings. A careful tracing with a digital voltmeter could chart the field lines to ±0.2% accuracy. No observable field non-uniformity was found at regions over one gap width inside from the edges. One of the reasons for choosing four 20 cm gaps instead of two 40 cm gaps was

to maintain a large useful fraction of the chamber volume. The use of 25 cm overhangs for 20 cm gaps was a simple and effective solution to the fringe field problem.

(c) Magnetic Field: The trajectory of an electron in vacuum under a cross field of E (along +z axis) and B (along -y axis) is

$$x = \frac{a}{\omega^2} \left(\omega t - \sin \omega t \right)$$

$$z = \frac{a}{\omega^2} \left(1 - \cos \omega t \right) \quad ,$$

where $a = \frac{eE}{m}$ and $\omega = \frac{eB}{mc}$.

In a noble gas medium and under the condition of strong electric field E and weak magnetic field B, the cycloidal radius $\frac{a}{\omega^2}$ will be much larger than the electron mean free path λ, and motion may be approximated by successive small angle scatterings nearly along the electric field. The resultant angle is then

$$\frac{\Delta x}{\Delta z} \approx \frac{\lambda}{a/\omega^2} \quad \text{or}$$

$$\Delta x = \frac{\Delta z \lambda e}{mc^2} \cdot \frac{B^2}{E} \quad .$$

Taking the column drift as $\Delta z = 5$ mm, $\lambda = 2.17$ μm in neon at 500 torr and E = 5 kV/cm, the lateral displacement will be 0.38 μm at B = 100 gauss or 38 μm at B =

1,000 gauss. The highest stray field in the nearest gap to the Echo Lake magnet is about 350 gauss and the effect is completely negligible. Again, it is seen that angular measurements, which are sensitive only to the gradient of magnetic field, is inherently less vulnerable than position determinations.

(d) Information Density: The ultimate limitation on the amount of information a spark has to offer is the primary ion density along the track. Since to increase this density by pressurization is not feasible for large volume chambers, some improvement may be gained by taking advantage of the gas properties.

Among the common noble gases used for spark chambers, argon will give the highest ion density but the threshold voltages for forming a spark in a 20 cm gap in He, Ne and Ar are 55, 100 and over 250 kV respectively. Thus Ne is generally chosen as the fill gas.

The ionization potentials of noble gases are large but the excitation levels are also quite high. Many atoms will be in the excited state from soft collisions with the ionizing particle, thus only a small amount of energy is required to ionize them. The energy locked up in a metastable state will not be available for further ionization except when there are inpurity atoms present whose ionization potential is close to and below that level. This increase in ion-

ization from impurities is known as the Penning effect. It is seen from Table 2 that argon will be a suitable impurity to produce this effect in neon. A parctical amount to use is about 0.5%.

(e) Multiple Scattering: The amount of multiple scattering is a constant fraction of magnetic deflection since they have the same momentum dependence. This fraction is 1.7% in the entire spectrometer of the Echo Lake Experiment.

(f) Optics: Worse results usually arise from compounding errors; thus optics must be kept as simple as possible. This means direct photography without mirrors is essential. In making measurements, it means the use of film-plane digitizers without inherent non-linearities.

High quality glass is needed for chamber wall construction. The radius of curvature of good plate glass is typically 0.5 km. The error from such a gross bending of a 1.27 cm glass is less than 1 μm hence completely negligible. More serious is any local lens effects. A local flatness of 2 fringes per 2.45 cm (5893 Å light source) will lead to an average error of 20 μm at 85 cm behind the glass if known fiducial marks are spaced 10 cm apart on the glass.

(g) Fiducial Marks: We have learned from the mistakes of the thin foil chambers that positions of reference

marks must be known as precisely as possible. There should be a sufficiently dense map of marks on the front glass of the chamber to correct lens distortions and similarly on the back glass to correct errors introduced by the front glass.

(2) CHAMBER CONSTRUCTION

Fig.46 shows the details of the multi-wide-gap chamber. The special electrodes made by the Met-L-Wood Corporation had a 1.27 cm thick balsa wood core and 0.625 mm aluminum skins. The combination was designed for high strength to weight ratio. The maximum sag at the middle of the plate was less than 1 mm when supported on a 168x168 cm^2 glass frame with 25 cm overhangs. Square aluminum rods were imbedded beneath the glass to carry the compressive load, and on the perimeters for smooth edges. Surfaces not parallel to the optical axes were scrubbled to reduce reflections, although it was not most effective at such small angles. On the other hand reflections from the back surfaces of the chamber were eliminated by tacking 1.6 mm sand blasted black plexiglas sheets to the glass. Holes were cut to uncover the back fiducial marks.

The glass plates were made by a twin ground process for good parallelism on the surfaces. The quality control figure for local distortion indicated a standard deviation of 2 fringes per radial 2.54 cm or a radius of

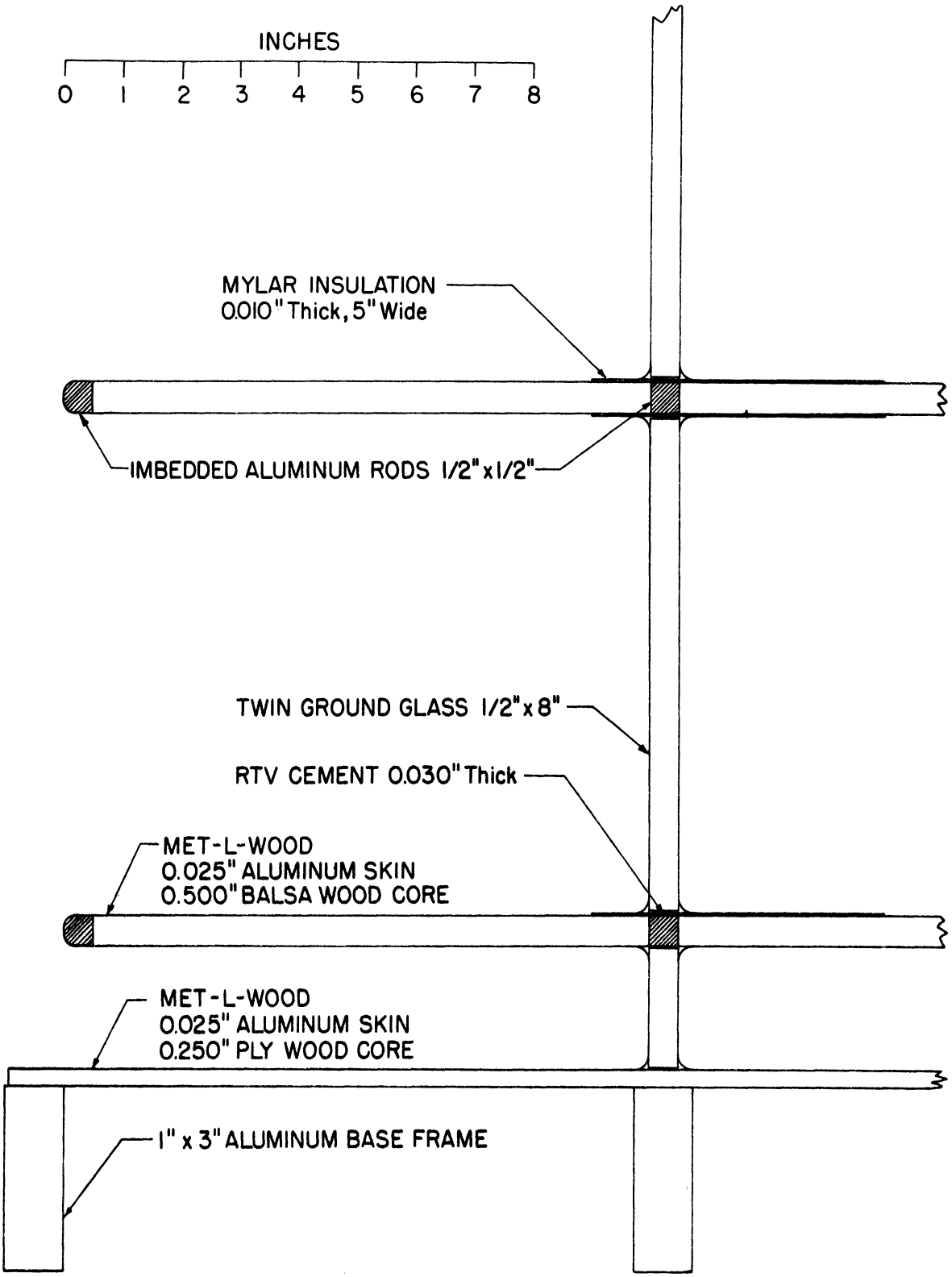

Fig.46 Construction Details of Multi-Wide-Gap Spark Chamber

curvature of 547 m. The long edges of each plate were ground to be parallel to within 0.25 mm, while the short edges were polished to facilitate edge illuminations of the fiducial marks. 1.0 cm holes were drilled for gas connections. Fig.47 shows the chamber glass plates before assemblying.

Fig.48 shows the base frame of the smaller chamber constructed out of selected aluminum bars with minimum twists. It was supported on four fine leveling screws. The level of the chamber could be checked by using a special 2.44 m long leveling bar across the four corner pads on the base frame. The idea was to assemble the chamber on a perfectly leveled frame such that after transportation, it could be releveled on the experimental stack to relieve mechanical strains. The chamber could be consistantly leveled to $\pm$ 12 μr; this formed the basis for angular correlations.

The layer by layer construction of the chamber is illustrated in Fig.49. With the aid of a 2.4 m vernier calipers and a sensitive level, the glass plates were held by jigs while they were cemented with Dow Corning 891 Silastic RTV. The vertical tip of the frames were held to be under a fraction of a mr. Small 1 mm thick spacers were placed under the glass to assure a minimum glue thickness for secure bonding. The anti-reflection sheets were tacked to the back surface with minimum optical contact areas so

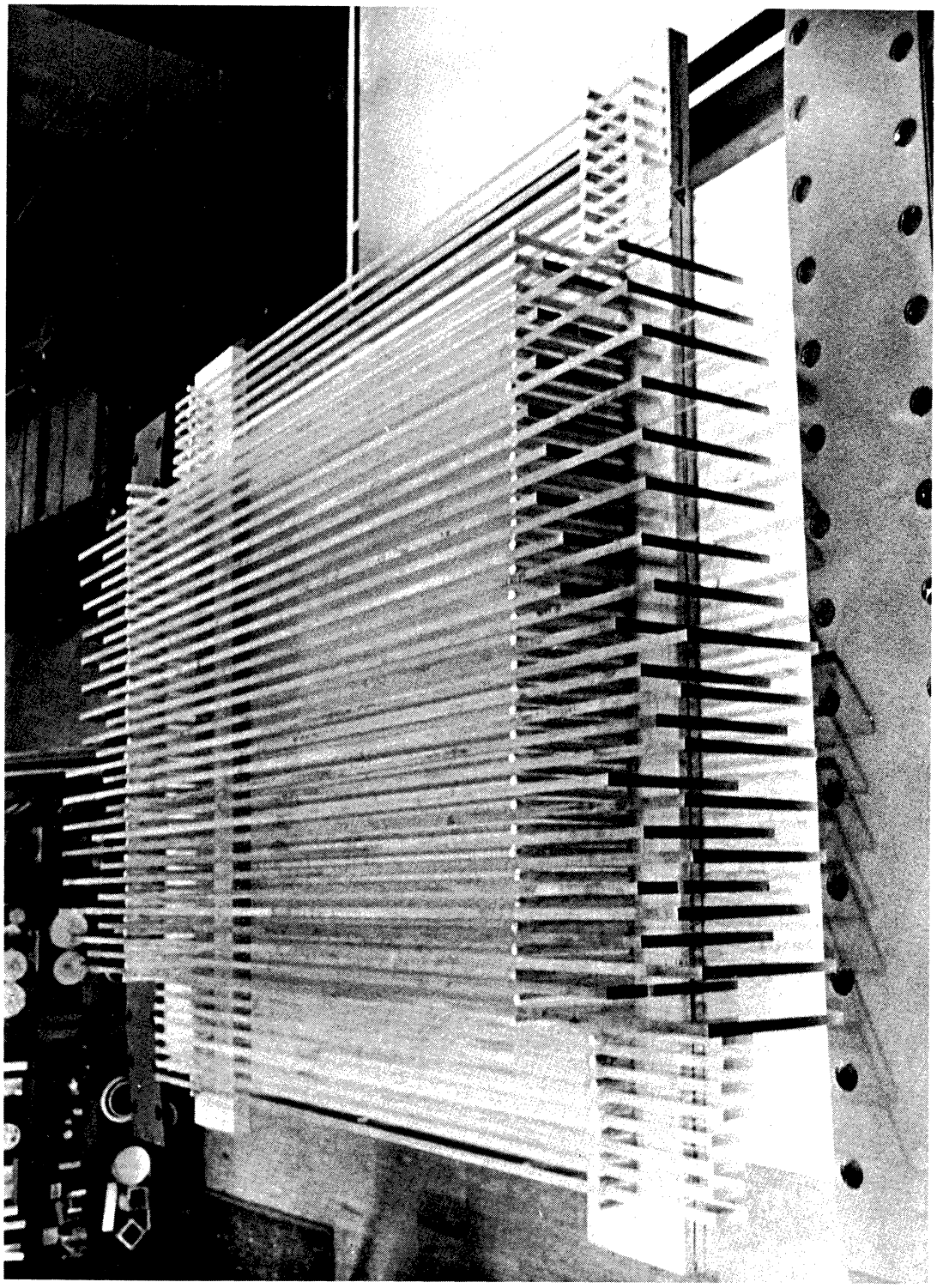

Fig.47 Chamber Glass Plates Before Assembling

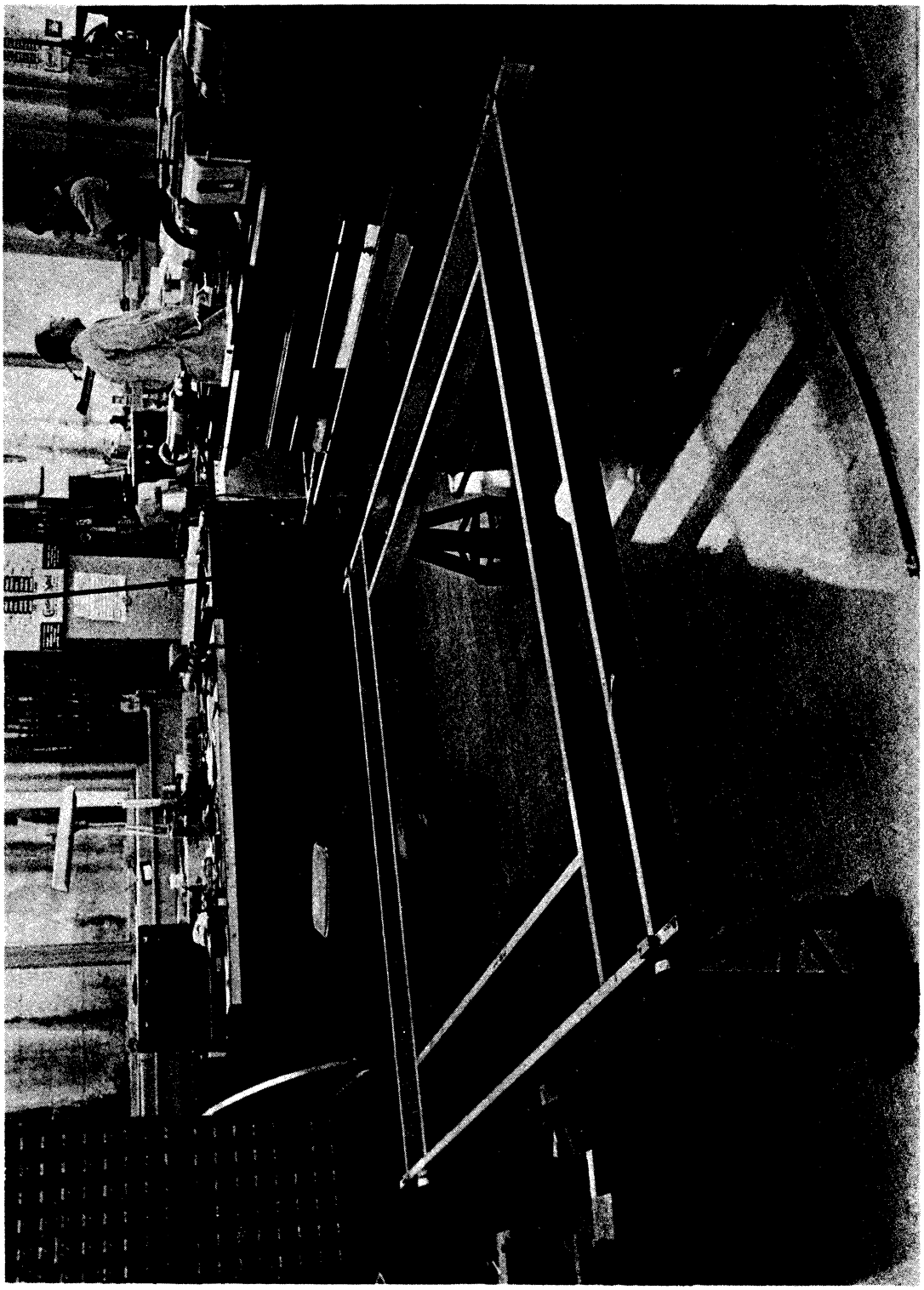

Fig.48 Base Frame of Multi-Wide-Gap Spark Chamber

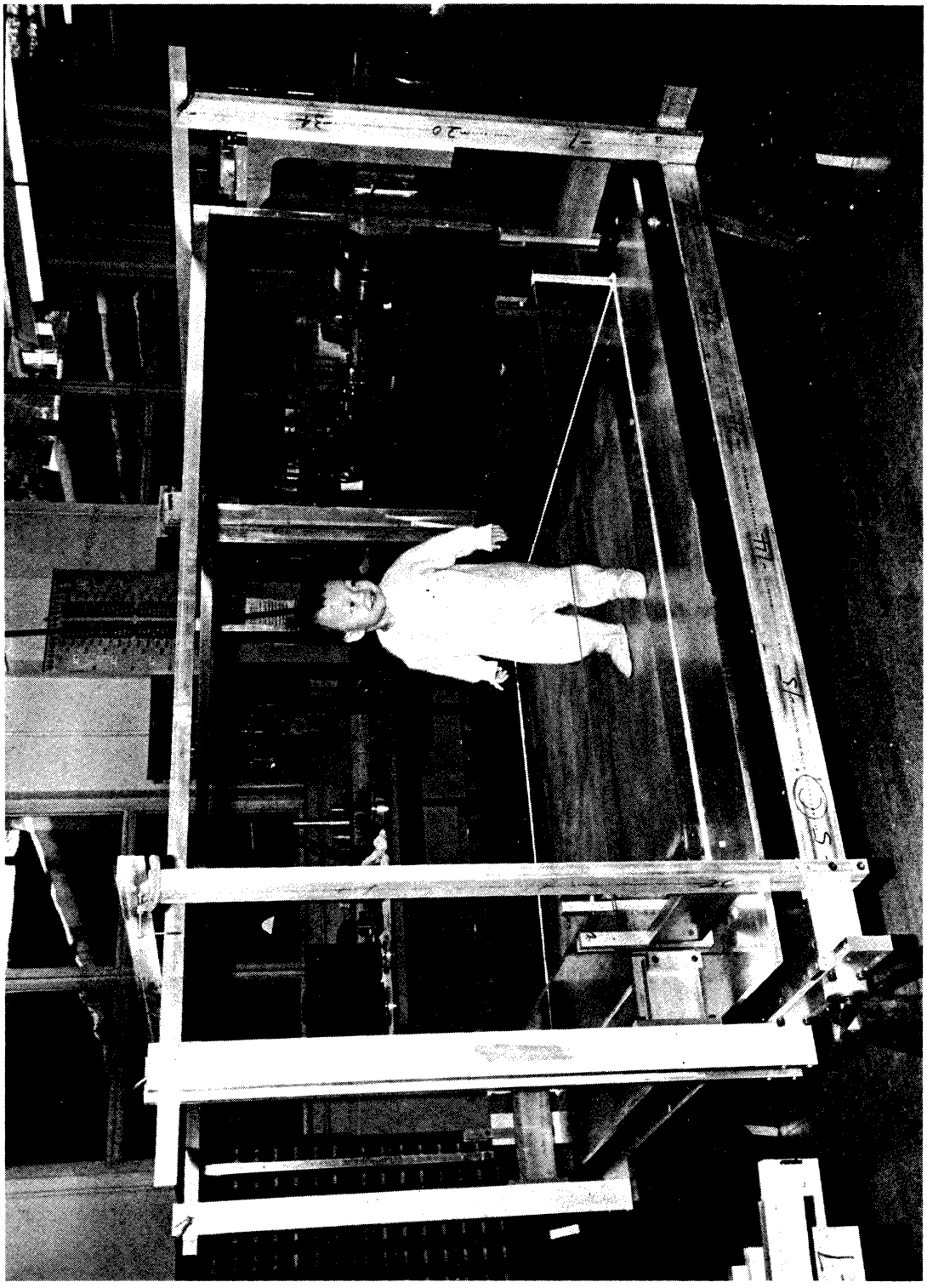

Fig.49 Assembly Procedures of Multi-Wide-Gap Spark Chamber

as not to interfere with the lighting of the fiducial marks by total internal reflections.

Fig.50 shows the fan connections from the chamber electrodes to a Model C Marx Generator. Part of a crude version of a gas control and purification system is also visible. The two chambers were constructed and tested at the University of Michigan, then trucked intact to the Echo Lake Laboratory.

(3) FIDUCIAL SYSTEM

There were two rows of fiducial crosses with approximately 10 cm horizontal spacings and 15 cm vertical spacings on every piece of glass, except those for the 5 cm dummy gaps. Each cross consisted of lines 0.8 mm wide by 2.5 cm long and was sand blasted with number 180 silicone carbide grits. The depth of the crosses was about 70 μm.

The key to simple reconstruction from film to real space was to produce an identical pattern on all 32 pieces of glass such that only one set of relative positions of the crosses was needed. This was achieved by using a single 1.6 mm thick stainless steel mask with the fiducial pattern carefully cut into it with a fine circular saw on a milling machine. With the proper combination of pressure and flow rate in the sand blasting jet, sharp and consistant crosses were obtained. To achieve reproducability, the glass and mask were uniformly clamped to a flat

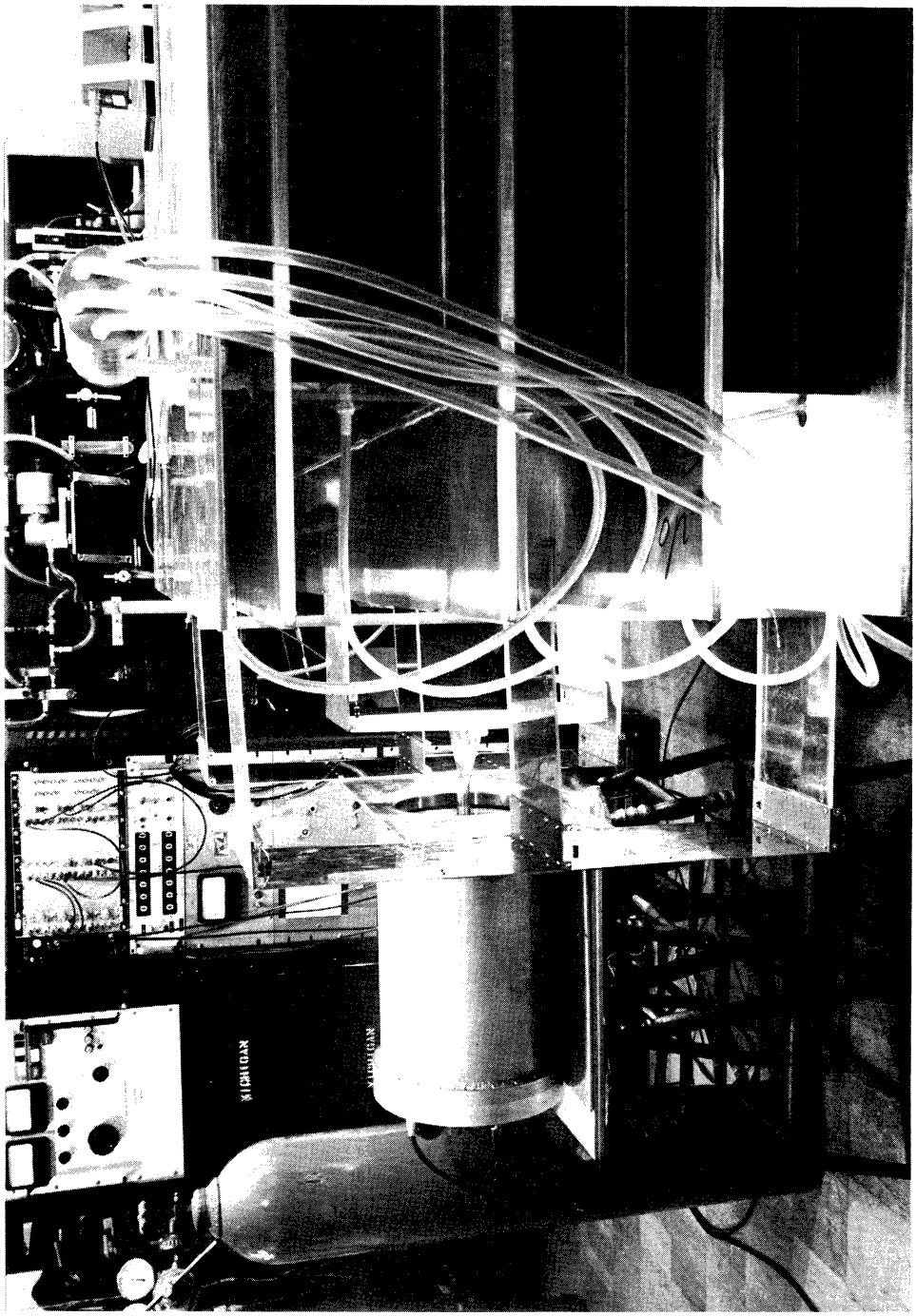

Fig.50 Fan Connections to the Marx Generator

table, and the mask's surface was shielded by 0.5 mm thick polyethylene tapes to prevent it from undergoing plastic deformation.

Eight pieces of the glass sand blasted on different days and representing the front windows of the critical view were taken to Argonne National Laboratory for surveying. A self-checking three-transit system travelling on two perpendicular 2.5 m tooling bars was employed to measure the relative x-z positions of the 38 fiducial crosses. With careful measurements, the rms point setting accuracy on the center of a cross was as high as $\pm$ 6.5 μm.

Fig.51 shows the distribution of individual x measurements from the values averaged over all glasses and all measurements. The standard deviation of 16 μm reflects both the measurement accuracy and the reproducability of the patterns.

(4) SURVEYING

After obtaining the relative coordinates of the fiducials on a single glass, the final question was to interrelate the glass positions in three dimensions.

A 0.15 mm phorsphor bronze wire stretched to 75% of its tensile strength by a 2 kg plumb bulb damped by mineral oil will form a very stable vertical reference. Four such lines were hung from the top of the upper chamber

table, and the mask's surface was shielded by 0.5 mm thick polyethylene tapes to prevent it from undergoing plastic deformation.

Eight pieces of the glass sand blasted on different days and representing the front windows of the critical view were taken to Argonne National Laboratory for surveying. A self-checking three-transit system travelling on two perpendicular 2.5 m tooling bars was employed to measure the relative x-z positions of the 38 fiducial crosses. With careful measurements, the rms point setting accuracy on the center of a cross was as high as $\pm$ 6.5 μm.

Fig.51 shows the distribution of individual x measurements from the values averaged over all glasses and all measurements. The standard deviation of 16 μm reflects both the measurement accuracy and the reproducability of the patterns.

(4) SURVEYING

After obtaining the relative coordinates of the fiducials on a single glass, the final question was to interrelate the glass positions in three dimensions.

A 0.15 mm phorsphor bronze wire stretched to 75% of its tensile strength by a 2 kg plumb bulb damped by mineral oil will form a very stable vertical reference. Four such lines were hung from the top of the upper chamber

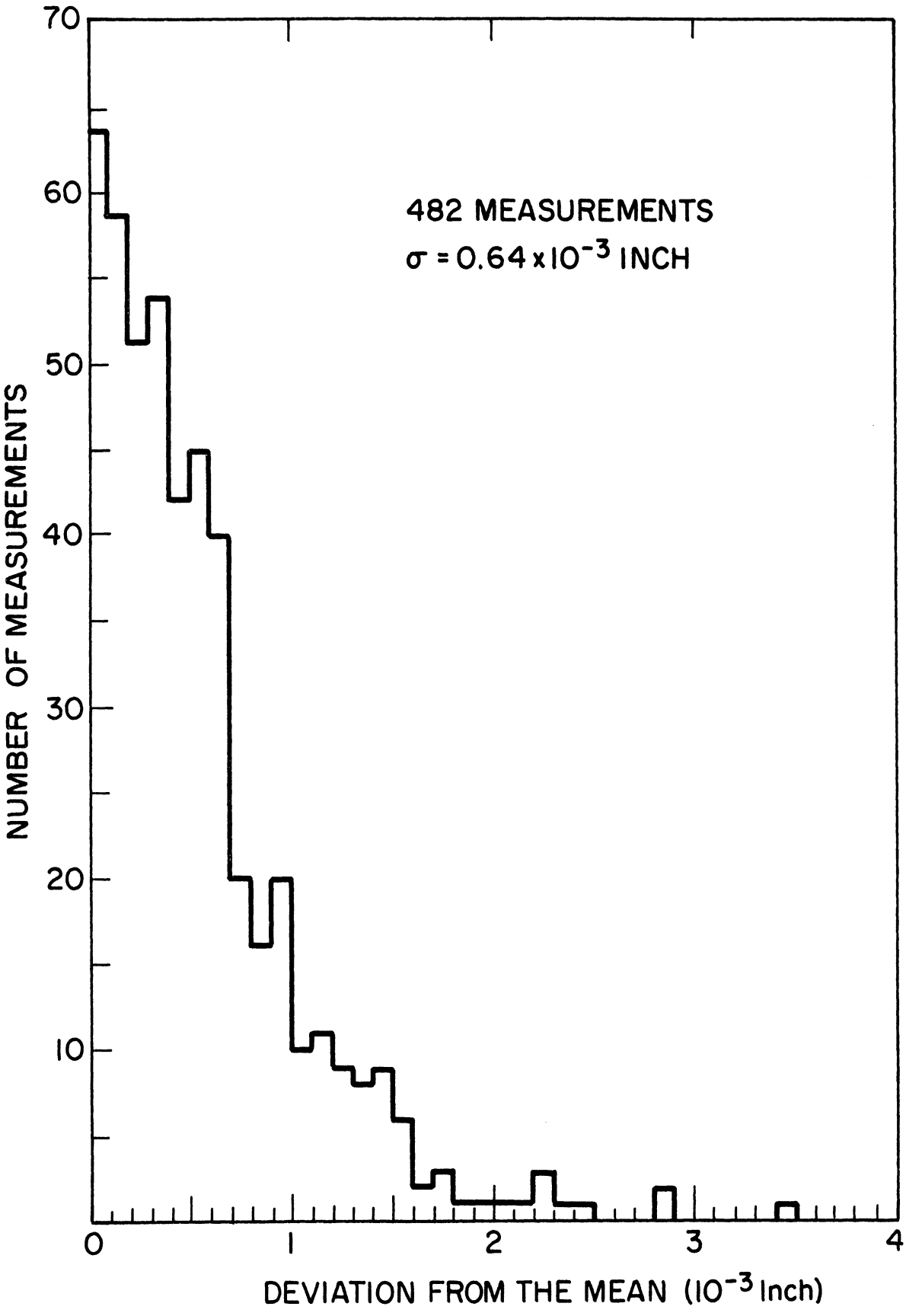

Fig.51 Precisions of the Fiducial Marks

through 1.9 cm holes in the electrodes of both chambers. The lines were adjusted to fall on the exact corners of a true rectangle ($\pm 50\,\mu m$ diagonal errors), hence constituting a set of master reference lines for x-y measurements.

Fig.52 portrays a completed chamber mounted with surveying instruments.

Basically, measurements were made by recording position changes in the optical axis of a cathetometer when it was moved between a reference line and a fiducial mark. Of the four degrees of freedom associated with a line in space, the two rotations must be constrained in order to record the two translations consistantly. In practice, it must be adjusted to be parallel to a level line in a plane defined by two of the reference plumb lines.

Fig.53 is a close-up look of the cathetometer mount. The dark disc at the lower middle of the picture is the cathetometer eye-piece. The horizontal adjustment was monitored by the sensitive ($48\,\mu r$/div) level directly above while the left right adjustment confined the optical axis to be in the plane of the near and far plumb lines. A "no-play" micrometer translational stage was used to make fine horizontal displacement measurements. The sliding of this stage on the vertical bar with a precision vernier scale allowed z measurements. Supported on two pivots, the vertical bar in turn could slide on the upper square frame and

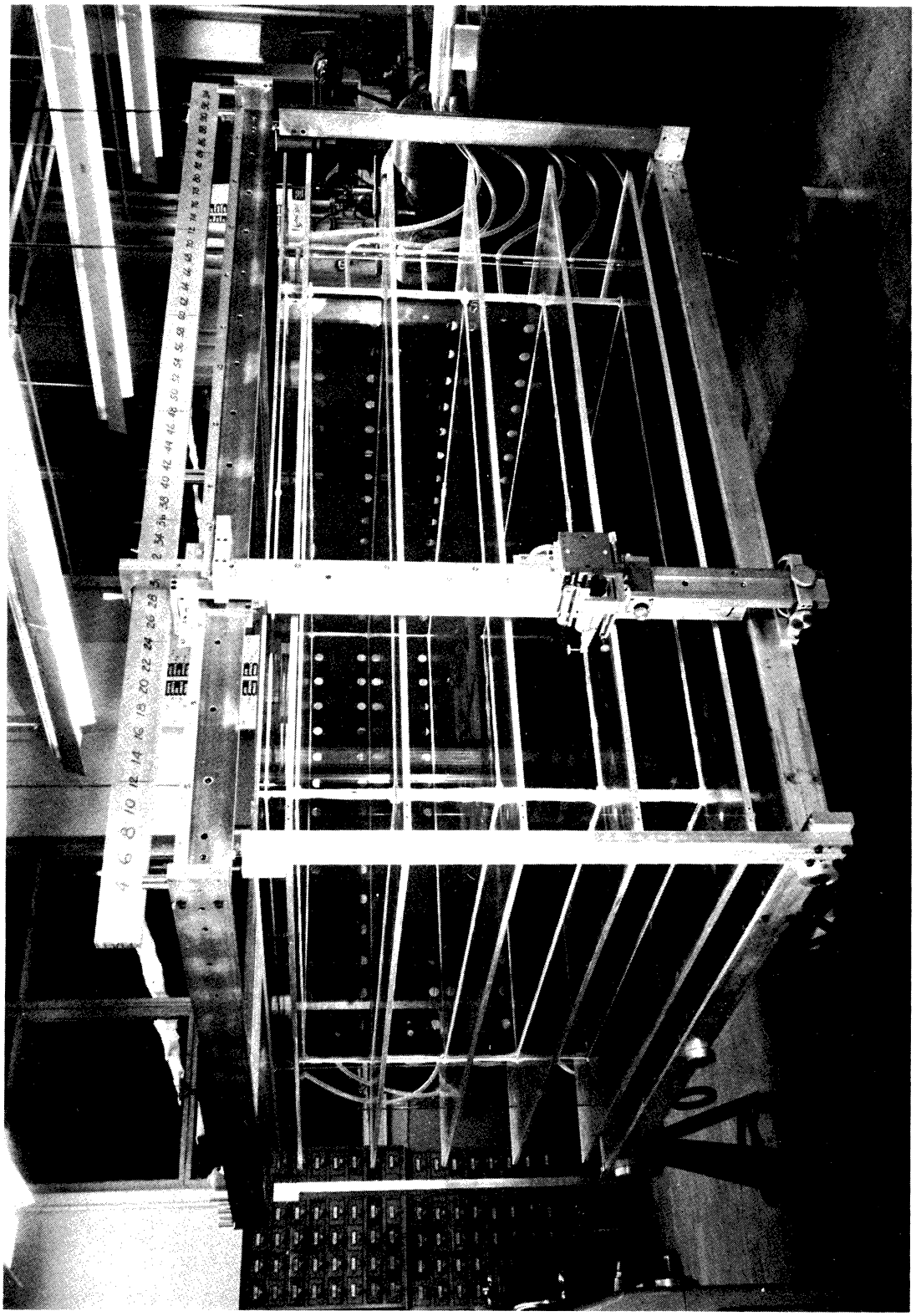

Fig.52 A Completed Chamber Mounted with Surveying Instruments

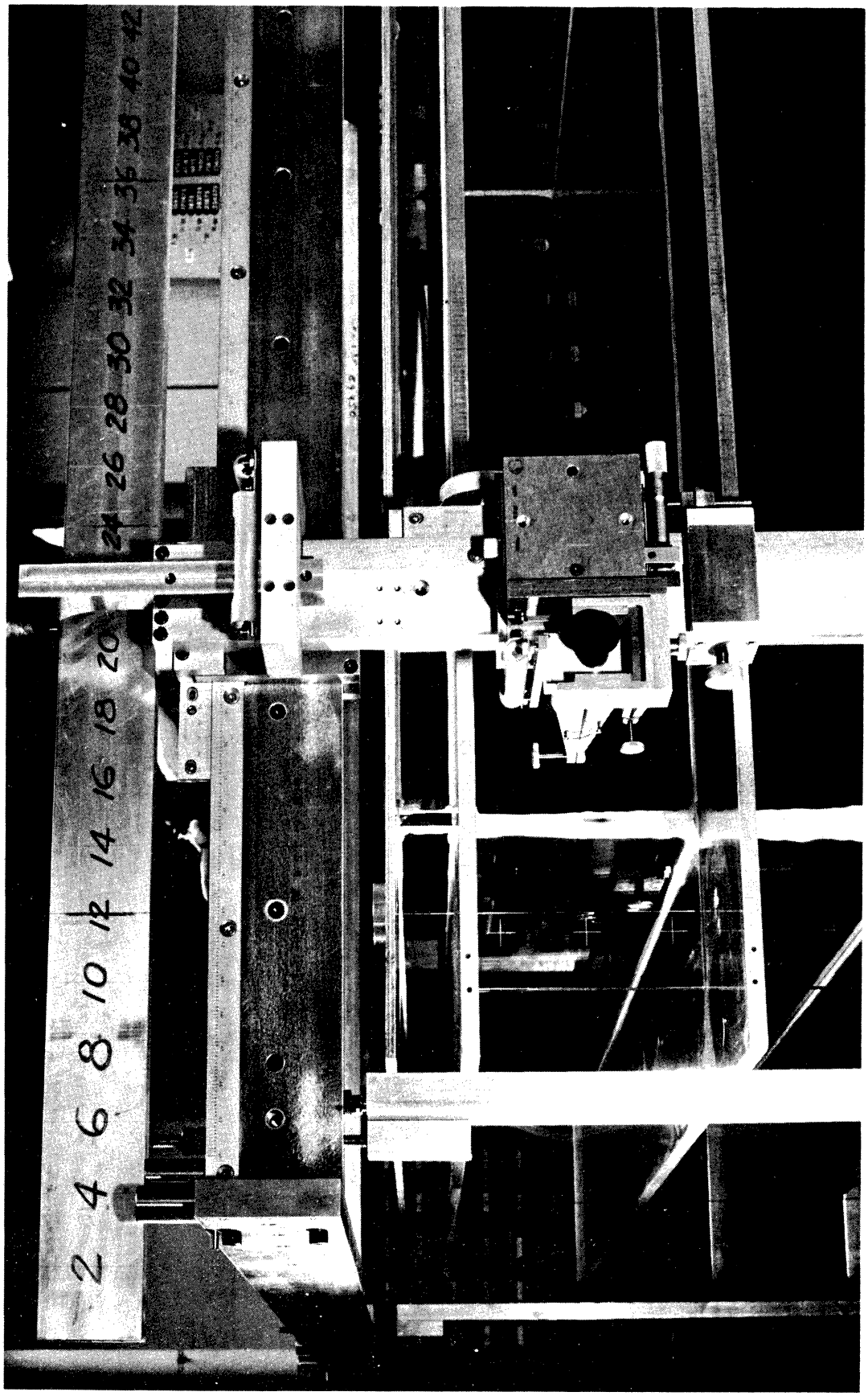

Fig.53 Details of the Cathetometer Mount

its orientation could be monitored by the two perpendicular levels near its top.

The leveling bar at the very top had been calibrated at the Argonne National Laboratory for deflections of various relevant spans. Its surface was also charted to 5 μm accuracy. It is seen that the micrometer at the very top could make a one-step z correction for the sag of the apparatus by measuring to the load-free leveling bar.

The effectiveness of the design was realized by purposefully locating the plumb wires near a set of fiducial marks, such that the critical x measurement could be made by a small smooth movement of the micrometer translational stage without touching other adjustments. Thus this measurement would be insensitive to any mechanical defect of the structures.

The depth informations were recorded by measuring the small distance between the glass and the plumb wire. A micrometer depth gauge was connected to an ohmmeter such that precise contact positions could be located without displacing the wire. Errors of less than 12 μm were typical.

Armed with the relative fiducial positions on a glass, one could deduce all fiducial coordinates from a simple measurement of the curvature of the glass when the corner fiducials were known.

Results of on site surveying had shown that the rms error was 19 μm for x measurements and about 40 μm for y and z measurements. Sensitive levels were mounted on all four sides of the chambers for continuous post-survey monitoring.

(5) PERFORMANCE

The multi-wide-gap chambers were test fired with helium filling at one atmosphere before being shipped to Colorado.

The threshold voltage for the development of sparks in helium was 101 kV. Above 110 kV, the track forming efficiency was virtually 100%. Resistor strings could be plugged in near the corners to give a RC time constants of 1-10 μsec, although voltage was usually terminated by tracks themselves. When the gas conditions were equally good in all the gaps, there was little intensity difference among the sparks. On the other hand, any inbalance in track intensity could be easily corrected by inserting relative amounts of series resistances of 1-20 ohms in the current return loops at the fan connections.

Figures 54-58 show the characteristics of helium tracks from 120 to 200 kV in 20 kV increments. Note the gradual transition from very smooth spark channels at low voltages to very lumpy ones at high voltages. This behavior

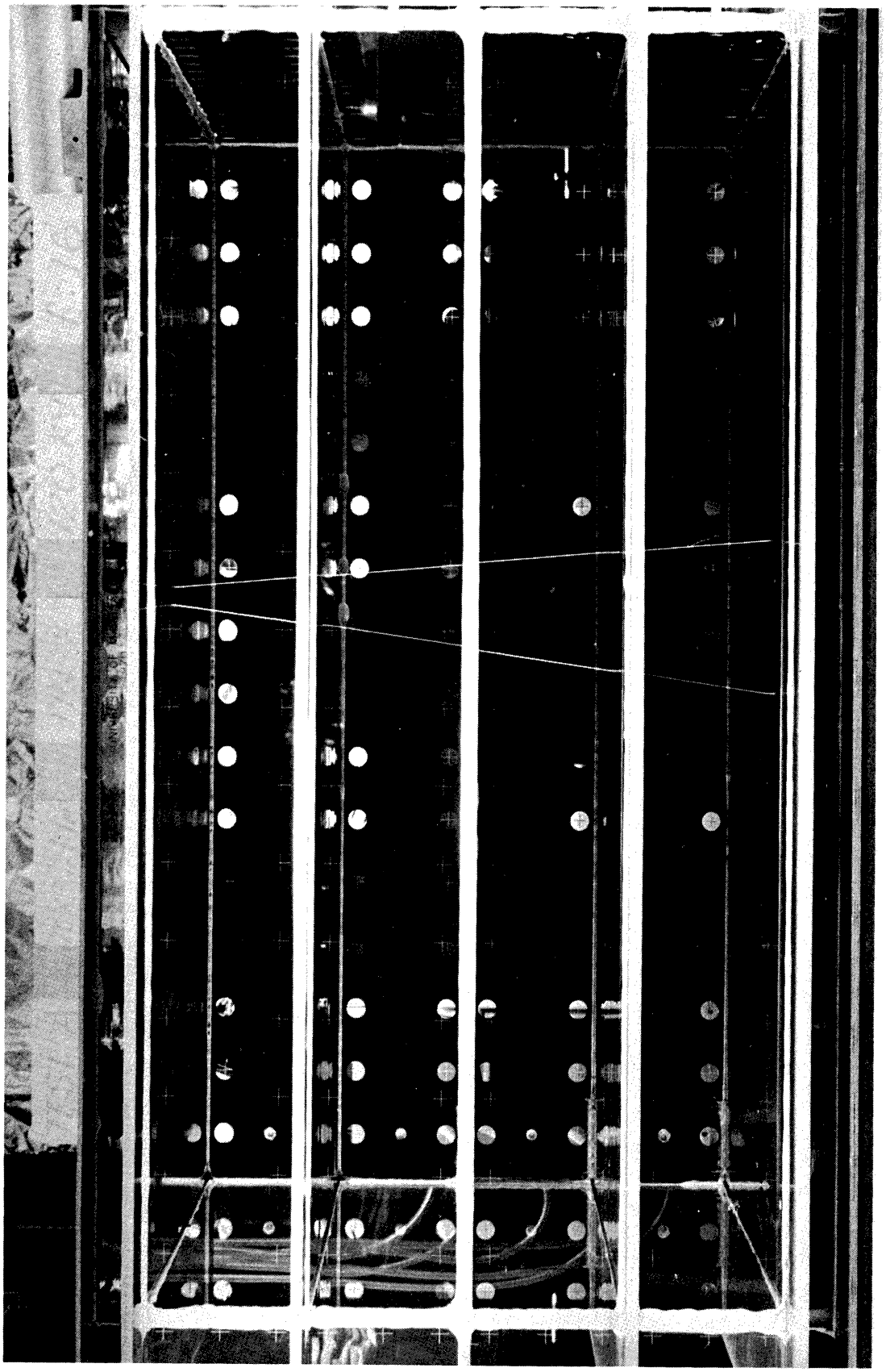

Fig.54 Spark Characteristics at 120 kV

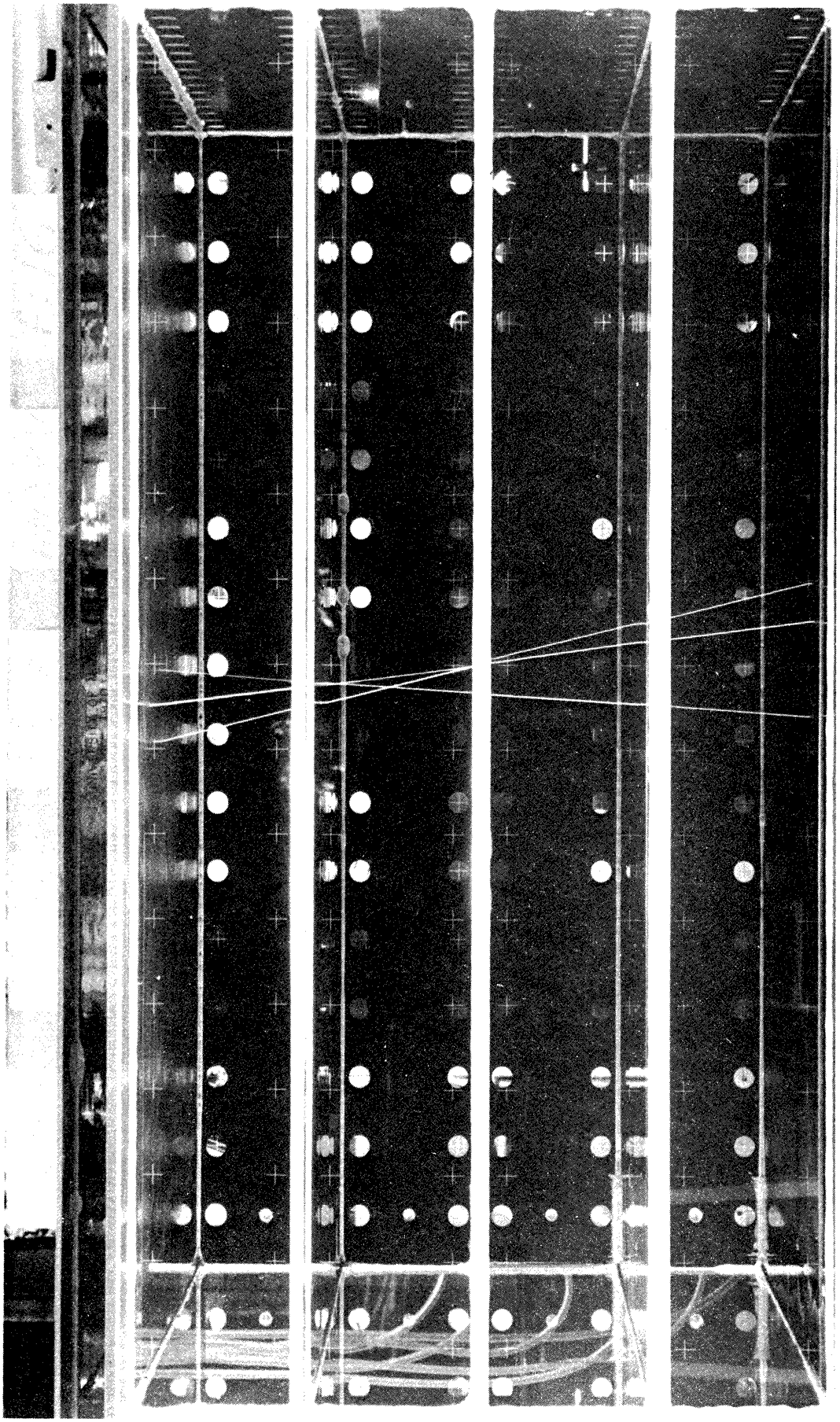

Fig.55 Spark Characteristics at 140 kV

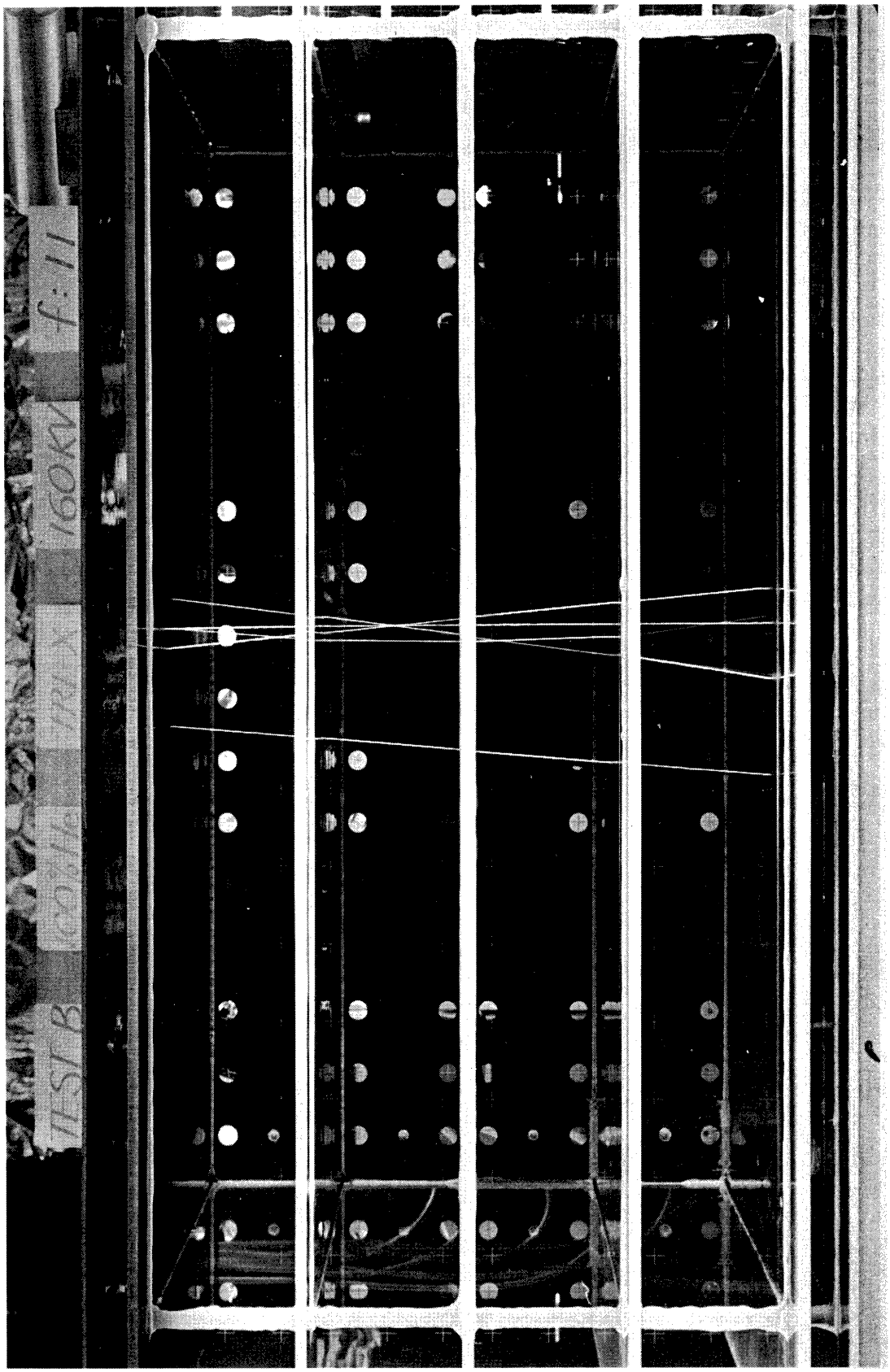

Fig.56 Spark Characteristics at 160 kV

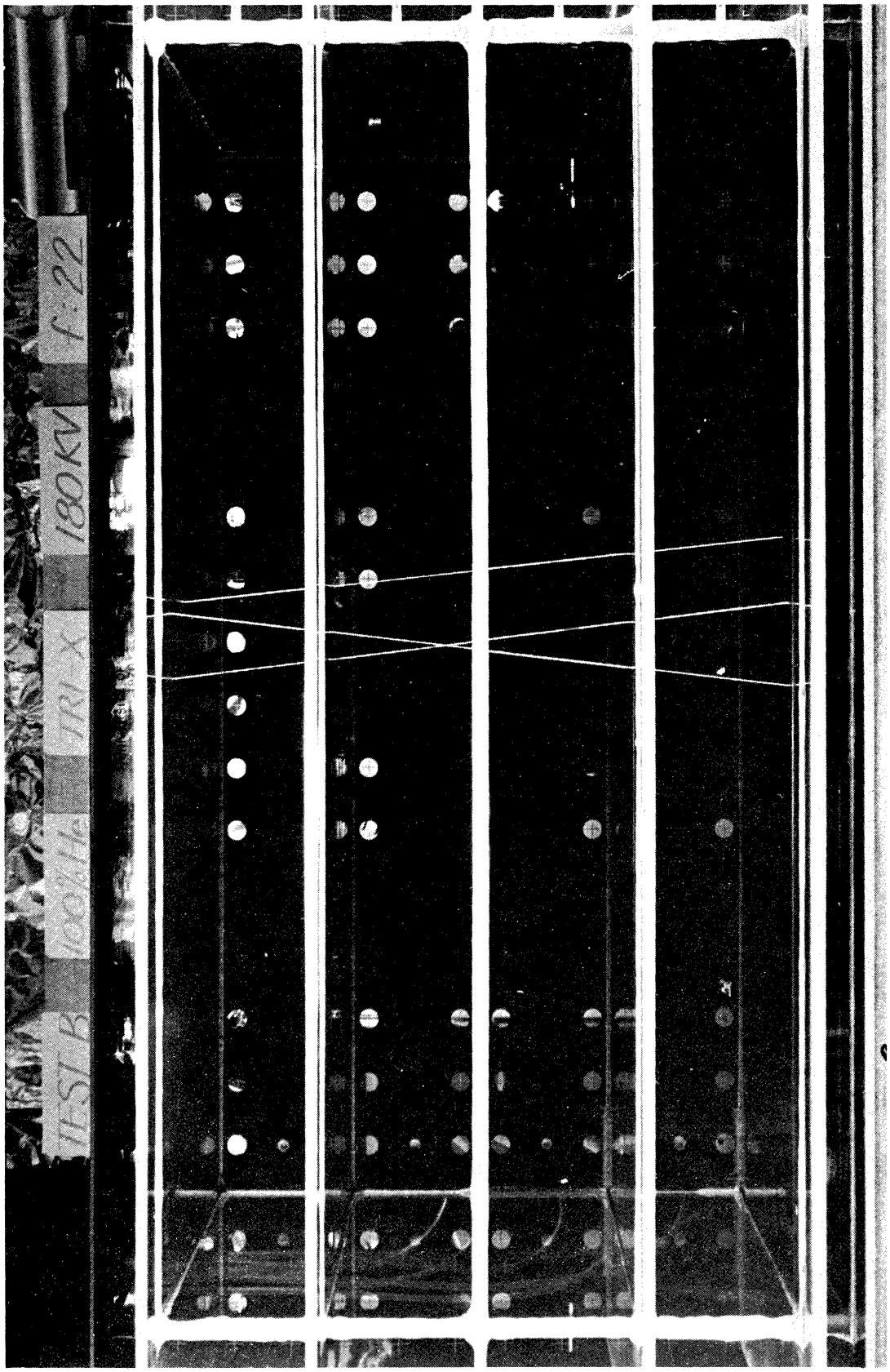

Fig.57 Spark Characteristics at 180 kV

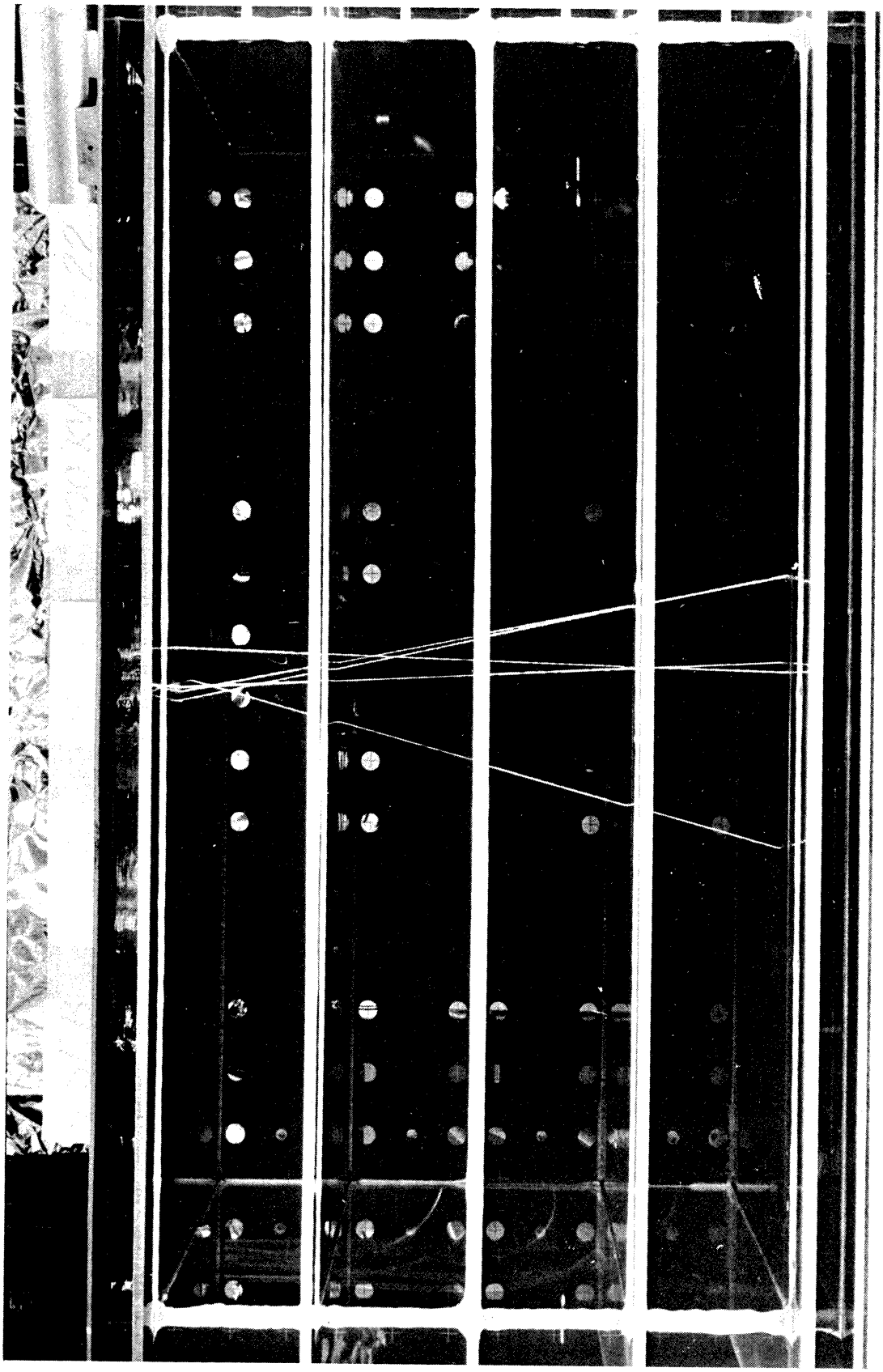

Fig.58 Spark Characteristics at 200 kV

is expected from the known process of spark formation. The Townsend coefficient α increases with the field strength E thus the Meek condition is satisfied at a shorter distance. This means that the linkage between neighboring streamers will be less effective and spark development will show more local characteristics. Furthermore, while the growth of a streamer along the electric field is heavily field dependent, the transverse growth is primarily a diffusion process. Thus when the spark formation time becomes shorter at higher fields, the transverse linkage with neighbors is even more difficult in an inclined track, and isolated developments become more prominent.

It is clear that operating a wide-gap chamber very much above its threshold voltage is not desirable as far as obtaining the best spacial resolution is concerned. The most accurate spark will be developed if plenty of time is allowed for streamers to socialize with their neighbors and smooth out any local fluctuations.

Fig.59 shows the result of digitizations of single sparks in neon at 500 torr and the advantage of low voltage operation is evident. The intrinsic angular resolution was estimated according to

$$\Delta\theta = \frac{2\epsilon}{L\sqrt{N}} \quad ,$$

where ϵ is the rms deviation of the digitization points

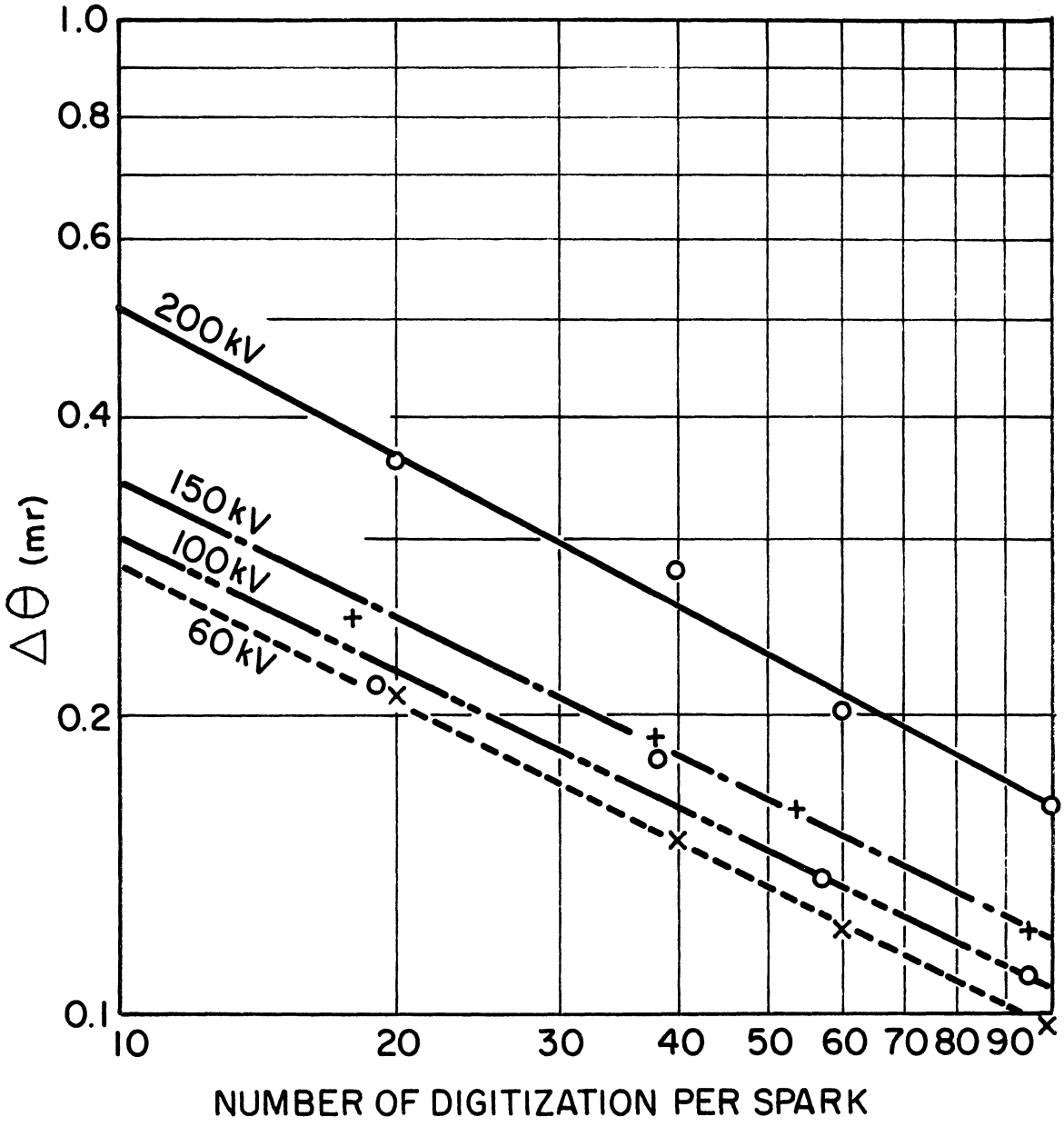

Fig.59 The Intrinsic Angular Resolution of a Single Spark

from a straight line fit, L the useful spark length and N the number of digitizations. This estimate is slightly more conservative than the expression developed on page 76.

The addition of C_2H_5OH was also known to be able to reduce local spark fluctuations,[36] but a factor of two in resolution is gained at the expense of over a factor of 50 loss in spark brightness.

Fig.60 is an air shower accidently detected during the testing of the chamber. Unfortunately the camera was then focused on the front glass, and the film was Kodak Panatomic X. Nevertheless, over 90 tracks were resolved.

(6) CONCLUSION

The performance of the multi-wide-gap chamber has demonstrated that large and precise detectors are entirely practical. With some care in design and construction systematic sources of error can be kept smaller than the intrinsic resolution in the spark whose ultimate precision depends on the optimum mode of operation that is possible in a given situation.

So far we have only considered problems at the source. In practice, equivalent attention must be given to the other links in the chain of information transmission. The questions of lens distortion, film flatness, and digitization if not properly handled all may contribute to the

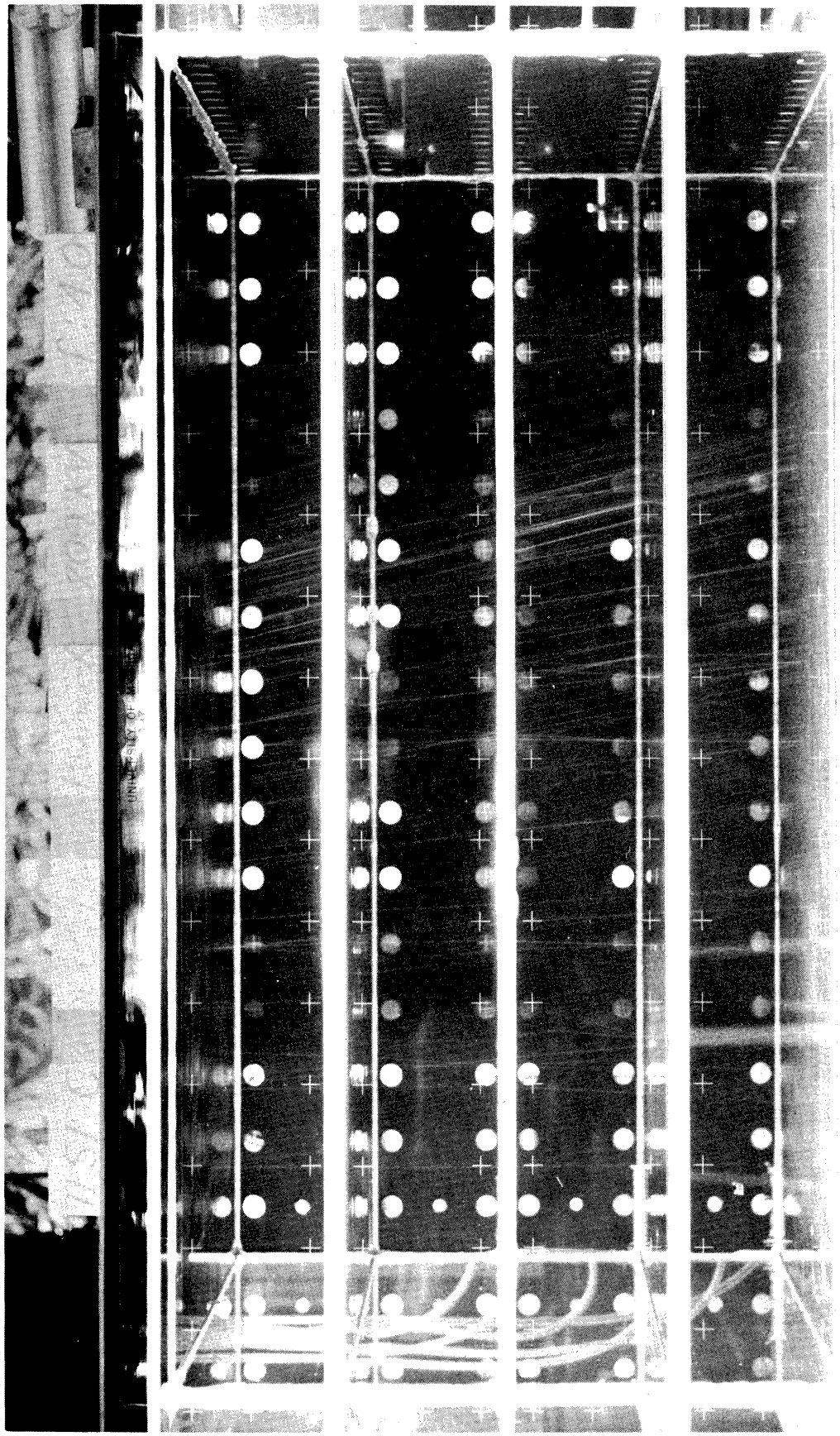

Fig.60 An Air Shower of Over 90 Resolved Tracks

degradation of the intrinsic resolution which was seen to be about 100 μr at N = 100 in one gap, or 50 μr in four gaps. Thus the M.D.M. for the Echo Lake magnetic spectrometer could be as high as 5.5 TeV/c.

CHAPTER V

PROTON-IRON INELASTIC CROSS SECTIONS

A. THEORETICAL CONSIDERATIONS

The p-p inelastic cross section exhibits little energy dependence between 70 and 1,000 GeV.[37] Recent observations on attenuation of primary proton flux by air nuclei indicated at least an 8% rise in cross section between 70 and 3×10^4 GeV.[38] It is of interest to see if energy dependence of p-nucleus cross section can nevertheless be compatible with a flat p-p cross section.

The theoretical approach to this problem is usually to seek a way of calculating the elastic scattering amplitude F(t), where t is the square of the four momentum transfer to the target nucleus, and is related to the angular differential cross section by

$$\frac{d\sigma}{d|t|} = \frac{\pi}{p^2_{lab}} F(t)\, F^*(t) \quad .$$

The total cross section σ_T is then deduced from the optical theorem

$$\sigma_T = \frac{4\pi}{p_{lab}} \text{Im}\, F(0) \quad ,$$

and inelastic cross section is taken as the difference be-

tween total and elastic cross sections. At very high energies and heavy nuclei, the real part of the scattering amplitude is assumed to be negligible.

The simplest description of the scattering process is the optical model in which the nucleus presents itself collectively as an optical potential $V(\underline{r})$. The wave equation is

$$(\nabla^2 + k^2)\, \Psi(\underline{r}) = V(\underline{r})\, \Psi(\underline{r}) \quad .$$

Using the eikonal approximation $\Psi(\underline{r}) = e^{ikz}\, \varphi(\underline{r})$ and the fact that scattering is forward-peaked at high energies, the wave equation is reduced to

$$\frac{d}{dz}\, \varphi(\underline{r}) = \frac{1}{2ik}\, V(\underline{r})\, \varphi(\underline{r}) \quad ,$$

and

$$\varphi(\underline{r}) = \exp\left[\frac{1}{2ik} \int_{-\infty}^{z} V(\underline{r}')\, dz'\right] \quad .$$

For a heavy nucleus of mass number A, $V(\underline{r})$ can be approximated by

$$V(\underline{r}) = -4\pi A\, f(0)\, \rho(\underline{r}) \quad ,$$

where $f(q)$ is the nucleon-nucleon scattering amplitude, $\rho(\underline{r})$ the nuclear density distribution, and $q = \sqrt{-t}$ is the momentum transfer. Finally, $F(q)$ is calculated by an impact parameter expansion

$$F(q) = \frac{ik}{2\pi} \int_0^{\infty} J_0(qb)\left[1 - \varphi(b,z)\right] b\, db \quad ,$$

with $\underline{r} = \underline{b}+\underline{z}$ and J_o is the zeroth order Bessel Function.

Therefore given the nuclear density distribution nucleon-nucleon cross sections, the optical model can be used to calculate nucleon-nucleus cross sections.

If $\rho(\underline{r})$ is constant for $r<r_o$ or a Gaussian function, there will be analytical solutions. But it is more realistic to use the Woods-Saxon form of

$$\rho(r) = \frac{\rho_o}{1+\exp\left[\frac{4.4(r-a)}{b}\right]} .$$

For iron the half-density radius a and the 90-10% skin depth b are about 4.0 f and 2.4 f respectively.[39] Note that for the optical model this calculation would lead to no energy dependence for the cross section as long as f is independent of energy and V is very small compared to the particle energy.

Glauber has developed a model in which a proton undergoes multiple diffractive reactions with the nucleons.[40,41] It may lead to similar results as the optical model but it could also display in the form of a series the contributions to the scattering amplitude from single nucleon interactions and increasingly higher order processes in which internuclear shadowing and the correlation of intranuclear coordinates play a role. Thus the model also requires two input functions; the nucleon-nucleon amplitude f(q) and the nuclear form factor S(q) which is the Fourier

transform of the density distribution $\rho(\underline{r})$

$$S(q) = \int e^{i\underline{qr}}\, \rho(\underline{r})\, d\underline{r} \quad .$$

Trefil has incorported the effect of inelastic intermediate states, first proposed by Abers et al., to the Glauber calculation.[42,43] The nucleon-nucleus elastic scattering amplitude is written as

$$F = F_o + \sum F_i$$

where F_o is the amplitude calculated according to the normal Glauber theory and F_i represents the contribution to the elastic scattering from an intermediate N* if the i^{th} kind and the summation is taken over all N* which can participate in the reaction according to

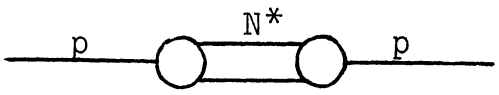

without violating the coherency requirement

$$q \cdot D \lesssim \hbar \quad ,$$

where q = momentum transfer $\approx \dfrac{m_i^2 - m^2}{2p}$, and D is a characteristic distance of the order of the nuclear diameter. The p-N* coupling is assumed to be of the form $G_i(m_i) = P(x)\, e^{-x}$ where $x = \dfrac{m_i}{m}$ and P(x) is a polynomail in x. It was also assumed that except for the coupling factor N*, production cross sections are similar to that

for the N*(1480) which has an energy independent cross section of 0.8 mb. Thus

$$\sum_i \sigma_i^* = \frac{0.8}{|G(1480)|^2} \sum_i |G_i(m_i)|^2 < 30 \text{ mb} \quad .$$

The last inequality is a condition imposed to assure that P(x) will sensibly behave since the total p-p inelastic cross section is approximately 30 mb.

The results of Trefil's calculation is shown in Fig.61 for energy independent p-p cross sections. The solid lines are the Glauber model results. The dotted and the dashed curves represent,respectively, the choices

$$P(x) = 1+x+\frac{x^2}{2} \; ; \; \sum \sigma_i^* = 19 \text{ mb} \quad ,$$

and

$$P(x) = 1+x-x^2 \; ; \; \sum \sigma_i^* = 28 \text{ mb} \quad .$$

It is seen that the shadowing effects of inelastic intermediate states on total and elastic crosssections are of comparable magnitude and saturate at about 400 GeV, leaving the inelastic cross section rather insensitive to energy.

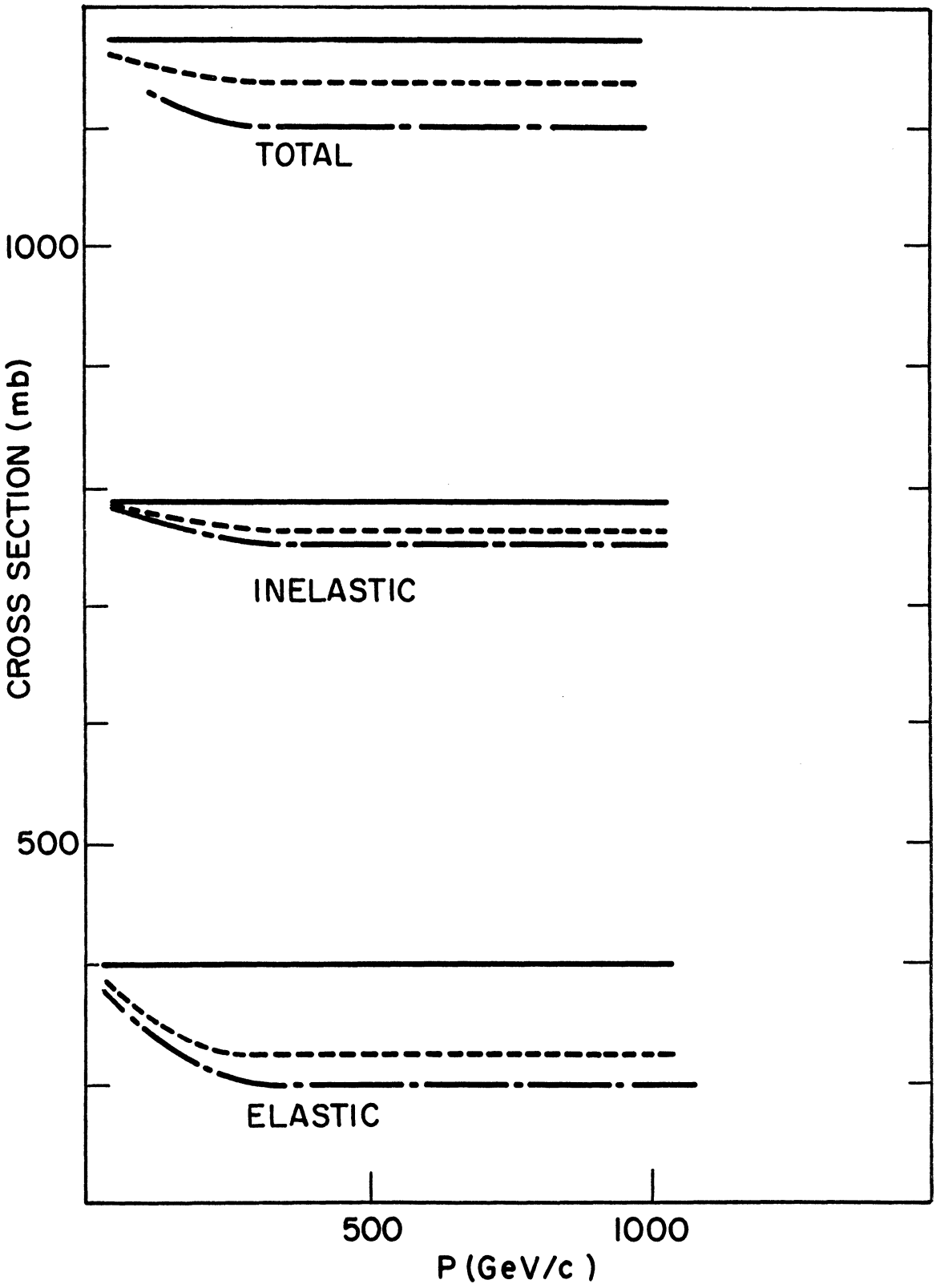

Fig.61 Theoretical Predictions of Proton-Iron Cross Sections

B. DESCRIPTION OF EXPERIMENT

The experimental set-up is already illustrated in Fig.5 and briefly described in chapter I, section F. More comprehensive and detailed descriptions are given in References (44) and (37). We shall only mention some features that are essential for the discussion for this phase of the experiment.

The thin foil wide-gap spark chambers as described in chapter IV were to define the trajectory of the incident particle. The anticoincidence guard ring and a visual scan of the photographic film assured that no more than one particle had traversed the fiducial volume of the system, particularly into the calorimeter.

The ionization calorimeter is shown in Fig.62. It is about 100 tons of iron interleaved by 10 scintillation layers which are viewed by 80 photomultiplier tubes. The details of placement and size of scintillators are summaried in table 3. The top section (above layer 3) also contain 10 narrow-gap (19 mm) spark chamber modules for visual study of cascade developments. All chambers were photographed by a single camera through strip mirrors in each of the two 90° stereo views. Fig.63 is an illustration of an "unfolded" event by proper magnifications of different segments of the film in order to restore the approximate real space relationships. Note that the cas-

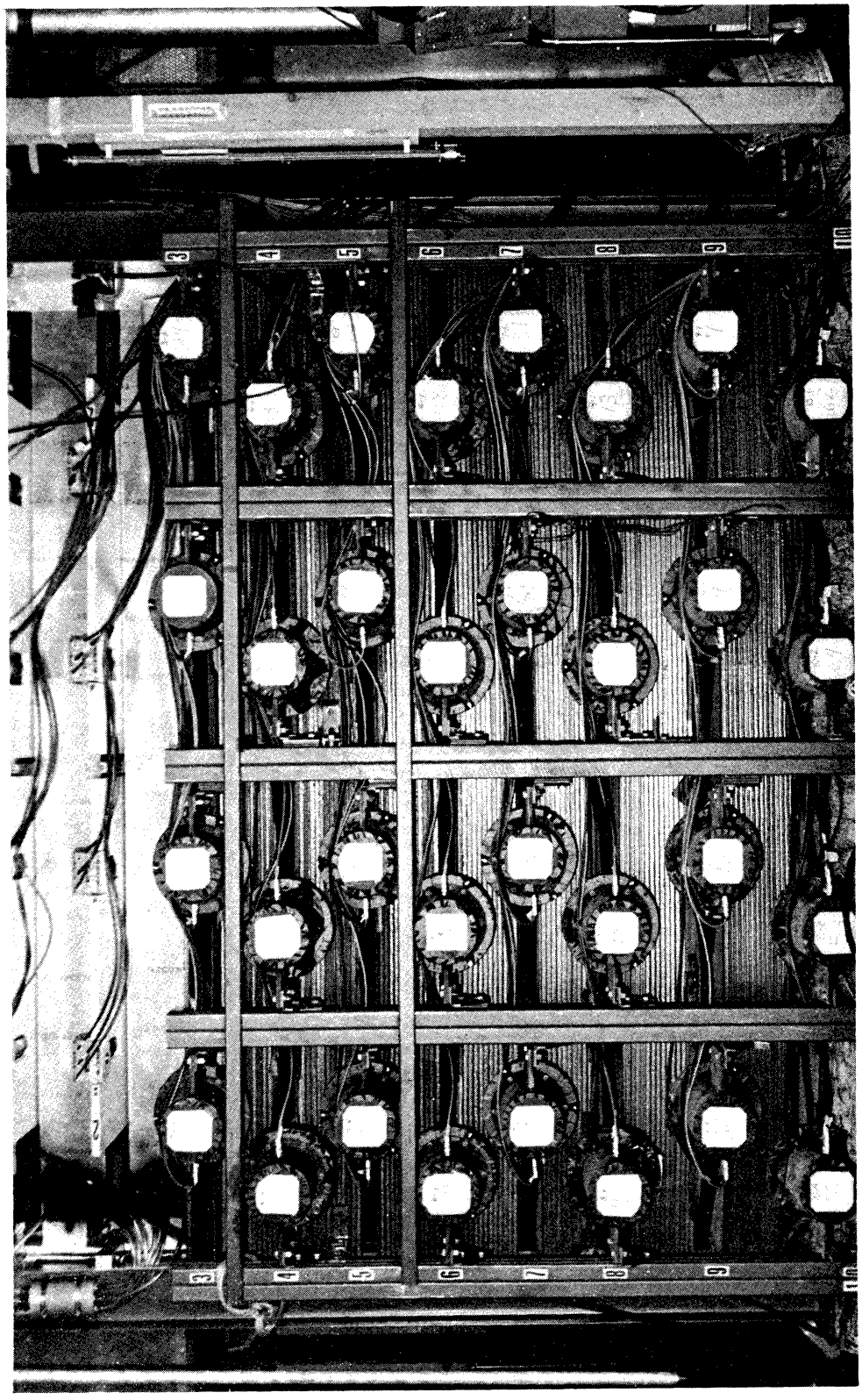

Fig.62 Front View of the Ionization Calorimeter

Table 3

Locations and Sizes of Scintillators in the Calorimeter

Scintillator Layer	z-Coordinate (cm)	Depth of Iron from top of Calorimeter (gm/cm^2)	Area of one Half Layer (m^2)	Thickness of Scintillator (cm)	Type of Photo-multiplier Tubes
Top Counter	120.13		0.914x1.829	1.91	RCA 6810
Layer 1	-131.3	40	0.914x1.829	1.91	RCA 6810
Layer 2	-155.7	120	0.914x1.829	1.91	RCA 6810
Layer 3	-184.9	210	1.219x2.438	3.81	EMI 9816
Layer 4	-205.8	330	1.219x2.438	3.81	EMI 9816
Layer 5	-226.4	450	1.219x2.438	3.81	EMI 9816
Layer 6	-247.6	570	1.219x2.438	3.81	EMI 9816
Layer 7	-267.6	690	1.219x2.438	3.81	EMI 9816
Layer 8	-287.9	810	1.219x2.438	3.81	EMI 9816
Layer 9	-313.7	970	1.219x2.438	3.81	EMI 9816
Layer 10	-338.8	1130	1.219x2.438	1.91	EMI 9816

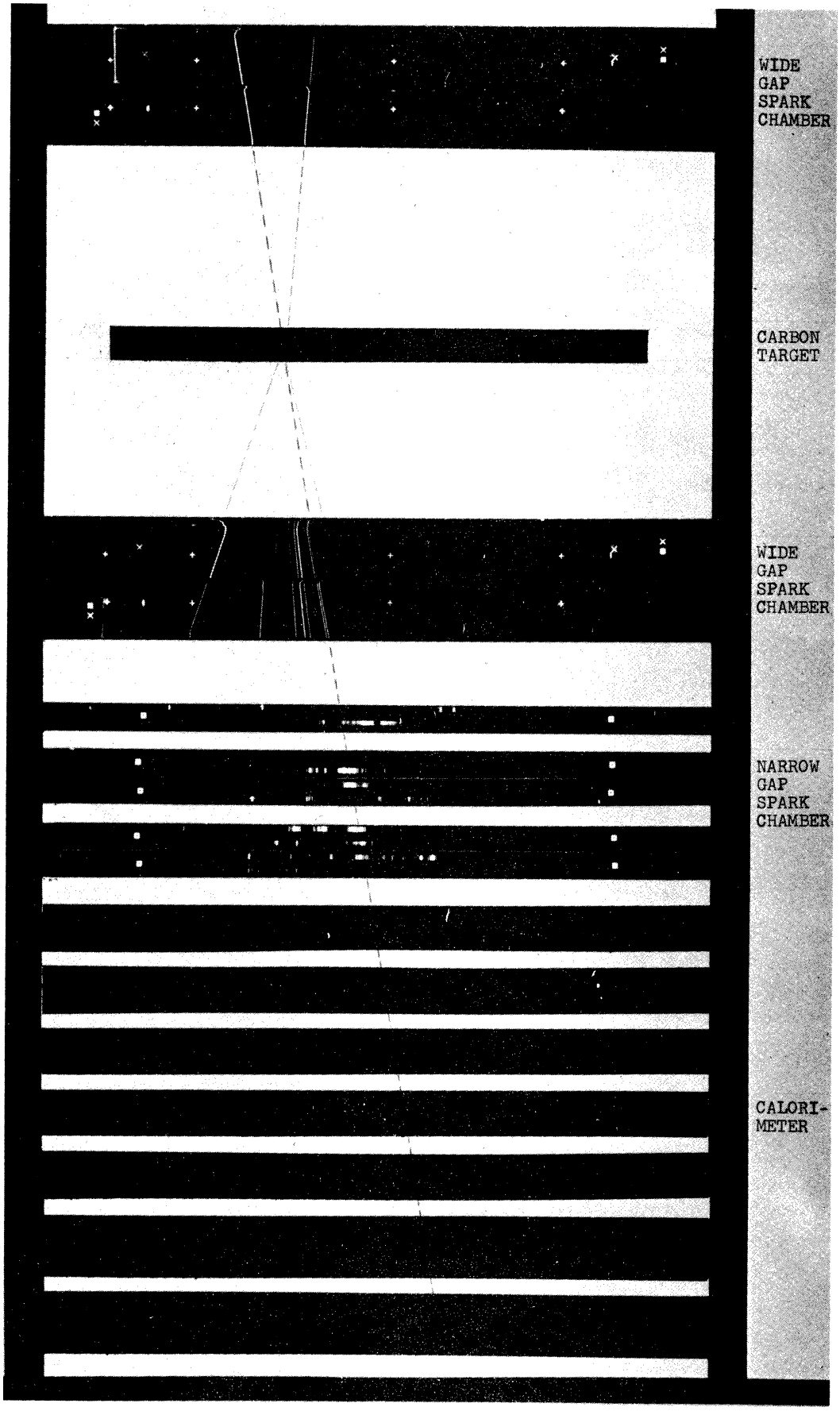

Fig.63 A Proton Interacted in the Carbon Target

cade development in the narrow-gap chamber also helps to identify the incident proton from the particle which back scattered from the target.

C. DATA ACQUISTION AND PROCESSING

Fig.64 shows the block diagram of the triggering and recording electronics. It is seen that the top counter, layer 2 and the sum of layers 1 through 9 of the calorimeter constituted a charged hadron coincidence trigger. On occasions, the top counter, layer 1 and layer 10 combination was used as a muon coincidence trigger. The shower counter guard-ring (7.68 m^2 total area) was of course in anticoincidence for both triggers.

The outputs of eight photomultipliers of each layer were summed passively. The pulse area, which was more representative than the time gittering pulse height of such a sum signal was then recorded by a logarethmic analog to digital converter (LADC). The 128 channels of each LADC covered a dynamic range of about 60 db and they were calibrated every few days for linearity and compared with the mean muon pulse area which was recorded at the same time as a standard reference of a minimum ionizing particle.

The spark chamber films and the magnetic tape containing the calorimeter data together with LADC and muon

ECHO LAKE COSMIC RAY EXPERIMENT

ELECTRONICS BLOCK DIAGRAM

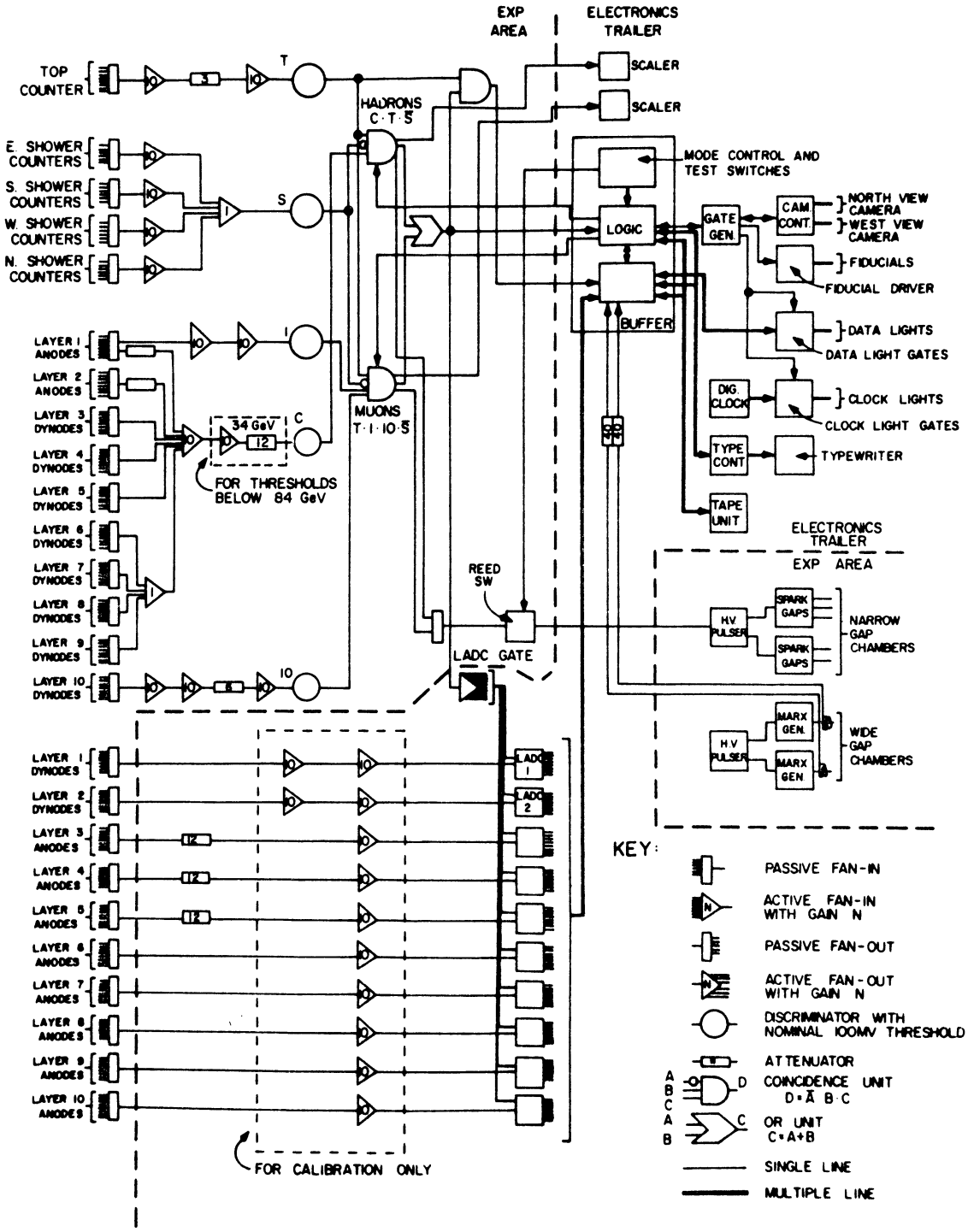

Fig.64 Electronic Block Diagram of the Echo Lake Cosmic Ray Experiment

calibrations were then the raw recorded data of the experiment.

The films were developed at the Argonne National Laboratory and then forwarded to the University of Michigan for prescanning and measuring. The calorimeter tape was first edited at the National Center for Atmospheric Research in Boulder, Colorado and sent to the University of Wisconsin for energy evaluation.

The film pre-scanning sorted out those events with interactions in targets from the "straight throughs", which are the transmitted flux, and rejected all inefficient or contaminated events. All the interactions were analyzed with the Wisconsin 1 μm least count manual measuring microscope and all the straight throughs were measured with the Michigan Automatic Scanning System (MASS). MASS is a programmed-spot digitizer controlled by a DDP 124 computer. It digitizes 13 points per spark and has an effective resolution of 5 μm on the film. The two MASS output tapes for the North and West orthogonal views were then merged at ANL with records paired according to event numbers. Reconstructions were accomplished by the program named Cosmic which included correction for optical distortions, rejection of some out-of-geometry events, and computation of the intersection of a particle's trajectory with the x-y plane and the directional cosines. In the real space coordinates, the x-y plane lies in the mid-plane of

the hydrogen target, with the x axis pointing north, and z is the line of symmetry along the zenith. Finally, the proccessed calorimeter data in terms of number of equivalent muons in each layer was added to each event which had been successfully processed by Cosmic. A similar output tape was generated from interacting events for further analyses. The seemingly scattered effort was only the result of making maximum use of all available computing, film processing and measuring facilities.

A condensed tape of 50,000 straight through events was the basis for the following analysis.

D. METHOD

Assume a particle comes within the fiducial volume of the apparatus and is stopped in the calorimeter without making an interaction in the target. Let its zenith angle be measured by the spark chambers and its energy determined by the calorimeter and sorted into a particular energy bin. The layer in which the first inelastic interaction occurs is detected by the subsequent scintillation counter which shows an anomalously large pulse (greater than some detection threshold D in terms of equivalent number of muons). The interaction mean free path λ_{Fe} can then be determined from its reciprocal γ_{Fe} by a maximum likelihood calculation.

The likelihood function is of the form

$$L(\theta,j,k,\gamma) = \prod_{i=1}^{N} f_i(\theta,j,k,\gamma) \quad ,$$

where $f_i(\theta,j,k,\gamma)$ is the normalized probability that the i^{th} particle with incident zenith angle θ in the k^{th} energy bin would interact inelastically in the j^{th} layer of the calorimeter. Its explicit form is

$$f_i(\theta,j,k,\gamma) = \frac{\exp\left[-\gamma z(j_i-1)\sec\theta_i\right] - \exp\left[-\gamma z(j_i)\sec\theta_i\right]}{1 - \exp\left[-\gamma z_m(k_i)\sec\theta_i\right]}$$

where $z(j)$ is the vertical depth of the j^{th} scintillator in gm/cm^2 of iron and $z_m(k)$ is the verticle depth of the last scintillator used in the calculation for the k^{th} energy bin.

γ_{Fe} is then determined by

$$\frac{\partial W}{\partial \gamma} = 0$$

where $W = \ln L$.

If we call

$$A = z(j_i-1)\sec\theta_i$$

$$B = z(j_i)\sec\theta_i$$

$$C = z_m(k)\sec\theta_i$$

and summations are over all particles in any energy bin, then

$$W = \sum -\gamma A + \sum \ln\left(1-e^{-\gamma B}\right) - \sum \ln\left(1-e^{-\gamma C}\right) \quad ,$$

$$\frac{\partial W}{\partial \gamma} = \sum -A + \sum \frac{B}{e^{\gamma B}-1} - \sum \frac{C}{e^{\gamma C}-1} \quad .$$

The equation $\frac{\partial W}{\partial \gamma} = 0$ has no analytical solution. So $\frac{\partial W}{\partial \gamma}$ is called the residue and a numerical calculation by iteration technique is performed. The zero-crossing point may be determined to an arbitrary degree of precision. In practice, the convergence is rather rapid and linear. Three iterations will usually give an error of less than 10^{-4} in γ.

Concurrently an evaluation is also done on

$$\frac{\partial^2 W}{\partial \gamma^2} = - \sum \frac{B^2 \, e^{\gamma B}}{(e^{\gamma B} - 1)^2} + \sum \frac{C^2 \, e^{\gamma C}}{(e^{\gamma C} - 1)^2} \quad ,$$

and the experimental uncertainty is represented by

$$\Delta \gamma_{Fe} = \left[- \frac{\partial^2 W}{\partial \gamma^2} \right]^{-1/2}$$

which is exactly one standard deviation if W is normally distributed.

Ideally, λ_{Fe} is determined for each energy bin and a least square fit of the experimental points will yield the energy behavior of cross section desired. Almost no experiment is ideal and this one is no exception.

E. SYSTEMATIC PROBLEMS AND SOLUTIONS

There were over a dozen systematic problems that might either prevent a correct determination of λ_{Fe} or introduce an energy biased effect. Many were expected at the

outset but others became apparent or were isolated only after extensive searches and cross-checking.

Fortunately many effects, once recognized, could be dealt with quite effectively simply by restricting data inclusion through imposing various boundary conditions. As a result, of the 50,000 original events, only 6588 survived the wield of the axes. The principle of parsimony was adhered to at the expense of badly needed statistics; but the otherwise compounding of numerous correction uncertainties could be overwhelming.

Table 4 is a summary of the 15 problems and their treatments. Some problems may have arisen out of physical processes, but since the effects are distinct, they will be labled and discussed separately:

(1) Time Variation of LADC Setting: This was only a problem in the early portion of the data where the attenuation was set too high for layer 1 of the calorimeter. Thus low energy events that did interact in layer 1 usually did not give an output signal until deeper down --- λ_{Fe} would appear to be too high. This situation was avoided by skipping all events with energy less than 211 GeV for the first 10406 events.

(2) Energy Trigger Threshold: Many problems were associated with the statistical nature of the nuclear cascade development which itself reflected collectively the

PROTON IRON INELASTIC CROSS SECTION ABOVE 70 GeV

	SYSTEMATIC PROBLEMS	EFFECTS	LAMBDA TOO HIGH	LAMBDA TOO LOW	SOLUTION	PROCEDURES
1	Time Variation of LADC Setting	Attenuation too high on layer 1 in initial portion of data	✓		DATA SAMPLE SELECTION	Skip over 10406 events for E≤211 GeV
2	Energy Trigger Threshold	Energy overestimated and flux supressed for near threshold events	✓		ENERGY CUT	70 GeV for 36 GeV triggers 211 GeV for 90 GeV triggers
3	Side Leakage	Energy underestimated. Detection Efficiency reduced		✓	GEOMETRY CUT	Top counter + layer 2 + Variable Layer 10 size Guided by $\Delta\lambda$ min. Final layer 10 size = $(260\ cm)^2$.
4	Non Uniform Scintillator Response	Inacturate energy evaluation			ENERGY EVALUATION	Start LADC summation one layer ahead of layer of interaction as detected at given level. Include correction functions for bottom leakage and position variation of scintillator response
5	Bottom Leakage	Energy underestimated				
6	Delta Rays	Deep interacting events shifted to higher bin				
7	Energy Bin Shifting	More elastic events shifted to lower bin				
8	Decreasing Layer Detection Efficiency	Deep interacting events suppressed		✓	LAST LAYER CUT	Last layer included was layer 6 consistant with cascade fluctuation and persistance cut
9	Muon Contamination	Muon interactions independent of depth	✓		PERSISTENCE CUT	Apply maximum cut not exceeding 700 gm/cm^2 or 5% of data rejection
10	Formation Zone	Detection deferred to deeper depth. Deplete events from early layers. Most serious at low energy. Varies with log D	✓		FIRST LAYER CUT	Ignore interactions in layer 1 which suffers from primary formation zone effect
11	Relative Low Signal LADC Settings	Some LADC require a min signal for output.	✓		DETECTION LEVEL SELECTION	There is no region of D that is free from all four systematic effects simultaneously. Nor can each effect be corrected independently. Thus should seek region where all effects are small and where residue effects have first order cancellations among themselves. Guided by $\Delta\lambda$ min. Resulting uncertainty indicated by range of ΔN_2 max. Final D = 10 ± 2.3. Average system. error = 29% statistical error.
12	Landau Fluctuation	Landau tail causes premature detection		✓		
13	Degree of Inelasticity	More elastic events suppressed to deeper layers at high D	✓			
14	Residue Muons	More serious at low energy. Also photonuclear events	✓		CORRECTION AFTER MAXIMUM LIKELIHOOD FITS	Monte Carlo correction for μ surviving persistence cut. Apply modified Rossi calculation with ± 30% FWHM assumption. With π-p flux ratio = 0.3, σ_{π} Fe = 596 mb (Allaby: $A^{0.743}$ interpolation.) $(\frac{\sigma_a}{\sigma_t})_{cu} = 0.625$, $\sigma_T(A) = \sigma_0 A^{2/3}$ (Bellettini), σ_T(n-cu) = 1262mb (Jones), $\frac{\sigma_{pFe}}{\sigma_{Fe}} = 1.0424$
15	Pion Contamination	Effective cross section lowered	✓			

Table 4 Systematic Problems and Solutions

fluctuation in the fraction of unsampled nuclear fragments and the Landau fluctuation of individual energy losses, particularly in the beginning and the end of the cascade. It is unnecessary at this point to review in detail the calculation of energy determination from the raw LADC signals except to note that proper weighting has been given to each layer and corrections have been allowed for the unseen nuclear disintegration and scintillation response. The average behavior of cascades are shown in Fig.65 and compared with Monte Carlo calculations of W.V. Jones.(37) The uncertainty associated with any single event was estimated to be about 20% and sampled ionization at any given depth may vary wildly about the average values. This was the major source of error in determining the first interaction site and will be discussed forther later on.

Due to the width of energy resolution, the edge of the energy spectrum near the trigger threshold appears diffused and depressed. Those marginal events which did trigger the system were those which developed on the average, longer and flatter cascades, hence were less vulnerable to the truncation effect of discrete sampling. This means that, on the average, their first interaction sites would be detected deeper down, or λ_{Fe} would be too high for the lower energy bins. The solution to this problem was to make an energy cut, such that only events in the region with a constant slope of the energy spectrum would be

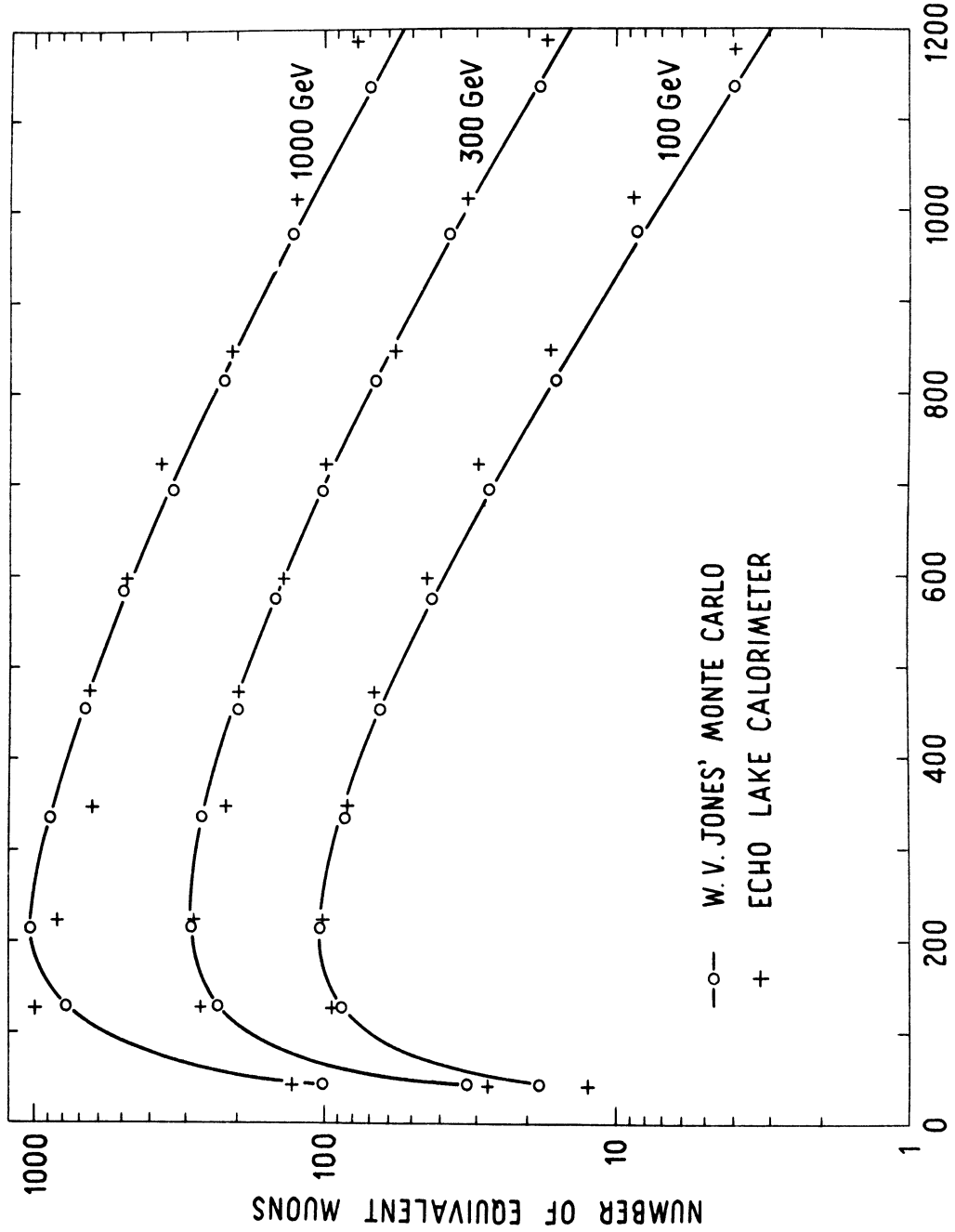

Fig. 65 Comparison of the Average Shower Curves with the Monte Carlo Results of W.V. Jones

accepted. This corresponds to a 70 GeV and 211 GeV cut for the nominally 36 GeV and 90 GeV triggers respectively.

(3) Side Leakage: Due to the finite size of the calorimeter some fraction of the cascades, particularly at large zenith angles, may escape. Not mentioning the energy underestimation, the more serious effect was to have a trigger bias against those which interacted at deeper layers, resulting in an underestimation of λ_{Fe}.

This effect was avoided by making a geometry cut. The trajectory of the incident particle as determined by the spark chamber was extrapolated beyond the interaction site and this ray was required to pass through the top counter $(182.8\ cm)^2$, layer 2 $(180.0\ cm)^2$ and an imaginary square at the level of layer 10. The size of this square was used as a parameter and as it was increased from some nominally small dimension, $\Delta\lambda_{Fe}$ was noted to decrease due to the increase in statistics. However beyond a certain area, $\Delta\lambda_{Fe}$ was reached and further acceptance of events actually led to a larger $\Delta\lambda_{Fe}$. This provided evidence for the onset of systematic errors. The optimum size used was $(260\ cm)^2$. For comparison, the actual size of layer 10 was $(244\ cm)^2$.

(4) Non-uniform Scintillator Response: The edge-center relative response of the scintillators was about 2.3 for the thick layers (layers 3 through 9) compared to about unity for the other thin layers. For the former cases, a

well fitted quadratic correction function was applied in the energy calculation. In any case the geometry cut would prevent any incident tracks from coming too close to the edge of the scintillators and be mistaken as an interaction.

(5) Bottom Leakage: Based on the average cascade development, a correction function was applied to those cascades which leak through the last layer.

(6) Delta Rays: There may be energetic delta ray production before the particle makes the first strong interaction. This effect will be discussed in the next section.

(7) Energy Bin Shifting: The measurement of energy dependency of cross-sections requires events to be sorted into the same unique energy bins reguardless how the measurements be made. Since the hadron flux of energy greater than E (GeV) is

$$N\ (>E) = 3\times10^{-3}\ E^{-2}\ \left(cm^{-2}\ sr^{-1}\ sec^{-1}\right)\ ,$$

the fractional change in the bin statistics is roughly proportional to E^{-1} for a constant shift of energy ΔE in the energy evaluation. This would introduce an energy bias if the events that move across the bin boundaries are not typical of their binmates. The procedure of energy evaluation therefore must be done with more care.

Normally energy was calculated for the hadronic cascade and no attempt was made to evaluate the small but

uncertain contribution from the ionization and energetic delta ray production before the first strong interaction. If the first interaction was detected in layer j, the LADC outputs of the layers previous to layer j were excluded in order to avoid the delta ray confusion. But since interactions have various degree of inelasticity, the apparent layer of first interaction (LFI) depended on the detection threshold D and so would the energy determination and binning.

It was observed that for reasonable increase in D, LFI was down shifted by no more than a layer. Thus a compromise was to include the LADC of the (j-i) layer in the energy calculation.

(8) Decreasing Layer Detection Efficiency: Energy leakage also contributed to decreasing triggering efficiency for deeper interactions. This difficulty was easily overcome by terminating the maximum likelihood calculation at layer 6. It would leave over 700 gm/cm^2 for cascade development and was entirely consistant with the persistance cut question discussed later. Examinations of the attenuation curves indicated that no energy dependent last layer cut was necessary.

(9) Muon Contamination: If a very energetic muon decays in the calorimeter, it will initiate an electromagnetic cascade. A muon may also initiate a hadronic cascade through photonuclear interaction. This will constitute a

small uniform background at any depth, but the fractional effect is more serious for deeper layers and λ_{Fe} will be too high.

Fortunately the photonuclear interaction is a small (about 3% in emulsions) [45] fraction of the total muon background. Thus it seems possible to exclude the muon events by "pulse shape discrimination".

Electromagnetic cascades are characteristically sharper than hadronic cascades of the same detected energy. This means that their persistence is shorter and consequently less sensitive to the change of D. The persistence of an event was taken as the vertical distance between the z coordinates of the first and last layer which had outputs greater than D equivalent muons plus the mean thicknesses of the end layers. The zenith angle effect was also corrected for.

Fig.66 shows the behavior of persistence (gm/cm^2) with D. The hadronic curves were obtained from the mean persistences of the two energy bins with high statistics. The dashed curves are EM cascades based on the calculation by Rossi [46] and the experimental EM curves were obtained from those energy bins where there was a clear separation of the two groups (Fig.67). The comparitatively lower values experimental curves were probably due to the discrete sampling nature of the calorimeter.

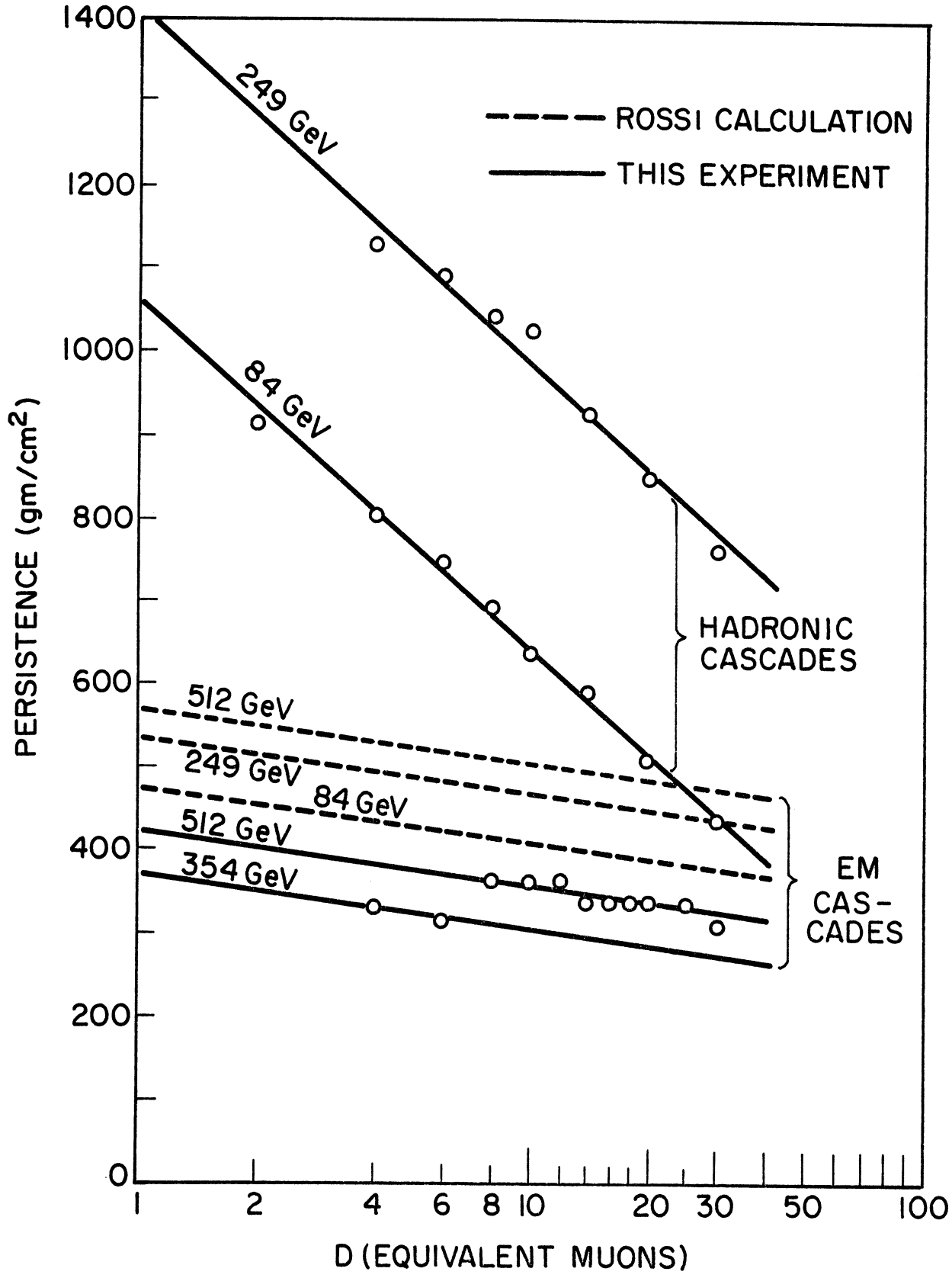

Fig. 66 Behavior of Hadronic and Electromagnetic Cascades in the Calorimeter

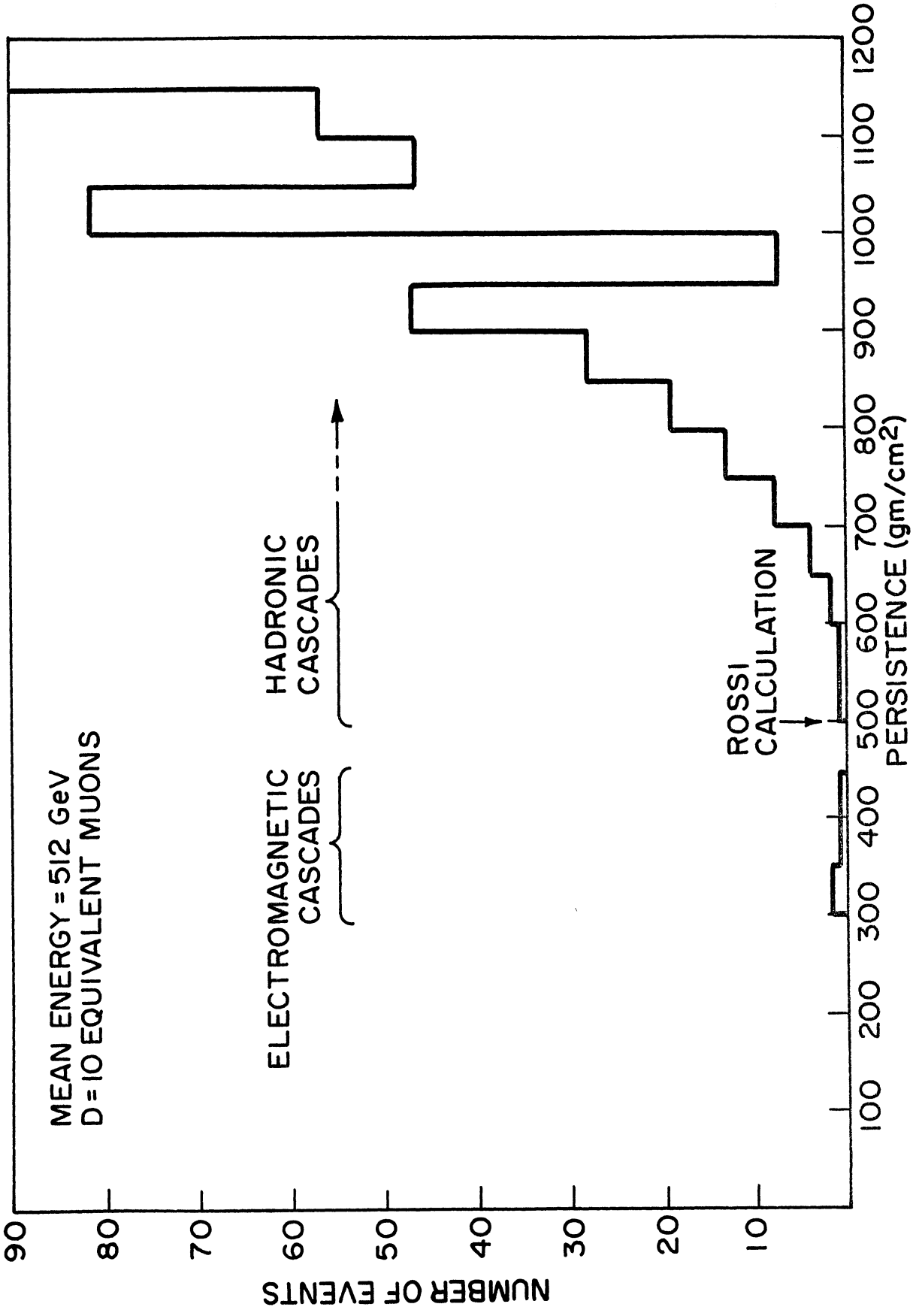

Fig.67 A Typical Persistence Distribution

The FWHM of the experimental hadronic cascades was about 30%. It is obvious in Fig.66 that in regions of high D's and low energies, the two types of cascades may no longer be distinguished. Following as closely as possible to the principle of exclusion rather than correction, it was decided to make a maximum cut not exceeding 700 gm/cm^2 (never necessary to be so high) or 5% of data rejection (such that statistics is not appreciably affected). The persistence cut matrix used is shown in Table 5 .

The muon contamination was estimated from a count of the short persistence events in those energy bins and at a level of D where there was clear separation of the hadron and EM groups. It was determined to be 1.7 ± 0.4% before the persistence cut.

(10) Formation Zone: Fig.68 is a schematic of an exaggerated initial portion of average shower curves. It is clear that on the average there is always a minimum distance z_F (called formation zone) in order that the cascade be developed to a particular detection level D. The size of z_F depends both on energy E and D.

The effect of the formation zone is that interactions occuring near the lower edge of a layer may not be detected until the subsequent layer. This down shifting of events ordinarily will not affect the slope of the attenuation curve except at the first layer where there is no com-

MEAN ENERGY (GeV)	D=4	D=6	D=8	D=10	D=12	D=14	D=16	D=18	D=20	D=25	D=30
84	385	360	330	310	300	290	280	270	260	240	220
120	420	385	360	335	320	310	300	290	280	265	245
173	480	440	410	380	360	345	335	330	320	300	285
249	580	540	510	480	460	435	420	410	400	375	310
354	690	655	630	600	580	560	545	530	520	490	470
512	700	700	700	700	700	680	650	665	655	625	605
742	700	700	700	700	700	700	700	700	700	700	700
1488	700	700	700	700	700	700	700	700	700	700	700

Table 5 Persistence Cut Matrix

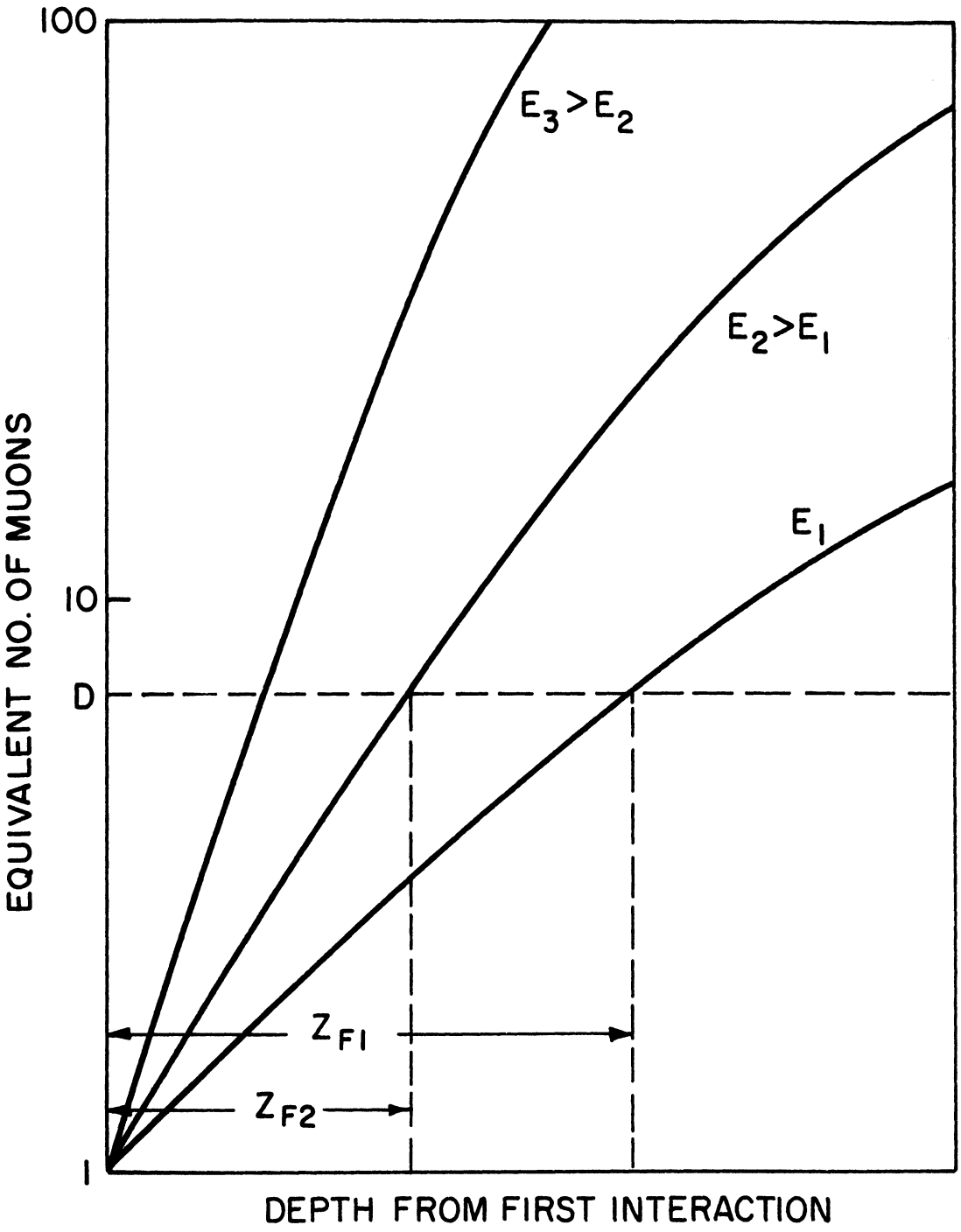

Fig.68 Illustration of Formation Zone by Qualitative Average Shower Curves

pensating events sliding down from above. Fig.69 illustrates the effect of the formation zone on the shape of the attenuation curve, hence λ_{Fe} also. It is also seen that z_F can be evaluated by making a fit to the lower portion of the attenuation curve. This has been done for all combinations of E and D. For example, at D = 10, z_F ranges from 18.4 gm/cm^2 at 84 GeV to 1.6 gm/cm^2 at 1500 GeV. The dependence of z_F on D was approximately logarithmic as expected.

An alternative of dealing with the z_F's is to incorporate them in the maximum likelihood calculation by replacing each z with an appropriate $(z-z_F)$. However, it was again preferred to keep a smaller but cleaner data sample by rejecting all events from layer 1.

It will be seen that the z_F's estimated above are only average values and individual events may fluctuate greatly. This means that the effect of z_F will be primarily in layer 1, but there will also be a small secondary effect in layer 2 and a neglegibly small tertiary effect in layer 3.

(11) Relative Low Signal LADC Setting: There was a pedestal in each LADC calibration in that a minimum signal of several equivalent muons was needed to give an output of one digit greater than no signal. The purpose of the pedestal was mainly to discriminate against noise and the set-

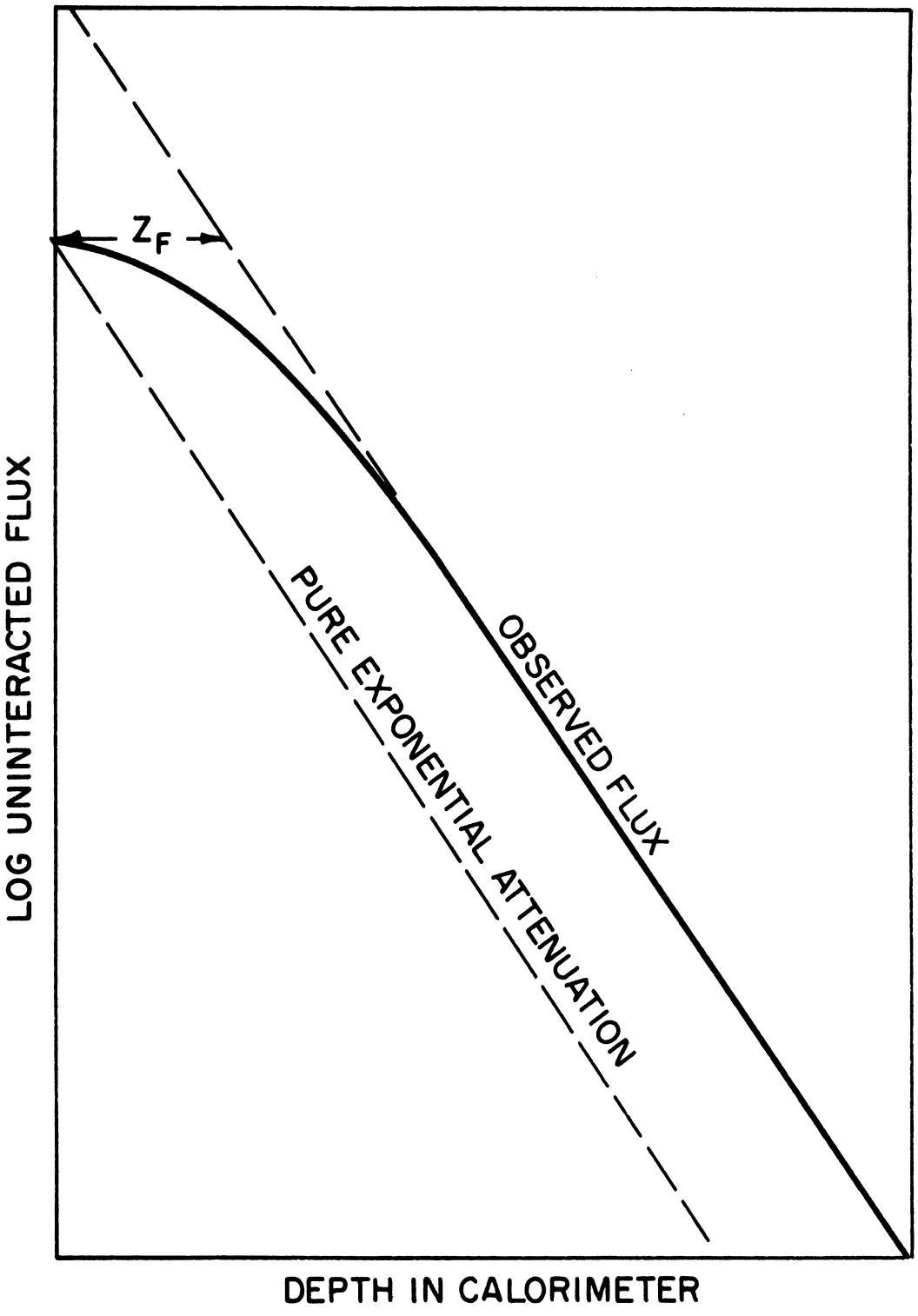

Fig.69 Effects of Formation Zone

tings were somewhat different for each layer, depending on the expected dynamic range. Thus for low values of D, λ_{Fe} depended strongly on the relative pedestal settings. The net effect was that λ_{Fe} would be too high if one used D to be less than seven or eight.

(12) Landau Fluctuation in Ionization: The ionization loss of a single particle typically has a Landau distribution in a sampling detector. The Landau tail can then be mistaken for an interaction and leads to too low a λ_{Fe}. It is expected that this effect is more serious at the lower values of D.

(13) Degree of Inelasticity: At increasing high values of D, the events of lower inelasticity are supressed to the deeper layers resulting in λ_{Fe} being too high.

Normally, this problem could be handled by making a series of measurements at different D's and then extrapolate λ_{Fe} to the value corresponding to D = 1. Such a technique was not possible here due to the dominance of other systematic effects at low D's.

Indeed, at any energy, the variation of λ_{Fe} with D reflected collectively all systematic effects of problems 10-13. There was no region of D that was free from all four systematic effects simultaneously. Nor could each effect be corrected independently. The optimum solution was to seek a region where all effects were small and where

residual effects had first order cancellations among themselves. When such an optimum D was determined, a quantitative uncertainty may then be evaluated for the combined contributing sources.

With all of the forementioned data cuts, λ_{Fe} and $\Delta\lambda_{Fe}$ were calculated by the maximum likelihood method for all combinations of E and D. The results are listed in tables 6 and 7 as λ_{Fe} and $\Delta\lambda_{Fe}$ matrices. The total number of interactions detected in layers 2 and 3 are called ΔN_2 and ΔN_3 respectively; and they are recorded in tables 8 and 9 as ΔN_2 and ΔN_3 matrices.

The general behavior of λ_{Fe} with D is illustrated in Fig.70. Regions of dominance by various effects are also indicated. Similarly the general behavior of ΔN_2 is illustrated in Fig.71, and the contributing factors that created this characteristic shape is illustrated if Fig.72. At low values of D, events were detected prematurely due to Landau fluctuations, hence the low values of ΔN_2. As D was increased, ΔN_2 recovers rapidly. In the mean time, the secondary effect of formation zone was building up as log D (more events were lost to layer 3 than gained from layer 1) so a peak was reached. Eventually, this logarithmic decrease would be superceded by the effect of inelasticity (gaining more events from layer 1 than losing to layer 2) at very high values of D. Of course these characteristic shapes were energy dependent and examinations of the pat-

MEAN ENERGY (GeV)	D=4	D=6	D=8	D=10	D=12	D=14	D=16	D=18	D=20	D=25	D=30
84	141.1	140.0	138.1	136.8	137.1	137.7	139.2	142.3	146.1	160.1	163.8
120	127.0	124.1	125.1	127.0	126.7	126.6	126.8	127.8	128.9	133.6	141.9
173	137.5	130.9	131.2	134.4	138.2	139.6	139.7	140.1	136.6	136.4	137.0
249	139.4	133.1	130.9	132.0	132.2	131.0	132.2	133.3	135.1	139.0	137.3
354	135.3	129.5	127.1	126.1	127.9	127.2	130.4	133.2	133.2	134.4	133.8
512	141.7	134.8	129.6	131.4	135.4	135.0	138.3	138.4	140.3	141.1	139.1
742	134.3	128.4	127.5	125.4	124.1	125.6	129.8	129.7	133.8	134.8	140.5
1488	172.1	142.4	136.5	138.8	148.2	148.6	148.9	149.1	144.5	144.7	141.0

Table 6 λ_{Fe} Matrix

MEAN ENERGY (GeV)	D=4	D=6	D=8	D=10	D=12	D=14	D=16	D=18	D=20	D=25	D=30
84	4.43	4.20	4.06	3.98	4.00	4.04	4.11	4.26	4.42	5.00	5.17
120	5.28	4.83	4.80	4.89	4.83	4.84	4.87	4.91	4.95	5.23	5.69
173	8.70	7.72	7.66	7.87	8.16	8.29	8.28	8.30	7.88	7.87	7.87
249	4.36	3.84	3.65	3.64	3.63	3.56	3.63	3.67	3.74	3.88	3.75
354	6.51	5.67	5.41	5.25	5.32	5.25	5.44	5.54	5.60	5.62	5.56
512	10.90	9.46	8.63	8.76	9.12	9.10	9.33	9.36	9.51	9.58	9.35
742	15.18	13.66	13.17	12.77	12.37	12.53	13.26	13.30	13.90	14.14	14.96
1488	33.34	22.84	20.80	20.99	23.14	22.92	23.05	22.93	22.19	22.24	20.81

Table 7 $\Delta\lambda_{Fe}$ Matrix

MEAN ENERGY (GeV)	D=4	D=6	D=8	D=10	D=12	D=14	D=16	D=18	D=20	D=25	D=30
84	736	798	831	849	837	833	820	810	803	778	748
120	426	490	505	500	511	505	505	500	501	494	481
173	170	202	207	205	201	199	201	202	216	215	217
249	717	875	954	973	979	996	986	986	971	953	999
354	304	374	401	422	422	429	423	425	424	427	434
512	123	151	173	172	172	170	172	171	171	170	171
742	52	59	64	65	68	69	67	67	65	64	62
1488	21	29	33	33	31	33	33	34	34	35	38

Table 8 ΔN_2 Matrix

MEAN ENERGY (GeV)	D=4	D=6	D=8	D=10	D=12	D=14	D=16	D=18	D=20	D=25	D=30
84	459	499	507	511	513	506	497	490	487	509	546
120	210	222	231	235	238	238	237	243	242	235	239
173	111	113	116	118	121	121	123	123	121	121	121
249	475	482	480	486	488	499	500	495	503	512	522
354	189	206	203	205	212	214	217	213	211	217	215
512	76	78	76	77	75	77	77	78	78	78	81
742	40	43	43	44	45	44	43	42	42	41	43
1488	13	16	16	17	18	16	16	15	15	13	14

Table 9 ΔN_3 Matrix

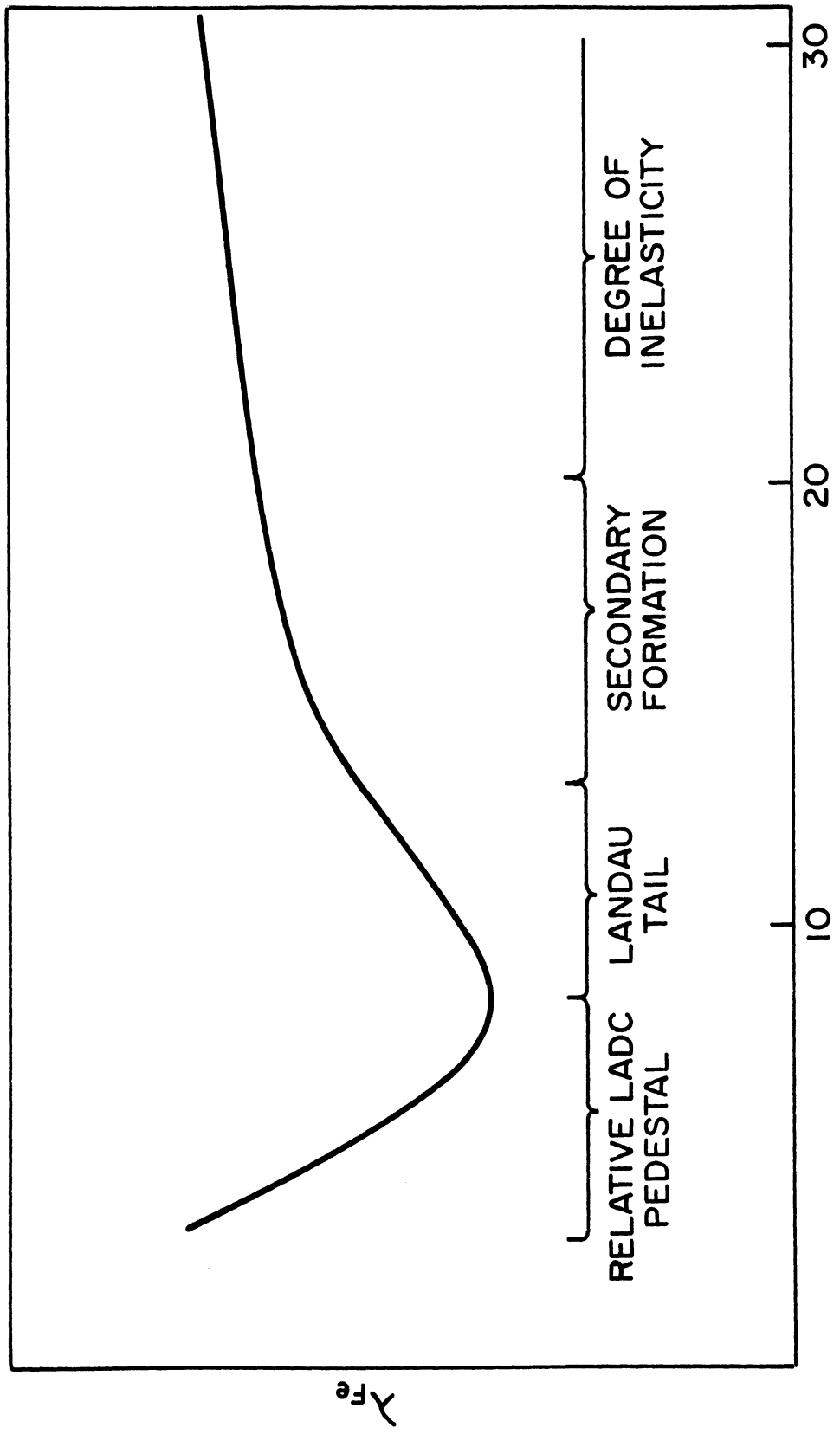

Fig.70 Characteristic Dependence of λ_{Fe} on D

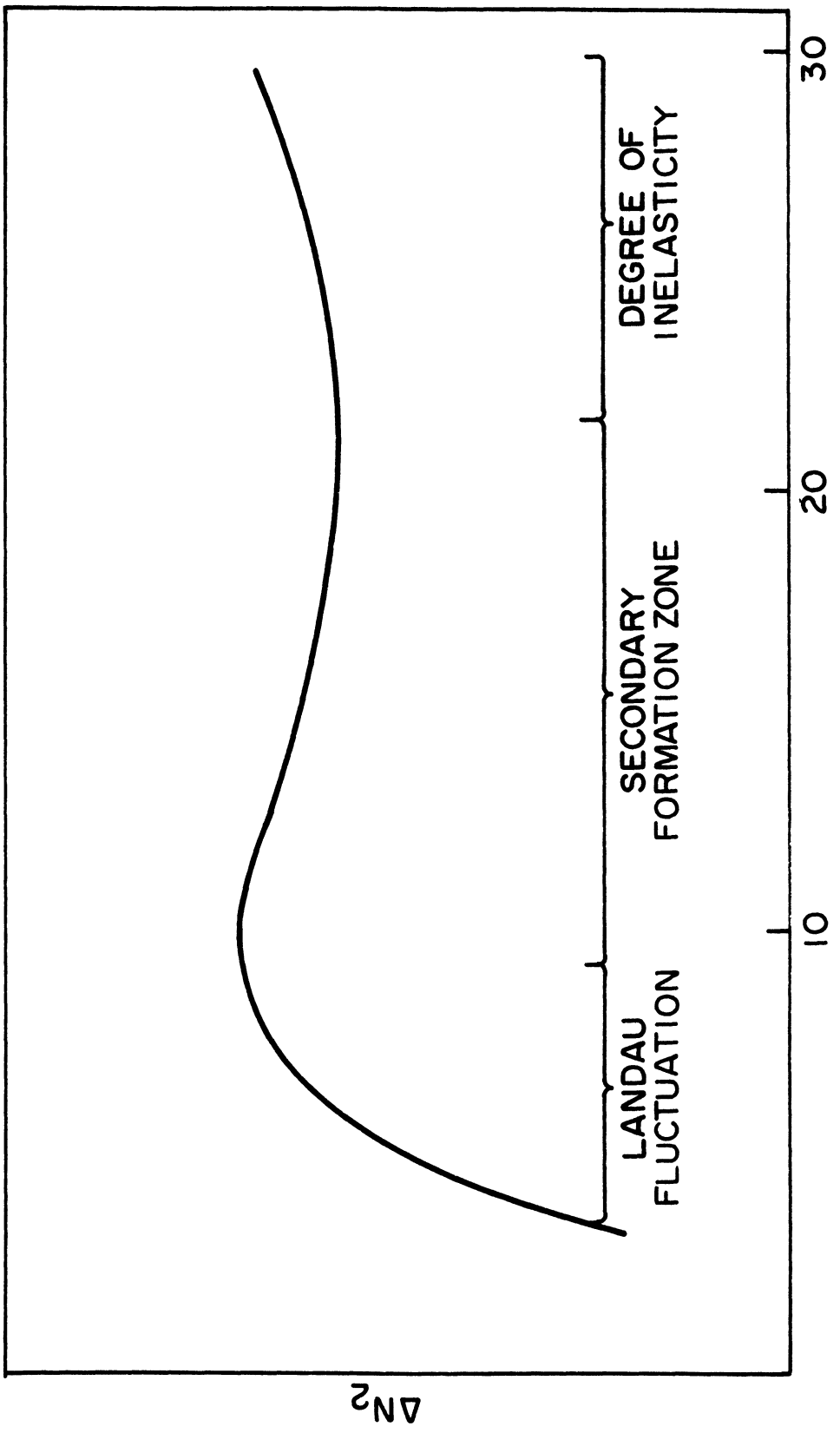

Fig.71 Number of Detected Interactions in Layer 2 vs. D

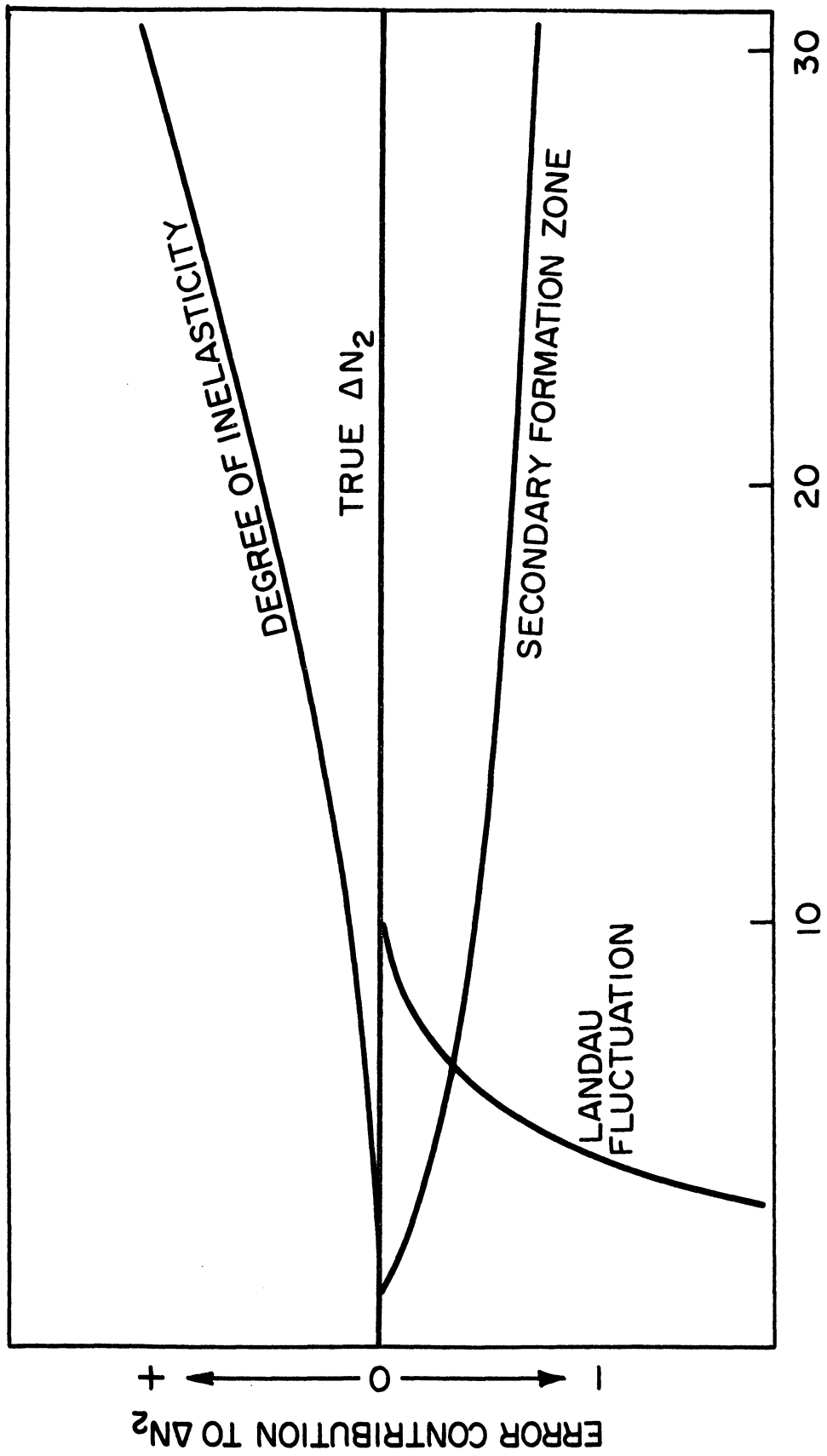

Fig.72 Error Contributions to ΔN_2

terns of variation of λ_{Fe}, ΔN_2 and ΔN_3 with E and D were entirely consistant with the above descriptions.

Table 10 is a "correlation matrix". It is to facilitate the choice of an optimum D and the evaluation of the resulting systematic uncertainty. For every energy bin, the letter

A is to mark the value of D at which λ_{Fe} is minimum,

B is to mark the value of D at which $\Delta\lambda_{Fe}$ is minimum,

C is to mark the value of D at which ΔN_2 is maximum,

X is to mark the value of D at which ΔN_3 is maximum.

All systematic effects tend to distort the attenuation curve from being a pure exponential, and $\Delta\lambda_{Fe}$ reflects this fact besides estimating pure statistical uncertainties. Therefore it is natural to choose the values of D at which $\Delta\lambda_{Fe}$ are minimum. As table 10 shows, there is no significant energy dependence of the location of B. Thus the mean value of D = 10 was chosen as the optimum for all energy bins.

Note that there was a remarkably strong correlation of B and C. Since the location of C depended on the combination of systematic effects, it was in a way a marker on the specific combination process. The strong correlation could then be interpreted as a consistant and effective cancellation of systematic errors. The remaining systematic uncertainty was represented by the spread of B or C. This r.m.s. spread in D was ± 2.3. The correspond-

MEAN ENERGY (GeV)	D=4	D=6	D=8	D=10	D=12	D=14	D=16	D=18	D=20	D=25	D=30
84				ABC	X						
120		A	B		C	X					
173		A	BC				X				
249			A			BC	X				
354				A		BC	X				
512			ABCX								
742					ABX	C					
1488			ABC		X						

Table 10 Correlation Matrix

ing uncertainty in λ_{Fe} was then seen to be, on the average, 29% of the statistical uncertainty, or less than 5% of the total error.

Note also that all the locations of A's were to the left (lower values of D) of B's. This assured that the cancellation process was not overwhelmed by a dominant source, namely the relative LADC pedestal settings. The facts that almost all the X's were on the right of C's and that dips in the ΔN_3 curves were almost non-existant were consistant with the expectation that formation zone effects occured only in the top layers.

F. CORRECTIONS

So far, the solutions to systematic problems were to seek optimum data cuts rather than to make numerous corrections. Cross sections were determined with the appropriate cuts incorporated into the maximum likelihood calculations. However there were two remaining effects that must be corrected.

(1) First was the residual muon contamination which survived the persistence cut. As it was noted, the overlapping of EM and hadronic cascades was more serious in the lower energy regions.

Table 11 summarizes the correction process. First it was assumed that the EM cascades were normally distri-

MEAN ENERGY (GeV)	PERSISTANCE CUT (gm/cm^2)	MEAN PERSISTANCE (gm/cm^2)	STANDARD DEVIATION (gm/cm^2)	RESIDUAL MUONS (%)	RESIDUAL MUON BACKGROUND (%)	CORRECTION FACTOR FOR λ_{Fe}
84	310	273	69	29.5	0.50	0.980
120	335	286	73	25.1	0.42	0.984
173	380	300	76	14.5	0.24	0.992
249	480	312	79	1.7	0.03	1.000
354	600	324	82	0.1	0	1.000
512	700	337	86	0	0	1.000
742	700	350	89	0	0	1.000
1488	700	367	93	0	0	1.000

Table 11 Muon Corrections

buted about a mean persistence which was taken to be 0.67 of the Rosse calculation. This assumption was of course not true, but it was approximately correct for practical purposes. The distribution was taken to have a spread of 30% FWHM, as was the case for hadrons, or a standard deviation of 25.4%. The percentage of muon which survived the persistent cut and the actual muon background in the hadron flux was then easily evaluated for each energy bin.

The effect of muon contamination was evaluated by an approximate Monte Carlo calculation. The primary hadron flux was attenuated exponentially in the calorimeter while muon interactions were distributed uniformly with depth. The surviving flux was then simulated at each layer of the calorimeter for appropriate values of λ_{Fe} and various percentages of muon contamination. Least square fits were then performed to obtain an apparent λ_{Fe} for each case and a direct comparison would give the correction factors needed.

(2) Among the incident charged hadrons there is a significant pion component. Pion cross sections are believed to be lower than proton's, thus the measured λ_{Fe} will be higher than the desired proton-iron interaction length λ_{pFe}.

The pion-proton flux ratio was determined to be approximately 0.3 [37]. The ratio of pion-proton inelastic cross section in iron was estimated from accelerator data at 20 GeV. In the cases where direct data on iron targets

were not available, interpolations were done from copper according to the dependence on mass number A. Proton data were also deduced from neutron data.

Specifically, A for iron is 55.85 and for copper, it is 63.54. The relation between interaction length λ and cross section σ is

$$\sigma = \frac{A}{N_0 \rho \lambda}$$

where N_0 is the Avogadro's number and ρ is the density. Thus for iron

$$\sigma = \frac{92679}{\lambda(\mathrm{gm/cm^2})} \ (\mathrm{mb}) \quad .$$

From Allaby's data,[47] the pion inelastic or absorption cross section is

$$\sigma_{\pi Fe} = 30.0 \times (55.85)^{0.743} = 595.9 \ \mathrm{mb} \quad .$$

From Jones' data,[48] the neutron copper total cross section is

$$\sigma_T \ (\mathrm{n\text{-}Cu}) = 1262 \ \mathrm{mb} \quad .$$

From Belletini's data,[49] the ratio of absorption to total cross section for copper is 0.625 and σ_T is proportional to $A^{2/3}$. The proton iron absorption cross section was then determined to be

$$\sigma_{pFe} = 1.0424 \ \sigma_{Fe} \quad ,$$

or $$\lambda_{pFe} = 0.9593\ \lambda_{Fe} \quad .$$

G. RESULTS

The results of corrections after the maximum likelihood calculation for D = 10 are listed in table 12.

Separate plots of λ_{pFe} and σ_{pFe} vs. energy are shown in Figs.73 and 74. The 20 GeV point was deduced form the accelerator data of reference (48).

The final results have been fitted to both a flat constant A and to a two parameter function of the form $A+B \log_{10} E$. Separate fittings were tried for both the inclusion and exclusion of the accelerator point. The complete results are listed in table 13.

Table 12 Final Experimental Results on Proton-Iron Inelastic Interations

Energy (GeV)		Number of Events	λ (gm/cm^2)	$\Delta\lambda$ (gm/cm^2)	σ (mb)	$\Delta\sigma$ (mb)
Bin Size	Mean					
70 - 101	84	1828	136.1	4.0	681	20
101 - 146	120	979	126.8	4.9	731	28
146 - 211	173	444	135.3	7.9	685	40
211 - 303	249	1965	134.0	3.7	692	19
303 - 437	354	831	128.0	5.3	724	30
437 - 629	512	335	133.3	8.9	695	46
629 - 905	742	138	127.3	13.0	728	74
>905	1488	68	140.9	21.3	658	100

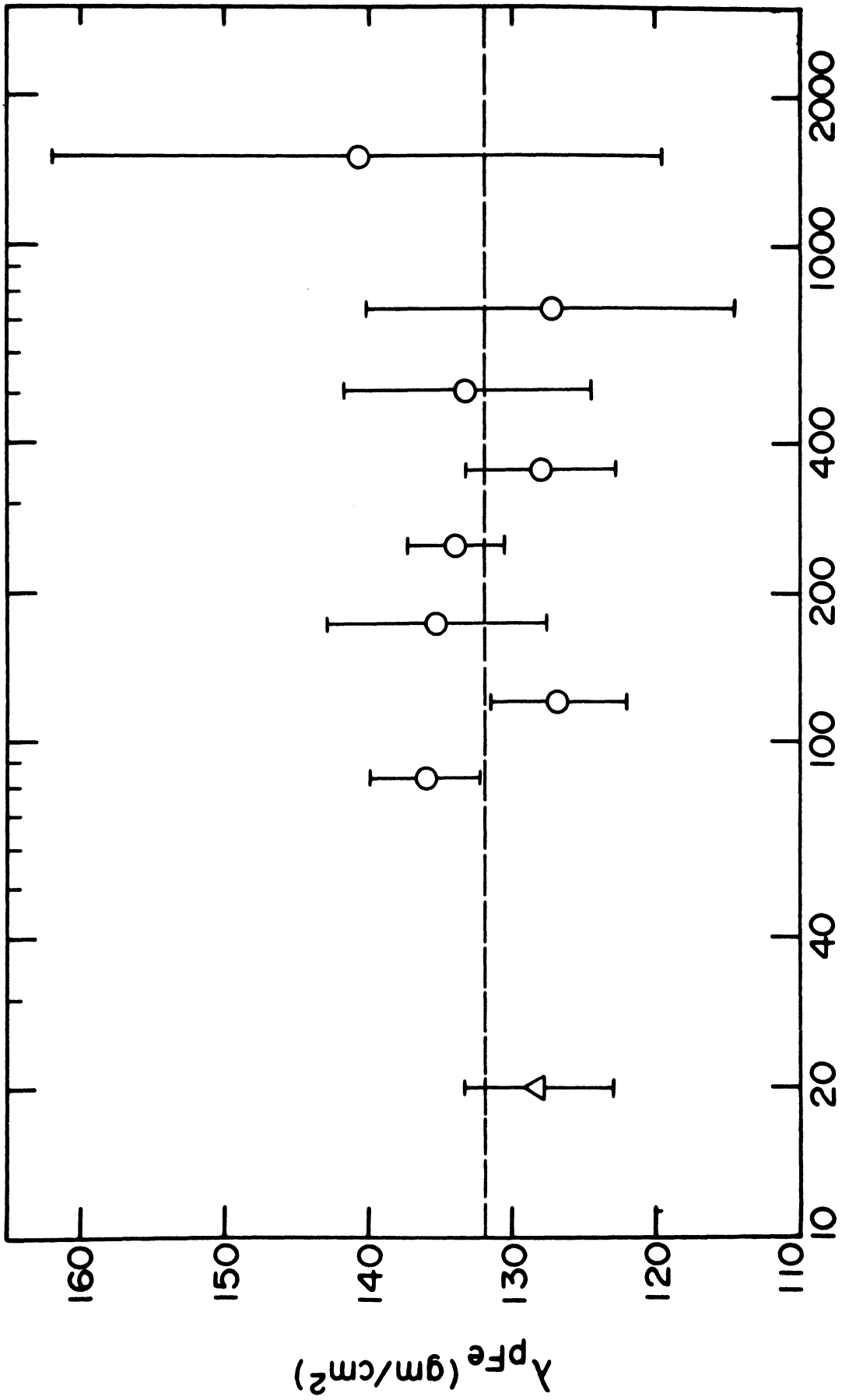

Fig.73 Variation of λ_{pFe} with Energy

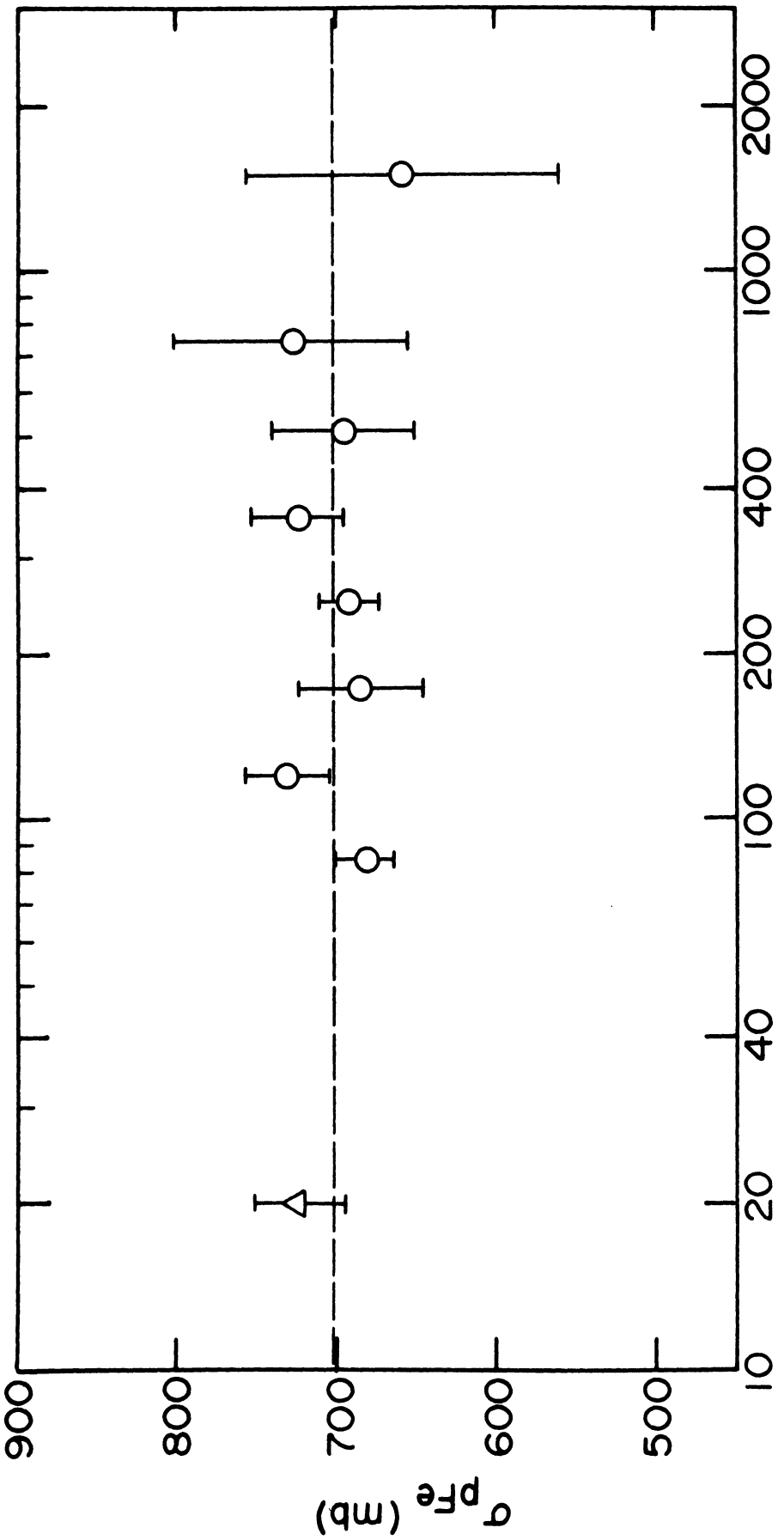

Fig.74 Variation of σ_{pFe} with Energy

Table 13

Results of Energy Dependent Curve Fittings

$$\lambda_{pFe} = A + B \log_{10} E$$

Data	A	B	χ^2/ Deg. Freedom
This Expt. Only	139.8 ± 16.4	-3.24 ± 7.16	0.55
This Expt. + Accel.	129.0 ± 9.9	1.35 ± 4.53	0.57

$$\sigma_{pFe} = A + B \log_{10} E$$

Data	A	B	χ^2/Deg. Freedom
This Expt. Only	660 ± 85	17.0 ± 37.3	0.53
This Expt. + Accel.	716 ± 54	-7.1 ± 24.7	0.56

$$\lambda_{pFe} = A$$

Data	A	χ^2/Deg. Freedom
This Expt. Only	132.4 ± 2.0	0.58
This Expt. + Accel.	131.9 ± 1.9	0.58

$$\sigma_{pFe} = A$$

Data	A	χ^2/Deg. Freedom
This Expt. Only	698 ± 10	0.57
This Expt. + Accel.	701 ± 10	0.57

H. CONCLUSION

From the fits to the experimental points we conclude that, between 20 and 1500 GeV, λ_{pFe} is best represented by 131.9 $\pm$1.9 gm/cm^2 independent of energy; although a slope of 3.5% change per decade change in energy is not ruled out.

Comparing to results of other similar cosmic ray experiments, we note that Andronikashvilli et al.[50] reported λ_{Fe}= 130 $\pm$ 6 gm/cm^2 between 50 and 800 GeV, and Bashindjhagyan et al.[51] reported λ_{pFe}= 132$\pm$ 5 gm/cm^2 at 400 GeV. None of the groups found any significant energy dependency.

Since we have better p-Fe data than p-p data, we may conclude that according to Trefil's calculation, σ_{pp} is also independent of energy. By the same token, the rising inelastic cross section in air can be attributed to a rising p-p total cross section.

CHAPTER VI

EPILOGUE

We have described the emergence of the SMW Trio from the world of high energy particle detectors. We have seen, through their basic operational mechanisms, their limitations, and some means of realizing their maximum characteristic potentials. We have also witnessed their incorportion into physics experiments, the touchstones for real effective performances.

Innovations are continuously being made on alleviating their shortcomings. To achieve isotropy in wide-gap chambers the application of a rotating electric field has been attempted.[52] To take advantage of the on line analysis capabilities of wire chambers, it is necessary to improve their spacial resolutions. This can be done by limiting lateral diffusion of the sparks and delta ray productions. A double barrel approach is to minimize gap width and going either to low temperature [53] or high pressure [54,55] operations. An even more radical attempt is to use liquid argon in the electron multiplication medium.[56] If cost is not of prime concern, multiwire proportional chambers can offer tremendous advantages in time resolution, repetition rate and multi-track effi-

ciencies.[17]

If a streamer chamber is driven by a short voltage pulse such that avalanches are not permitted to develop into streamers, metastable atoms may persist for preliminary analysis by auxiliary equipment to decide whether to re-pulse the chamber to record a possible rare event.[57] Another unique variation is the discharge-condensation chamber which is a hybrid of streamer and cloud chamber.[58] The dense column of ions developed from the initial short voltage pulse renders the chamber insensitive to other minimum ionizing tracks upon expansion, thus achieving good time resolutions ($\sim$1 μsec). The very long memory time ($\sim$ 0.01 sec) also allows auxiliary decision making instruments to trigger on rare events in a high flux background.

The addition of the magnetic spectrometer to the Echo Lake Experiment will permit an absolute calibration of a calorimeter at high energy for the first time, and a good correction to the systematic effects of the calorimeter to the transmission experiments will be possible. Also possible will be a much more definitive measurement of the π-p flux ratio which is an important correction factor in extracting the proton cross sections from the charged hadron cross sections.

List of References

(1) Robert Oppenheimer. Nature of Matter. Purposes of High Energy Physics. pp. 1-5. Edited by Luke C. L. Yuan. BNL 888 (T-360) 1965.

(2) Advanced Accelerator Concepts and Technology. A Report to the High Energy Physics Advisory Panel of the U. S. Atomic Energy Commission by the HEPAP Subpanel on Advanced Accelerator Technology. Sept. 1971.

(3) S. P. Denisov. Advances in Cerenkov Counters. Preprint (IHEP. 71-47) Serpukhov, 1971.

(4) P. M. Dauber, L. H. Smith and M. A. Wahlig. Nuclear Instruments and Methods 84 (1970) pp. 199-204.

(5) V. A. Davidenko, B. A. Dolgoshein, V. K. Semenov and S. V. Somov. Nuclear Instruments and Methods 67 (1969) pp. 325-330.

(6) P. V. Ramanamurthy. Nuclear Instruments and Methods 63 (1968) pp. 77-82.

(7) M. P. Lorikyan. Instruments and Experimental Techniques. pp. 273-274 (English Translation) 1968.

(8) Luke C. L. Yuan. Scintillation and Semiconductor Counter Symposium. Washington D. C. March 1970.

(9) A. I. Alikhanian, K. A. Ispirian, A. G. Oganessian and A. G. Tamanian. Nuclear Instruments and Methods 89 (1970) pp. 147-153.

(10) R. Hofstadter. Nuclear Instruments and Methods 63 (1968) pp. 136-140.

(11) Arthur Roberts. Review of Scientific Instruments 32 No. 5 (1961) pp. 482-485.

(12) J. G. Rutherglen. Progress in Nuclear Physics, Vol. 9 (1964) pp. 2-26.

(13) G. Charpak, L. Massonnet and J. Favier. Progress in Nuclear Techniques and Instrumentation, Vol. 1 (1965) pp. 321-324. North-Holland Publishing Co. Amsterdam.

(14) James W. Cronin. Bubble and Spark Chambers, Vol. 1, Chapter VI (1967) pp. 315-405. Academic Press Inc. N. Y.

(15) Otto C. Allkofer. Spark Chambers (1969) Verlag Karl Thiemig KG. Munich.

(16) W. A. Wenzel. Spark Chambers. UCRL-11319 (1964).

(17) G. Charpak. Evolution of the Automatic Spark Chambers. Annual Review of Nuclear Science 20 (1970) pp. 195-254.

(18) V. A. Davidenko, B. A. Dolgoshein, V. K. Semenov and S. V. Somov. Nuclear Instruments and Methods 67 (1969) pp. 325-330.

(19) A. von Engel. Ionized Gases (1955) p. 157 Oxford at the Clarendon Press.

(20) S. Fukui. CERN 63/37 (1963) p. 145.

(21) W. E. Hazen. Private communication.

(22) C. J. Evans. Nuclear Instruments and Methods 69 (1969) pp. 61-69.

(23) A. I. Alikhanyan. Loeb Lecture Notes given at Harvard University. Feb. 1965.

(24) V. M. Knyazev and V. A. Lyubimov. Instruments and Experimental Techniques (1969) English Translation. pp. 85-86.

(25) J. Fisher and G. Zorn. Review of Scientific Instruments 32 (1961) p. 503.

(26) G. E. Chikovani, V. N. Roinishvili, V. A. Mikhailov and A. K. Javrishvili. Nuclear Instruments and Methods 35 (1965) pp. 197-202.

(27) V. Davidenko, B. Dolgoshein and S. Somov. Nuclear instruments and Methods 75 (1969) pp. 277-286.

(28) M. L. Perl and L. W. Jones. Nucleonics, Vol. 18, No. 5 (1960) pp. 92-97.

(29) L. W. Jones and B. W. Loo. Advances in Electronics and Electron Physics, Vol. 22B (1966) pp. 813-822. Acadimic Press.

(30) E. Gygi and F. Schneider. CERN 66-14 Accelerator Research Division (1966).

(31) A. Odian. Proceedings of the 1966 International Conference on Instrumentation for High Energy Physics at SLAC. pp. 49-59.

(32) S. L. J. Prünster. Argonne National Lab Preprint, SLJP-1 (1970).

(33) E. Gygi and F. Schneider. CERN 64-46 Accelerator Research Division (1964).

(34) E. Gygi and F. Schneider. CERN-ISR/GS/71-17 (1971).

(35) I. I. Gromova, V. I. Nikanorov, G. Peter, and A. F. Pisarev, Instruments and Experimental Techniques, (1965) English Translation, pp. 63-67.

(36) L. P. Keller, R. A. Schluter and T. O. White, Argonne National Lab Preprint, (1965).

(37) G. D. DeMeester, Thesis (1971), University of Michigan High Energy Physics Technical Report, UM HE 71-5.

(38) G. B. Yodh, Yash Pal, and J. S. Trefil, Physical Review Letters, Vol.28, No.15, (April 1972) pp.1005-1008.

(39) T. P. McCorriston, Doctoral Thesis, University of Michigan (1972).

(40) R. J. Glauber, Lectures in Theoretical Physics, edited by W. E. Britten et al, (Interscience, N.Y.,1959), Vol.I, pp.315-414.

(41) R. J. Glauber, High Energy Physics and Nuclear Structure, edited by G. Alexander, (North-Holland, Amsterdam, 1967), pp.311-347.

(42) E. Abers et al., Nuovo Cimento 42A, (1965) p.365.

(43) J. S. Trefil, Predictions for Elastic and Inelastic Nucleon-Nucleus Cross Sections at High Energies, University of Virginia, Preprint (1971).

(44) L. W. Jones et al., The Properties of Proton-Proton Interactions Between 100 and 1000 GeV from a Cosmic Ray Experiment (Jan.1972), Submitted to Nuclear Physics.

(45) A. W. Wolfendale, Cosmic Rays (1963), p.96, George Newnes Ltd., London.

(46) Bruno Rossi, High Energy Particles, Prentice Hall, (1952) p.258.

(47) J. C. Allaby et al., Soviet Journal of Nuclear Physics Vol.13, No.3, (March 1971) pp.295-304.

(48) L. W. Jones et al., Physics Letters, Vol.36B, No.5, (Oct.1971) pp.509-512.

(49) G. Bellettini et al., Nuclear Physics 79 (1966) pp.609-624.

(50) E. L. Andronikashvili, G. E. Chikovani, D. I. Garibashvili, L. L. Gabunia, D. B. Kakawridze, D. M. Kotlyarevski, Z Sh. Manyavidze, N. N. Roinishvili, L. A. Razdolskaya, and E. N. Sherer, Canadian Journal of Physics, Vol.46, No. 10 (May 1968) pp.s689-s693.

(51) G. L. Bashindjhagyan, V. M. Belokopytov, A. I. Demianov, V. S. Murzin, L. I. Sarycheva, and N. B. Sinyov, Paper HE-24, 12th International Conference on Cosmic Rays, Hobart, University of Tasmania, Conference Papers, 6, 2211 (1971).

(52) M. I. Kozlov and N. S. Rudenko. Instruments and Experimental Techniques, (1969). English Translation, pp. 29-31.

(53) M. Atac. Nuclear Instruments and Methods, 93 (1971), pp. 521-523.

(54) W. J. Willis, R. Majka and W. Bergmann. Nuclear Instruments and Methods,91 (1971) pp.29-31.

(55) W. J. Willis, V. Hungerbuchler, W. Tanenbaum and I. J. Winters. Nuclear Instruments and Methods. 91 (1971), pp.33-36.

(56) S. E. Derenzo, R. A. Muller, R. G. Smits and L. W. Alvarez, Preprint, UCRL-19254 (Oct.1969).

(57) V. Eckardt, Preprint, DESY 70/60 (Nov.1970).

(58) Z. Sh. Mandzhavidze, V. N. Roinishvili, and A. K. Dzhavrishvili, Instruments and Experimental Techniques, English Translation,(1970) pp.48-52.